A direct numerical simulation study of a turbulent non-premixed lifted flame

Shahram Karami

School of Photovoltaic and Renewable Engineering

The University of New South Wales

This dissertation is submitted for the degree of

Doctor of Philosophy

March 2015

PLEASE TYPE

THE UNIVERSITY OF NEW SOUTH WALES
Thesis/Dissertation Sheet

Surname or Family name: **Karami**

First name: **Shahram** Other name/s:

Abbreviation for degree as given in the University calendar: **PhD**

School: **Photovoltaic and Renewable Energy Engineering** Faculty: **Engineering**

Title: **A direct numerical simulation study of a turbulent non-premixed liftedflame**

Abstract 350 words maximum: (PLEASE TYPE)

A turbulent lifted slot-jet flame is studied using direct numerical simulation (DNS). A one- step chemistry model is employed with a mixture-fraction dependent activation energy which can reproduce qualitatively the dependence of laminar burning rate on equivalence ratio that is typical of hydrocarbon fuels.

The qualitative structure of the flame is first examined, confirming some features that have previously been observed in experimental measurements as well as some which have not been previously discussed. Significant differences are observed comparing the present DNS representing a hydrocarbon fuel, and previous DNS representing hydrogen fuel.
The statistics of flow and relative edge-flame propagation velocity components conditioned on the leading edge-flame locations are then examined. The results show that on average, the streamwise flame propagation and streamwise flow balance, thus demonstrating that edge-flame propagation is the basic stabilisation mechanism. Fluctuations of the edge locations and velocities are, however, significant. It is demonstrated that the edges tend to move in an essentially two-dimensional elliptical pattern (laterally outwards towards the oxidiser, then upstream, then inwards towards the fuel, then downstream again). It is proposed that this is due to the passage of large eddies, as outlined in Su et al. [1]. However, the mechanism is not entirely two-dimensional, and out-of-plane motion is needed to explain how flames escape the high velocity inner region of the jet.

Next, the time-averaged structure is examined. The entrainment flow is shown to be diverted around the flame base causing locally upstream streamwise velocities. A budget of terms in the transport equation for product mass fraction is used to understand the stabilisation from a time-averaged perspective. It is found to be consistent with the instantaneous perspective, featuring a fundamentally two-dimensional structure involving upstream trans- port of products on the lean side balanced by entrainment into richer conditions, while on the rich side, upstream turbulent transport and entrainment from leaner conditions balance the streamwise convection.

A complete analysis of the reasons behind the observed trends in the flame relative propagation velocity has been performed. The mean normalised edge-flame speed is less than laminar flame speed (at around 0.6 of laminar flame speed) and the edge-flame velocity fluctuations are mainly connected with strain rates, scalar dissipation rate, mixture-fraction curvature, product mass fraction curvature and the inner product . These quantities as well as the average normal orientations and nature of the flame in terms of categorisation of the edge as premixed or non-premixed go through cyclic fluctuations which appear to be connected with the passage of large eddies and the elliptical pattern of the on-average motion.

Overall the results provide strong support for the edge-flame theory of flame stabilisation, but point to significant roles played by large, coherent eddies in determining fluctuations of both the flow velocities and edge-flame relative propagation velocities, and thus the lifted height.

FOR OFFICE USE ONLY Date of completion of requirements for Award:

THIS SHEET IS TO BE GLUED TO THE INSIDE FRONT COVER OF THE THESIS

I would like to dedicate this thesis to my loving parents and my little lovely sister.

Declaration

Originality statement

' I hereby declare that this submission is my own work and to the best of my knowledge it contains no materials previously published or written by another person, or substantial proportions of material which have been accepted for the award of any other degree or diploma at UNSW or any other educational institution, except where due acknowledgement is made in the thesis. Any contribution made to the research by others, with whom I have worked at UNSW or elsewhere, is explicitly acknowledged in the thesis. I also declare that the intellectual content of this thesis is the product of my own work, except to the extent that assistance from others in the project's design and conception or in style, presentation and linguistic expression is acknowledged.'

Shahram Karami

March 2015

Acknowledgements

It is with immense gratitude that I acknowledge the support and help of my supervisors, Associate Professor Evatt R. Hawkes and Dr. Mohsen Talei over the last three and half years. They continually and convincingly conveyed a spirit of adventure in regard to research. Without their guidance and persistence helps this thesis would have remain a dream. It gives me great pleasure in acknowledging Dr. Jacqueline H. Chen for her valuable comments and suggestions. I also consider it an honor to work with Dr. Shawn Kook and I would like to thank him for his support.

I would like to thank Dr. Hongfeng Yu for his time and effort on generating valuable and amazing animations.

I am indebted to my many colleagues who supported me over the last three and half years, namely Dr. Obulesu Chatakonda, Dr. Yuanjiang Pei, Dr. Shyam Sundar Pasunurthi, Fatemeh Salehi, Jalal (James) Behzadi, Alexander Krisman, Ali Haghiri, Shakil Ahmmed, Joshua Tang, Shervin Karimkashi, Nabeel Qazi and etc.

I also would like to acknowledge the computational facilities supporting this project including the Australian NCI National Facility, the partner share of the NCI facility provided by Intersect Australia Pty Ltd., the Peak Computing Facility of the Victorian Life Sciences Computation Initiative (VLSCI), iVEC (Western Australia), and the UNSW Faculty of Engineering.

I would like thank Dr. Joachim Mai for his support on Intersect computational facilities and James Rudd for his support on our group computing cluster.

Abstract

A turbulent lifted slot-jet flame is studied using direct numerical simulation (DNS). A one-step chemistry model is employed with a mixture-fraction dependent activation energy which can reproduce qualitatively the dependence of laminar burning rate on equivalence ratio that is typical of hydrocarbon fuels.

The qualitative structure of the flame is first examined, confirming some features that have previously been observed in experimental measurements as well as some which have not been previously discussed. Significant differences are observed comparing the present DNS representing a hydrocarbon fuel, and previous DNS representing hydrogen fuel.

The statistics of flow and relative edge-flame propagation velocity components conditioned on the leading edge-flame locations are then examined. The results show that on average, the streamwise flame propagation and streamwise flow balance, thus demonstrating that edge-flame propagation is the basic stabilisation mechanism. Fluctuations of the edge locations and velocities are, however, significant. It is demonstrated that the edges tend to move in an essentially two-dimensional elliptical pattern (laterally outwards towards the oxidiser, then upstream, then inwards towards the fuel, then downstream again). It is proposed that this is due to the passage of large eddies, as outlined in Su *et al.* [1]. However, the mechanism is not entirely two-dimensional, and out-of-plane motion is needed to explain how flames escape the high velocity inner region of the jet.

Next, the time-averaged structure is examined. The entrainment flow is shown to be diverted around the flame base causing locally upstream streamwise velocities. A budget of terms in the transport equation for product mass fraction is used to understand the stabilisation from a time-averaged perspective. It is found to be consistent with the instantaneous perspective, featuring a fundamentally two-dimensional structure involving upstream transport of products on the lean side balanced by entrainment into richer conditions, while on the rich side, upstream turbulent transport and entrainment from leaner conditions balance the streamwise convection.

A complete analysis of the reasons behind the observed trends in the flame relative propagation velocity has been performed. The mean normalised edge-flame speed S_e^* is less

than laminar flame speed, S_L, (at around 0.6 S_L) and the edge-flame velocity fluctuations are mainly connected with strain rate, scalar dissipation rate, mixture-fraction curvature, product mass fraction curvature and the inner product of the normal vectors to product mass-fraction and mixture-fraction iso-surfaces. These quantities as well as the average normal orientations and nature of the flame in terms of categorisation of the edge as premixed or non-premixed go through cyclic fluctuations which appear to be connected with the passage of large eddies and the elliptical pattern of the on-average motion.

Overall the results provide strong support for the edge-flame theory of flame stabilisation, but point to significant roles played by large, coherent eddies in determining fluctuations of both the flow velocities and edge-flame relative propagation velocities, and thus the lifted height.

Preface

The thesis concerns direct numerical simulation modelling of a turbulent lifted flame aiming to understand the stabilisation process and the edge-flame propagation statistics. It is based on the following papers:

Journal papers:

1. Shahram Karami, Evatt R. Hawkes, Mohsen Talei and Jacqueline H. Chen, "Edge flame statistics in a turbulent non-premixed lifted flame", is to be submitted to *Physics of Fluids.*

2. Shahram Karami, Evatt R. Hawkes, Mohsen Talei and Jacqueline H. Chen, "Stabilisation mechanisms in a turbulent lifted slot-jet flame at a low lifted height", submitted to *Journal of Fluid Mechanics.*

Peer-reviewed conference papers:

1. Shahram Karami, Evatt R. Hawkes and Mohsen Talei, "A direct numerical simulation study of a turbulent lifted flame in hot oxidizer", *18th Australasian Fluid Mechanics Conference*, Launceston, Australia, 3-7 December 2012, pp 149, ISBN 9780646583730.

2. Shahram Karami, Mohsen Talei and Evatt R. Hawkes, "Direct numerical simulation of a partially premixed turbulent, lifted flame", presented at *9th Asia-Pacific Conference on Combustion*, 19-22 May 2013, Korea, Page 237.

3. Shahram Karami, Mohsen Talei and Evatt R. Hawkes, "Flame base analysis in a turbulent, partially premixed lifted flame", presented at the *Mediterranean Combustion Symposium*, 8-13 September 2013, Turkey, Paper Number: TC-22.

4. Shahram Karami, Mohsen Talei and Evatt R. Hawkes, “A numerical study of species transport budgets in a turbulent lifted flame”, presented at *Proceedings of the Australian Combustion Symposium*, November 2013, The University of Western Australia, pp. 162-165, ISSN 1839-8162.

5. Shahram Karami, Evatt R. Hawkes and Mohsen Talei, “Direct numerical simulation of a turbulent lifted flame: stabilisation mechanism”, submitted to *19th Australasian Fluid Mechanics Conference*, Melbourne, Australia, 8-11 December 2014.

Contents

List of Figures

List of Tables

Nomenclature

Roman Symbols

α	Heat release parameter
γ	Ratio of specific heat
a	Sound velocity
c_v	Heat capacity at constant volume
D	Diffusivity of species
d_f	Damping function
E	Sensible energy
H	Jet width
L_x	Length of the domain in the streamwise direction
L_y	Length of the domain in the transverse direction
L_z	Length of the domain in the spanwise direction
N_x	Number of grid points in the streamwise direction
N_y	Number of grid points in the transverse direction
N_z	Number of grid points in the spanwise direction
p	Pressure
Q	Heat release per unit mass of fuel
q	Heat flux

R	Universal gas constant
r	Stoichiometric oxidiser to fuel mass ratio
S_L	Laminar flame speed
T	Temperature
t	Time
T_{ad}	Adiabatic temperature
U	Velocity vector
x	Cartesian coordinates
Y	Mixture fraction
Y_{Fst}	Stoichiometric mixture fraction
Da	Non-dimensionalisation Damköhler number
Le	Lewis number
Pr	Prandtl number
Re	Reynolds number
Sc	Schmidt number

Greek Symbols

ε	Turbulent dissipation rate
η_k	Kolmogorov length scale
α	Heat-release parameter
β	Zeldovich factor
δ	inlet momentum (and mixing layer) thickness
γ	Heat capacity ratio or adiabatic index or ratio of specific heats
ν	Kinematic viscosity

τ Heat-release parameter

ω Reaction rate

σ Damping constant

ζ Damping constant

δ_{ij} Kronecker delta

μ Molecular viscosity

ρ Density

τ_{ij} Viscous tensor

δ_{th} Thermal thickness

Superscripts

$*$ Dimensional values

Subscripts

c Co-flow

F Fuel

in Inlet

j Jet

O Oxidiser

o Fuel stream condition at the inlet

Chapter 1

Introduction

A considerable fraction, approximately 90%, of the world's total primary energy supply is generated via combustion of fossil and biomass fuels [2]. Historically this has been because combustion systems have been a very cost-effective method of energy generation due to the low cost of fossil fuels, and their high energy density. Recent decades have seen a shift away from combustion, particularly in the electricity and residential heat sectors, due principally to concerns about climate change and the decreasing costs of renewable generation. However, it is expected that combustion systems will remain dominant overall for decades to come. In addition, there are particular, hard to address energy markets that renewables are unlikely to penetrate at a high fraction in foreseeable futures. These include, in order of decreasing difficulty: aviation, high temperature industrial process heat, and automotive transportation. Combustion systems are often categorised by the mixedness of the fuel and oxidiser when delivered into the combustion chamber. In premixed systems, the fuel and oxidiser are mixed at some point before entering the combustion chamber. In fully non-premixed systems, the fuel and oxidiser enter in separate streams and mix simultaneously when they are burning. Partially non-premixed systems are also possible. In these systems, fuel and air may be injected separately but undergo a certain extent of mixing prior to combustion occurring. Non-premixed and partially premixed systems are easier to design for robust operation and are less complicated to build, but suffer from high levels of pollutants including oxides of nitrogen NO_X and soot. Many combustion devices, such as furnaces, steam boilers, diesel engines, liquid rocket motors and gas turbine engines feature non-premixed or partially premixed operating modes. Premixed systems are more difficult to design but it is possible to operate them with lower pollutant levels. For example, lean premixed combustion is often used to reduce NO_X and soot emissions, relative to a non-premixed operating mode. The design of premixed combustion systems is however

complicated by issues such as flashback, flame blow-out, themoacoustic instabilities, and unwanted pre-ignition.

When injecting fuel into a non-premixed or partially premixed combustion system, it is beneficial for several reasons to inject it at high velocity. First, it minimises the size of the fuel injection equipment. Second, and more importantly, it increases mixing rates which decreases the required overall size of the combustion chamber, since non-premixed and partially premixed systems typically operate in regimes which are mixing rate-limited, as opposed to being combustion rate-limited. A consequence of injecting the fuel at high velocity is that the flame may become lifted. Considering a simple fuel jet injection into a quiescent oxidiser environment, for low fuel-injection velocities, an attached flame which burns in a fully non-premixed mode is usually observable. However, if the fuel injection velocity is increased beyond a critical level, the flame abruptly detaches from the fuel nozzle and stabilises at some point further downstream. In this situation, the flame is termed as “lifted". Depending on the lifted height, the fuel and air will undergo a certain level of premixing prior to the lifted location, and thus the situation of a lifted flame is a partially premixed combustion scenario.

Besides the high fuel injection velocity that causes the flame to lift, there are several other advantages of having a lifted flame as opposed to an attached flame. One key advantage is that via the larger degree of premixing prior to combustion, combustion occurs in on-average somewhat leaner conditions, which greatly reduces soot emissions and also reduces prompt NO_X. Another key advantage is reduction of heat transfer back to the burner. In the case of attached flames, the large amount of heat transfer to the burner necessitates the use of expensive, temperature-resistant materials such as ceramics. However, commonly available metals can be used for construction of burners in the case of lifted flames which means simpler manufacturing process and therefore lower cost. One of the most crucial parameters for lifted flame operation is the lifted height. Higher velocities result in a longer lifted height, which is beneficial to increase mixing rates and thus reduce the size of the combustion equipment and also emissions; however, if the lifted height is too large, flame instability or even blow-off can become problematic. The lifted height is also significant in the sense that any computational model of a lifted flame would obviously need to predict it correctly in order to have an overall good prediction of other quantities. As such the mechanism by which lifted flames are stabilised has been studied extensively. The stabilisation mechanism has been clearly understood in laminar lifted flames [3–6]; however, for the turbulent lifted flames several theories have been proposed, which are summarisied in chapter 2, but the available evidence to date does not provide enough information to fully support

any one theory [7–9].

Almost all of the prior evidence has been accumulated from experimental studies. Early studies used simple measurements of flame luminosity to mark the lifted height location [10–16], but capabilities have significantly advanced over the years. The most advanced recent measurements are capable of simultaneously measuring laser-induced fluorescence of one or more species and all velocity components in a two-dimensional plane and in a time-resolved manner [9, 17–19]. However, despite these significant advances, the full three-dimensional, time-evolving structure of a lifted flame has not been previously measured. Moreover, experimental measurements always contain some uncertainty, and this uncertainty can be significant for some quantities. Numerical modelling could be a solution where all quantities are in-principle available in three- dimensions and time. From all available modelling approaches, direct numerical simulation (DNS) is considered the most accurate as both the flow and flame are fully resolved. The main issue with DNS is however the computational cost limiting this method to simple configurations and parameter spaces (notably, to low Reynolds numbers). As a result, DNS is mainly used to reveal the fundamental physics of the turbulence and chemistry interactions in simplified configurations. The results of DNS can also be used to develop turbulent combustion models required for simulating industry applications.

Despite the potential of the DNS approach to help in understanding lifted flame stabilisation, there has only been one prior DNS of a lifted flame in an ambient oxidizer temperature environment, which is reported in [20, 21]. However, these early DNS considered hydrogen as a fuel. While an understanding of hydrogen lifted flames is certainly needed, the typical situation is of combustion of a hydrocarbon fuel. Hydrocarbon fuels have a significantly different combustion behaviour as compared to hydrogen, principally in that hydrogen burns at much richer and much leaner conditions than do hydrocarbons.

1.1 Research aims

The focus of this dissertation is therefore to develop an improved understanding of the mechanisms of stabilisation of a hydrocarbon lifted flame. The aims are achieved using DNS which employs a thermochemistry model which is capable of representing the main features of hydrocarbon combustion. Therefore, the objectives of this study are summarised as follows,

Performing a three-dimensional simulation of a lifted turbulent flame:

The first objective is to perform a three-dimensional DNS of a turbulent, lifted, slot-jet flame in an atmospheric co-flowing condition using single-step chemistry.

The reason for selecting a slot jet configuration was that the spanwise extent can be significantly smaller, and a shorter integration time is needed to obtain converged statistics, particularly near the centreline therefore the computational cost is lower.

The choice of a one-step chemistry model against an alternative more complex chemistry is on the basis of computational cost and the desire to achieve an otherwise realistic parameter space. The one-step chemistry model features a mixture-fraction dependent activation energy which can reproduce the dependence of laminar burning rate on equivalence ratio that is typical of hydrocarbon flames.

Analysing the instantaneous flame structure:

The second objective is to report the instantaneous structure of the lifted flame, describing important features of the overall structure and the leading edge flames, and comparing the observations against previous experimental work, previous DNS and theoretical concepts to explain lifted flame stabilisation.

Revealing the flame stabilisation mechanism:

The third objective is to analyse the flame base to reveal the lifted flame stabilisation mechanism. To do so, two distinctive approaches are used. First, the conditionally averaged flow and edge-flame velocities of the instantaneous flame base in the streamwise and spanwise directions are analysed to reveal the role of the edge-flame and flow interaction in the stabilisation process. Second, analysing the terms involved in the averaged transport equations of reacting scalars informs us on the averaged flame structure and reveals the roles of different physical mechanisms that control the flame stabilisation.

Analysing the edge flame statistics:

The edge-flame velocity relative to the flow depends on the displacement speed of both mixture-fraction and product mass-fraction iso-surfaces. Therefore, the response of the edge-flame propagation velocity and its components to flow and chemistry parameters, e.g. scalar dissipation rate, curvature of product mass-fraction iso-surfaces, curvature of mixture-fraction surfaces, and strain rates needs to be analysed.

1.2 Thesis outline

The remainder of thesis is organised as follows:

Chapter 2 presents a brief discussion of the stabilisation theories with supporting experimental studies from the literature. The methodology, including the governing equations, numerical methods, simulation parameters, resolution criteria and mathematical tools to explore the flame structure, are reported in chapter 3. Phenomenological descriptions of the flame structure and the stabilisation mechanism as well as examination of the flame base structure are presented in Chapter 4. Chapter 5 presents a more detailed analysis of the flame base forming a clear picture about the stabilisation mechanism of the studied lifted flame. Chapter 6 presents a comprehensive analysis of important parameters such as propagation velocities of mixture fraction and product mass-fraction iso-surfaces, scalar dissipation rate, curvature and strain rate. Finally the conclusions and suggestions for future research are summarised in chapter 7.

The results presented in chapters 4 and 5 were submitted to *Journal of Fluid Mechanics*. A main part of chapter 6 is to be submitted to *Physics of Fluids* shortly.

Chapter 2

Background

2.1 Introduction

Lifted flames occur in some types of gas turbines, in many industrial furnaces, and in several other important applications. Starting from an attached non-premixed jet flame, a lifted flame can be achieved by increasing the fuel-jet velocity such that an attached flame can no longer be supported. The flame then abruptly detaches and stabilises at some point downstream. The stabilisation location is a crucial parameter of a lifted flame. Longer lifted heights result from higher fuel injection velocities, and higher velocities are desirable to minimise the size of the fuel injection equipment and to increase the overall rate of mixing, allowing an overall smaller combustor. Longer lifted heights also lead to a greater amount of premixing before combustion, which – depending on the application – can lead to lower emissions of nitrogen oxides and/or soot. However, if the lifted height is too long, the flame can become unstable which can be a problem because of thermo-acoustic dynamics as well as leading to increased emissions of unburned hydrocarbons and carbon monoxide. In extreme conditions, the flame can completely blow off, which is obviously undesirable in any combustion system.

Because of the importance of the lifted flames in combustion systems and the importance of the stabilisation dynamics to the overall combustion behaviour, the stabilisation mechanism has been extensively investigated. As nicely summarised in some key review articles [7, 8, 22] several theories have been proposed. In the present study, we categorise and somewhat reinterpret these into four essential mechanisms which apply in an environment of oxidiser that has a temperature below the chain branching temperature such that autoignition can be ruled out. The mechanisms, which are sketched in figure 2.1, are categorised as the premixed flame theories, the edge-flame theories, the critical dissipation rate

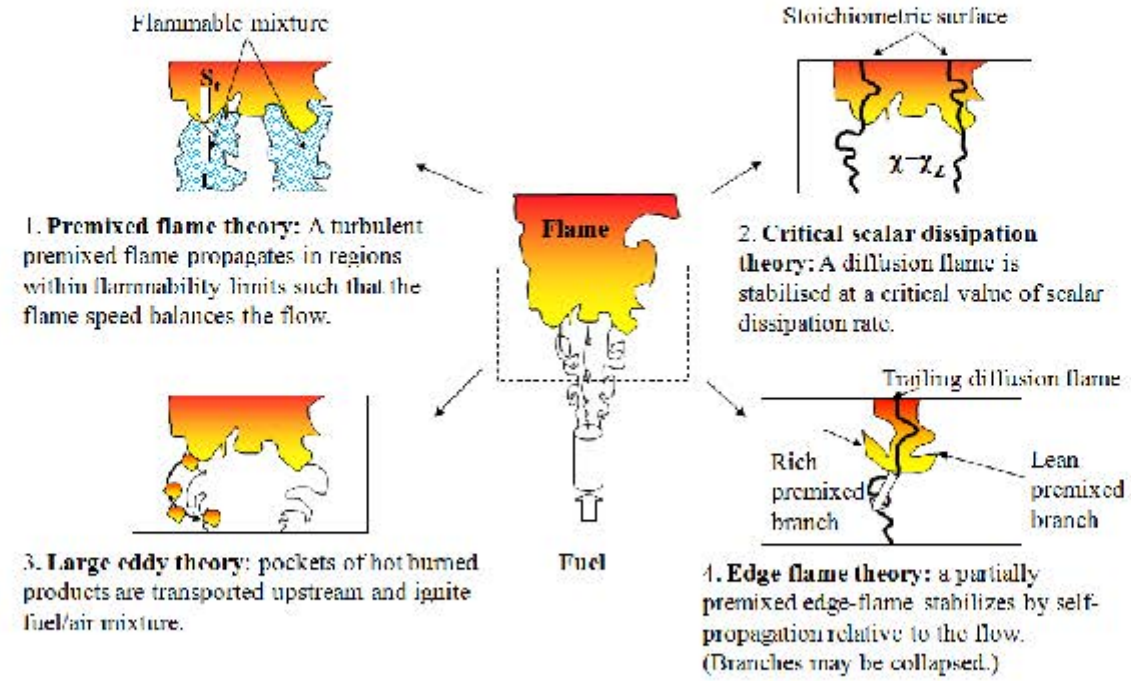

Fig. 2.1 Schematic of a lifted jet flame (centre), and different theories for the stabilisation. Specific references for these theories are discussed below.

theories, and the theories involving a role played by large eddies.

The aim of this chapter is to present a brief discussion of these theories with supporting experimental studies from the literature to reveal the more commonly accepted stabilisation mechanisms. Therefore, the structure of this chapter is as follows. First, the most accepted lifted flame stabilisation theories are described by presenting the experimental studies supporting each theory. This is followed by a brief review on the numerical simulation studies of lifted flames and the stabilisation mechanisms described by these studies.

2.2 Lifted flame stabilisation theories

2.2.1 Premixed flame theory

The first attempt to shed light on the stabilisation mechanism was the study by Vanquickenborne and Van Tiggelen [23], in which they formulated the flame base as the location where the jet average velocity is equal to the turbulent premixed flame speed,

$$S_b = U_G \ @ \ x = h, \tag{2.1}$$

where h is the lifted height, S_b and U_G are the propagation speed of the flame base and the flow velocity just ahead of the flame base, respectively. To explain the upstream flame propagation, Upatnieks *et al.* [9] added a new constraint to this theory as,

$$dS_b/dx > dU_G/dx. \tag{2.2}$$

This addition states that if the flame is moved to a downstream location, S_b will exceed U_G, so it will propagate back upstream to its equilibrium location at $x = h$. It can be postulated from this theory that the blow-out occurs not because of exceeding the flammability limits, but more often because of high jet velocity when the burning speed fails to balance the flow velocity at the flame base and the flame downstream motion is followed by blow-out.

2.2.2 Turbulent intensity theory

Later on, Kalghatgi [14] proposed the turbulent intensity theory in which the turbulent premixed flame speed is correlated by turbulence intensity. According to this theory, the turbulent burning velocity S_T, is proportional to the root mean square of velocity fluctuation, u',

$$\frac{S_T}{S_L} = b(\frac{u' l_t}{\nu})^{1/2}, \tag{2.3}$$

where b is the model constant, l_t is the turbulent length scale and $u' l_t/\nu$ is the local turbulence Reynolds number.

2.2.3 Critical scalar dissipation concept (flamelet extinction model)

Peters and Williams [24] proposed the critical scalar dissipation theory. In this theory the flame is stabilised in regions of sufficiently low scalar dissipation rate. They proposed that the turbulent flame is a group of fluctuating laminar diffusion flamelets on the reaction sheets and they are stretched and contorted by the turbulent flow. The flamelets are thin reactive diffusion layers in which chemistry is active in the thin inner layer. If the inner layer is thin enough, it will be embedded in eddies of quasi-laminar flow. In contrast, if the flow is highly turbulent and eddies are smaller, they can penetrate the inner layer and break up the flame structure resulting in flame extinction. The main stability marker in the flamelet models is the scalar dissipation rate. Based on this concept, if the scalar dissipation rate is too large, the heat loss overtakes the heat production rate and chemical reactions can not catch up with the heat dissipation. In this case, the critical value for the scalar dissipation rate marks the extinction. There have been experimental studies supporting [10] or opposing [11, 12, 25]

this theory.

Watson *et al.* [25] questioned the scalar dissipation concept by measuring the scalar dissipation rate experimentally for three Reynolds numbers of pure methane lifted flames and showed that the scalar dissipation rate for all three cases are lower than the critical quenching value of counterflow flame.

Müller *et al.* [13] observed that flame propagation is the main reason of stabilisation and the scalar dissipation rate is equal to quenching value upstream of the stabilisation location.

The common view is that the role of scalar dissipation rate in the stabilisation of the flame cannot be completely ruled out [22]. The scalar dissipation rate can alter the flame base location and would be the reason for the flame base fluctuations, however, it is not the main reason for the flame stabilisation.

2.2.4 Edge flame concept

The edge flame stabilisation mechanism, which was proposed by Buckmaster [26], is based on the concept that there should be a mechanism to enhance the propagation speed. The heat release at the edge flame causes an expansion and a divergence of streamlines which enhances the propagation speed of the edge flame (Figure 2.2). In laminar lifted flames, the

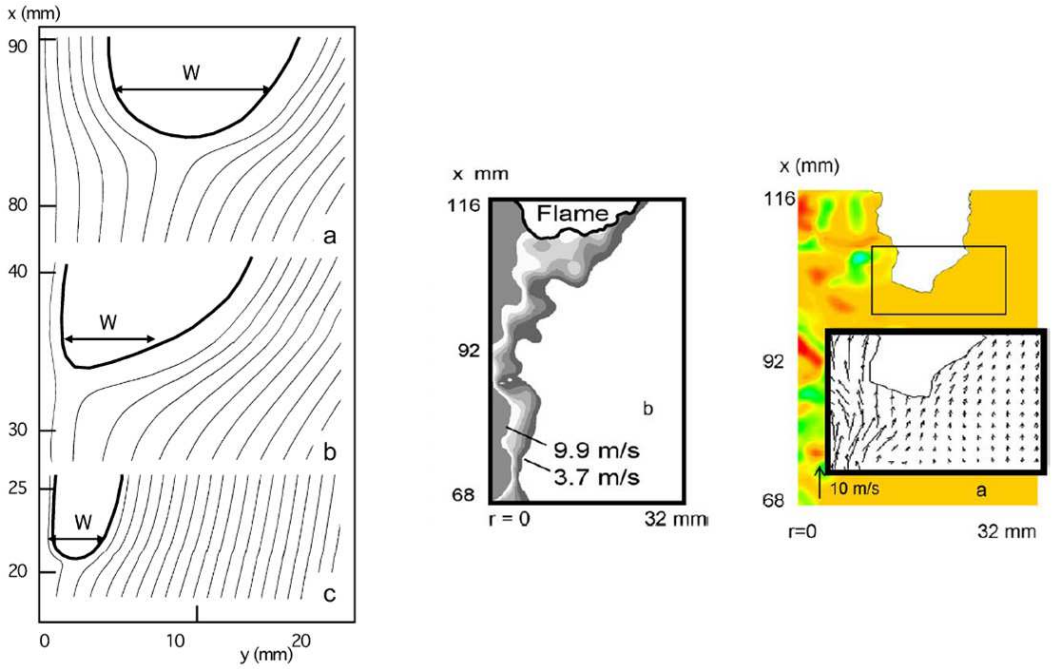

Fig. 2.2 Divergence of streamline at flame base and enhancement in leading edge width by increasing lifted length [9].

triple flame plays the main role in stabilising the flame as reported in previous experimental studies [27–30]. Figure 2.3 clearly illustrates the triple flame structure in a methane/air laminar lifted flame [27]. A triple flame consists of a diffusion flame surrounded by two rich and lean premixed flames.

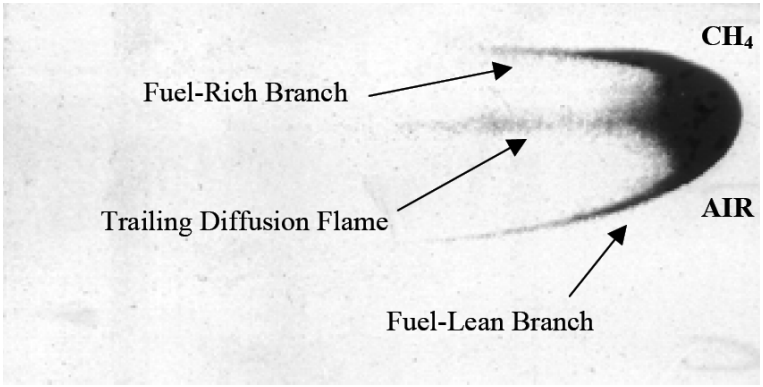

Fig. 2.3 Laminar triple flame in a methane- air flame observed by Phillips in 1965 [27].

The effects of fuel mass gradient on the behaviour of triple flames in a methane/air and propane/air laminar lifted flames were examined by Kim *et al.* [30]. As presented in figure 2.4, the two rich and lean premixed wings merge on the diffusion tail as the fuel mass gradient increases. Kioni *et al.* [28] have shown that the triple flame is affected by strain rate and tends to form a leading-edge diffusion flame. The presence of this structure is expected in turbulent lifted flames where the fuel gradient is higher due to the higher micro-mixing and strain rate [28]. The 'edge flame' or 'leading edge' is the structure formed when the wings of the lean and rich turbulent lifted flame merge with the diffusion flame. Edge-flame structures have been observed in several experimental studies of turbulent lifted

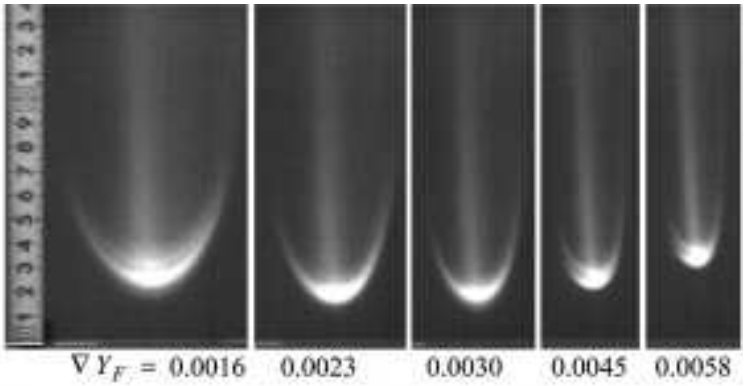

Fig. 2.4 Laminar triple flame shape for fuel concentration gradients in a methane- air flame [30].

flames [11, 15, 16, 25, 31–33]. The streamlines at the flame base diverge (see figure2.2)

and the effective propagation speed of the flame is enhanced with the difference between the flow velocity in the undisturbed flow and the flame base. The flow decelerates as it approaches the leading edge and the flame propagates towards the coming flow. Increasing the jet velocity results in movement of the flame to a downstream location and increases the streamlines divergence as discussed by Upatnieks *et al.* [9]. A schematic of this process is presented in figure 2.2.

2.2.5 Large eddy concept

There has been significant interest in the role of large eddies in flame stabilisation. Broadwell *et al.* [34] originally proposed that large structures cause hot reaction products to be ejected to the edges of the jet and then re-enter the jet together with fresh oxidiser and re-initiate combustion (Figure2.5). As discussed by Broadwell *et al.* [34], this mechanism does not completely explain the phenomena surrounding stabilisation since it cannot explain the upstream motion of a lifted flame that is ignited downstream of its lifted stabilisation point. To explain this aspect upstream transport is certainly required, but this is typically not observed experimentally. Several other works have suggested stabilisation mechanisms which

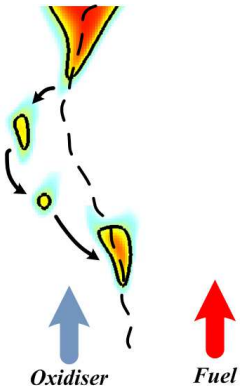

Fig. 2.5 Schematic diagram of re-entrainment of hot products into the upstream fresh mixture.

involve a strong influence of large eddies. First, it should be mentioned that all theories based on a turbulent premixed flame propagation naturally involve the effect of eddies to increase the burning velocity. What distinguishes the theories discussed below is that they involve coherent eddies associated with large scale jet organisation, while the turbulent premixed flame concept does not explicitly take this organisation into account.

Miake-Lye *et al.* [35] proposed a mechanism which is related to the critical dissipation rate concept wherein the flame is stabilised in a region where the large-scale strain rate is lower than a critical level (as opposed to the original scalar dissipation concept based on

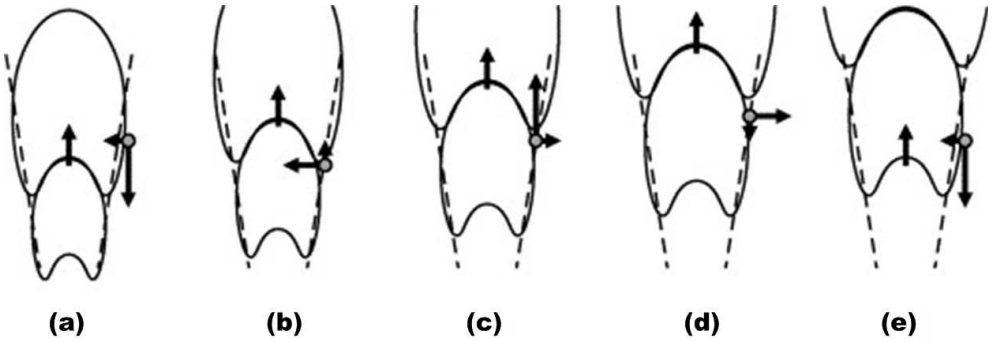

Fig. 2.6 “Schematic depiction of the flame base motion, in terms of the axisymmetric mode of large-scale organization of the mixing field. Time advances from left to right. The instantaneous stabilization point for each time is represented by a gray circle." Caption and figure from Su *et al.* [1], with permission from the authors.

small-scaled strain rate). It was proposed that the flame propagates from one structure to its upstream neighbour until the strain rate between the structures exceeds a critical value, and the flame moves downstream again. The lifted height and the inlet jet velocity was shown to have a linear correlation and this behaviour was suggested to be consistent with the proposed concept based on a self-similar form of the large-scaled strain rate field which decays inversely proportional to axial distance.

Burgess *et al.* [36] proposed another hybrid concept wherein a turbulent premixed flame is involved, but large eddies play a moderating role through outer-scale intermittency. Once intermittency was accounted for, turbulent burning velocity correlations from Ref.[37] were found to agree within a factor of two to the estimated turbulent burning velocity in the intermittent large eddies of turbulent fluid.

A theory involving both edge-flame propagation and large eddies was proposed by Su *et al.* [1]. We refer to figure 2.6, taken from Su *et al.* [1][1] to explain this idea. Since the concept is nicely stated in that article, we simply quote the explanation, and the figure’s caption.

> In (a), the stabilisation point is relatively far from the centerline, and the flame advances upstream against the low axial flow velocity. This simultaneously requires that the flame move radially inward, to maintain a flammable mixture. Eventually, the local axial flow velocity becomes sufficiently high that the flame begins to recede downstream (b). When the trailing coherent structure, which brings higher fuel mole fractions, overtakes the flame, the stabilization point moves radially outward (c). As the flame moves downstream and outward, the

[1] Permission from the authors has been obtained.

flow axial velocity decreases, until the flame once again propagates upstream (d) and the initial situation recurs (e).

A different theory involving both flame propagation and large-eddy structures to stabilisation was proposed by Lawn [22]. In this scenario as shown in figure2.7, a large structure of rich mixture departs from the fuel jet upstream of the flame and is diluted as moves toward the oxidiser stream. This flammable mixture will move downstream and eventually encounter the hot region and ignite. The ignited mixture then propagates in the shape of an edge flame or triple flame downstream within the eddy leaving the hot products behind for the next eddy to come.

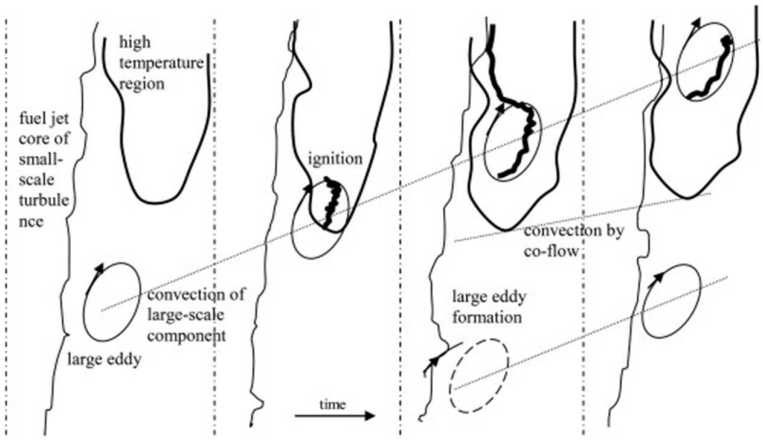

Fig. 2.7 Schematic of the proposed large eddy model by Lawn [22].

2.2.6 Out-of-plane motion

Another structure reported in the recent experimental results is the appearance of isolated flame islands. Lyons *et al.* [8] reported the presence of islands, or pockets of reaction zone upstream of the flame base. They proposed that these islands might be introduced by out-of-plane motions. The same structures were observed in a series of experimental studies by Boxx *et al.* [18, 19]. Generally, two discontinuous structures have been observed in these studies. Some occur downstream and far from the flame base which are classified as extinction holes [8, 18, 19]. The second discontinuous structure, referred to as “flame island" was observed near the flame base and is expected to play an important role in stabilisation of the flame. Gordon *et al.* [17] reported a significant out of plane velocity prior to the appearance of flame islands (Figure 2.8). They did not observed any correlation between the flame motion and turbulent intensity. Neither, there was a significant flow field divergence upstream

of the flame base. They concluded that the sudden jumps in the flame base was mainly due to the out of plane motion. However, it is challenging to measure the out of plane motion of the flow and flame experimentally. In the round jet lifted flame configuration, the mean azimuthal curvature of the flow field and also the flame sheet will cause deviation of the flame normal from the plane of imaging [38]. In the planar jet turbulent lifted flame [38], similar to the several previous round jet turbulent lifted flames experiments [11, 15, 16, 25, 31, 32] the quasi-laminar edge flame propagation has a dominant role and moreover, the turbulent flow and edge flame interaction is three-dimensional and effectual.

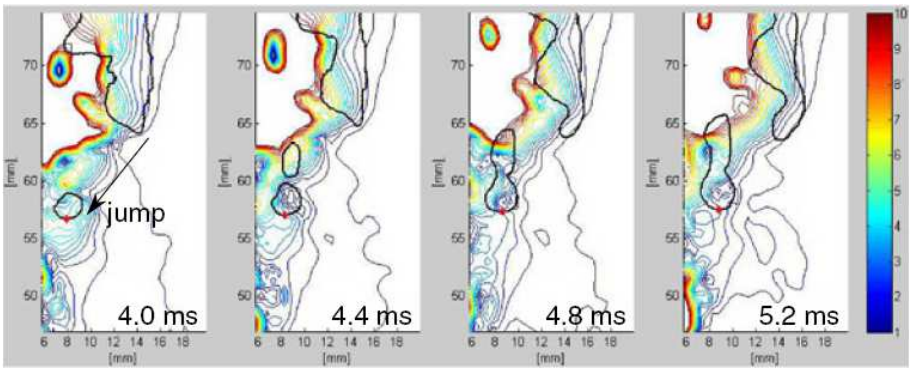

Fig. 2.8 Presence of out-of-plane velocity at the location of appearance of islands [17].

The presence of out-of-plane motion and its prominent role in closing of local extinction holes in turbulent piloted non-premixed flames of compressible natural gas (CNG) were highlighted using a new technique combines planar and volume cross imaging of laser-induced fluorescence from the hydroxyl radical [39].

2.2.7 Auto-ignition theory

Another stabilisation mechanism is auto-ignition and mainly observed in lifted flames in a vitiated co-flow. Numerical and experimental results presented by Gordon *et al.* [40, 41] are consistent with the view that auto-ignition is the main stabilisation mechanism in lifted flame with hot co-flow[2]. Yoo *et al.* [42] studied a hydrogen turbulent lifted flame in a heated co-flow using DNS. Instantaneous image of HO_2 and OH showed buildup of HO_2 prior to the creation of OH which is an indicator of auto-ignition in the flame base. Statistical behavior of the Flame Index (FI) and Damköhler number (Da) revealed that auto-ignition occurs in lean mixtures where the fuel and oxidiser gradients are opposed.

[2]The co-flow is primarily air mixed by the products of the lean premixed flame

The experimental study of the hydrogen lifted flame in a heated co-flow by Markides and Mastorakos [43] showed that auto-ignition was the main reason of the flame stabilisation in a heated co-flow. In another study of a H_2/N_2 lifted flame in a vitiated co-flow by Cabra *et al.* [44], auto-ignition was found to be the main reason for stabilisation. The study on on a methane-air lifted flame with a heated co-flow by Gordon *et al.* [45] also revealed auto-ignition as the main reason of stabilisation.

Some other studies support coexistence of different theories [6, 12]. The experimental studies of lifted flames in laboratory condition and their main parameters and findings are summarised in table A.1 in appendix A. The main conclusion from the literature is that there is no single theory which accurately describes the stabilisation mechanism in particular when the lifted height is as low as 20 times the jet width.

2.3 Numerical studies of lifted flames

Even with the most modern laser imaging tools, it is difficult to capture complex motion of the flame [46]. Although some three dimensional (3D) experimental results are presented in the literature (e.g. Coriton *et al.* [47]), three-dimensional data is not generally available. Laser Induced Fluorescence (LIF) is one of the more common techniques to measure species concentration in turbulent reacting flows. The flow is illuminated by a laser light sheet at a wavelength in which target molecules would be excited on the plane. Using intensity of reflected fluorescence, the species concentration can be captured. The lasers used in this method have a limited repetition rate. In addition to two-dimensional limitations of the optical method, variation of laser power and absorption of fluorescence are the other limiting factors. Despite rapid improvement in optical techniques both in terms of repetition rate and capability to detect other species with the multi-dimension images, the spatial and temporal accuracy is still insufficient to capture complex phenomena such as combustion waves. In addition, the experimental results only varied a few parameters and therefore the projection of the findings into other situations is difficult.

Computational Fluid Dynamics (CFD) can be used as an alternative to study turbulent lifted flames. A variety of approaches and modelling strategies have been used to study non-premixed combustion. The three main groups are: Reynolds-averaged Navier-Stokes (RANS) simulation, Large-eddy simulation (LES) and Direct numerical simulation (DNS). A review of the studies using each of these three methods are presented next.

2.3.1 Reynolds-averaged Navier-Stokes (RANS)

In the Reynolds-averaged Navier-Stokes (RANS) approach, the Navier Stokes equations are solved for ensemble means and this averaging leads to unclosed terms which need to be modelled. The main advantage of this method is its low computational cost which makes it capable of modelling industrial scale devices. Most of the commercial codes used in industry are based on this approach. Several RANS studies have been reported for lifted flames.

Gordon *et al.* [41, 48] used RANS to study a lifted methane/air flame in a vitiated co-flow stream. In this study the k-ε model was used for turbulence closure and the in situ adaptive tabulation (ISAT) method was used to reduce the computational cost of the chemistry. The budgets of convection, reaction, and diffusion were analysed in order to determine the mode of stabilisation in the flame, Gordon *et al.* [41, 48] concluded that this particular flame is stabilised by auto-ignition.

Using RANS coupled with the Eddy Dissipation Model (EDM), a lifted methane-air flame was studied by Wang and Echekki [49]. The main assumption of the EDM approach, which is originally developed by Magnussen and Hjertager [50], is a much faster chemistry compared with the rate of turbulent mixing. This approach is widely used in most commercial CFD codes. Using the k-ε model, for turbulence closure and EDM for combustion closure, Wang and Echekki [49] studied the behaviour of lifted flames for different inlet velocities. Comparison with the experimental results showed that this approach can provide a reasonable prediction of the lifted height despite its simplicity. The normalised flame index was used to analyse the flame base structure, however, the stabilisation mechanism was not discussed.

RANS models are widely used in industry to design and improve combustors. The trends have been predicted in some circumstances. However, complexity of the combustion and turbulence interaction makes RANS a less accurate approach to deal with the unsteady phenomena such as stabilisation process in a lifted flame, auto-ignition and extinction. Unsteady effects resulting from the rolling up of shear layers, swirl and recirculation zones, have a strong impact on stabilisation and extinction. The weakest point of RANS models is that by averaging quantities, details of unsteadiness are not considered.

2.3.2 Large-eddy simulation (LES)

A more accurate approach is Large-eddy simulation (LES), method in which the governing equations are spatially filtered to remove small length scales. The large length scales

greater than a user-defined filter size resolved by solving the LES equations. LES can provide a more accurate prediction of the flow field than the conventional RANS methods, in particular, for the case of complex geometries.

Large-eddy simulation seeks prediction of the motion of eddies which are larger than some user-defined length scale δ. Since its introduction [51], LES has been used to model different types of flow fields including turbulent combusting flows.

LES of lifted flames have also offered different interpretations of the stabilisation mechanisms. Jones and Navarro-Martinez [52] simulated a H_2/air jet with a co-flow of 1035–1045 K using LES and joint PDF approaches, considering a detailed chemistry model. The results were shown to be sensitive to the co-flow temperature. The lifted height was about one jet diameter larger than that of the experimental results. It was claim by the authors that the difference is due to the uncertainties of the co-flow temperature and chemical mechanism. They also found that auto-ignition is the main mechanism of stabilisation.

In a separate study by the same group [53], a combination of LES and Conditional Moment Closure (LES-CMC) was used to study the stabilisation mechanism. The simulations were set up using three experimental studies of lifted flames (Berkeley [44], Cambridge [43] and Calgary [54]) to study the different stabilisation mechanisms.The convective-diffusive-reactive terms in the species equation for different flame configurations and for different inlet conditions were analysed to investigate the stabilisation mechanism. A balance between convection, diffusion and chemical reaction provides an evidence for the stabilisation by auto-ignition mechanism. Flame stabilisation by turbulent flame propagation (Turbulent intensity theory) will require large contribution by the turbulent diffusional transport. The results of this analysis showed that the Berkeley and Cambridge flames were stabilised by auto-ignition. However, the stabilisation of the Berkeley flames depends on the co-flow temperature. For high co-flow temperatures, the flames were stabilised by auto-ignition, whereas the premixed flame theory was able to explain the stabilisation mechanism for low co-flow temperatures.

Domingo *et al.* [55] simulated a turbulent diluted methane jet flame using LES. Experimental results of the Cabra flame [44] was used to generate a look up table and to introduce a new closure model for the scalar dissipation rate of reactive species. To capture the zone of intense flow rotation, Domingo *et al.* [55] used the variable Q defined as $Q = 0.5(\omega_{ij}\omega_{ij} - S_{ij}S_{ij})$, where $\omega_{ij} = 0.5(\partial u_i/\partial x_j - \partial u_j/\partial x_i)$ and $S_{ij} = 0.5(\partial u_i/\partial x_j + \partial u_j/\partial x_i)$ are the antisymmetrical and symmetrical parts of the velocity gradient tensor, respectively. The zones in which flow rotation overtakes strain have a positive Q value. Analysing the Q iso-surfaces showed that leading edges avoid regions of intense rotation.

LES is an attractive approach for modelling non-premixed flames. The flame and flow unsteadiness are largely captured in LES and therefore it is more accurate than RANS modelling. However, the coupling between micro-mixing and chemical reactions occurring at the small-scale level is not captured directly by LES and therefore reduces the accuracy of LES.

2.3.3 Direct numerical simulation (DNS)

As discussed earlier, both RANS and LES modellings feature unclosed terms demanding needs for turbulence and combustion models. However, some important phenomena such as knock, extinction and reignition, and auto-ignition introduce a number of challenges in terms of modelling. In other words, modelling results in a loss of temporal and spatial information of the flow and flame which might affect conclusions. To eliminate a need for modelling, Direct numerical simulation (DNS) can be used as an alternative. DNS can capture the micro-mixing and its influence on reaction with a high accuracy. Since mixing is an important phenomena influencing the behaviour of non premixed flames, DNS can be a useful tool to study the resulting phenomena such as auto-ignition, quenching, reignition and the stabilisation mechanism in turbulent lifted flames. DNS results are also widely used for improvement of closure models required for RANS and LES.

Due to the high computational cost, DNS studies of lifted turbulent flames are limited to a few in the literature [20, 21, 42, 56]. The study by Yoo *et al.* [42] considered Hydrogen as a fuel in hot co-flow. The buildup of HO_2 prior to the creation of OH was considered by the authors as an evidence of stabilisation by auto-ignition, when co-flow temperature is chosen to be more than the cross-over temperature. Another study by Yoo *et al.* [56] considered an ethylene jet flame in a highly-heated co-flow. Once again, the co-flow temperature were chosen to be high enough to auto-ignite the mixture.

Mizobuchi *et al.* [20, 21] also considered Hydrogen as a fuel with an atmospheric temperature co-flow stream. They observed a vigorous inner premixed turbulent flame core and diffusion flame islands have been observed which might have been a hydrogen-specific feature due to the very lean and very rich equivalence ratios that hydrogen can burn at.

To investigate the extinction dynamics, Pantano [57] modelled non-premixed combustion of a planar methane jet with an air co-flow of 20% higher temperature than the atmospheric using DNS. The chemical mechanism was a four step reduced mechanism. A thin layer of hot co-flow was injected as a pilot to avoid blow-out. They observed that the edge flame is negatively correlated by scalar dissipation rate.

2.4 Conclusion

Different stabilisation theories were reviewed in this chapter. The main conclusion from the literature is there is no single theory which can provide an accurate prediction of the lifted height while also physically describing the stabilisation mechanism. However, it seems that the edge flame and large eddy theories and the out-of-plane motion are accepted based on the experimental results. Scalar dissipation rate plays an important role but is not the main reason of stabilisation.

Although the literature is replicated by experimental studies which suffer from lack of the third dimension. Moreover, measuring of all flame and flow dynamics simultaneously is a challenge.

Among all existing numerical approaches, DNS is the most accurate. However, due to its high computational cost, DNS is limited to highly simplified configurations for the jet flame. Of the DNS studies of turbulent non-premixed jet flames in the literature, the co-flow temperature was taken to be higher than the cross-over temperature and the auto-ignition is the dominant stabilisation mechanism. There is only the study by Mizobuchi *et al.* [20, 21] in which the co-flow has atmospheric temperature. However, this study considers hydrogen which is a fuel that can burn at very lean and rich characteristics and might have a different bahaviour compared with hydrocarbon fuels.

Therefore, the aim of this research is to perform three-dimensional DNS of a turbulent lifted flame for a hydrocarbon like fuel with a co-flow at atmospheric temperature to study the stabilisation mechanism.

Chapter 3

Methodology

3.1 Introduction

Many burners feature fuel injection into the combustion chamber at a velocity high enough to preclude rim stabilisation. The presence of a high jet velocity at the nozzle leads to stabilisation of the flame downstream of the nozzle where velocities and flame stretch rates are less severe. Recent advancements in computational technology have made it possible to model turbulent lifted flames with direct numerical simulation (DNS), however the computational cost is still high and therefore the 3D DNS studies are limited to few cases [20, 21, 42, 56, 58]. Single step chemistry is able to capture the basic behaviour of conventional fuels with significantly reduced computational cost, thus allowing larger computational domains and higher Reynolds numbers.

This chapter presents the governing equations and numerical methods used to study a turbulent lifted flame. The simulation parameters and resolution criteria are discussed in detail next. Finally, the mathematical concepts used for post-processing are introduced.

3.2 Governing equations

For a single-step irreversible reaction of $F + rO \rightarrow (1+r)P$ in which r is the stoichiometric ratio, i.e. the mass of oxidant disappearing with unit mass of fuel, the following system of

equations is solved,

$$\begin{aligned}
\frac{\partial \rho^*}{\partial t^*} + \frac{\partial \rho^* U_i^*}{\partial x_i^*} &= 0, \\
\frac{\partial \rho^* U_j^*}{\partial t^*} + \frac{\partial \rho^* U_i^* U_j^*}{\partial x_i^*} &= -\frac{\partial p^*}{\partial x_j^*} + \frac{\partial \tau_{ij}^*}{\partial x_i^*}, \\
\frac{\partial \rho^* E^*}{\partial t^*} + \frac{\partial U_j^* (\rho E^* + p^*)}{\partial x_j^*} &= \frac{\partial U_j^* \tau_{ij}^*}{\partial x_j^*} - \frac{\partial q_j^*}{\partial x_j^*} - Q\dot{\omega}_F^*, \\
\frac{\partial \rho^* Y_F^*}{\partial t^*} + \frac{\partial \rho^* U_j^* Y_F^*}{\partial x_j^*} &= \frac{\partial}{\partial x_j^*}\left(\rho^* D^* \frac{\partial Y_F^*}{\partial x_j^*}\right) - \dot{\omega}_F^*, \textit{ and} \\
\frac{\partial \rho^* Y_O^*}{\partial t^*} + \frac{\partial \rho^* U_j^* Y_O^*}{\partial x_j^*} &= \frac{\partial}{\partial x_j^*}\left(\rho^* D^* \frac{\partial Y_O^*}{\partial x_j^*}\right) - \dot{\omega}_O^*,
\end{aligned} \tag{3.1}$$

where

$$\begin{aligned}
p^* &= \rho^* R^* T^*, \textit{and} \\
\tau_{ij}^* &= \mu^* \left[\frac{\partial u_i^*}{\partial x_j^*} + \frac{\partial u_j^*}{\partial x_i^*} - \frac{2}{3}\frac{\partial u_k^*}{\partial x_k^*}\delta_{ij}\right],
\end{aligned} \tag{3.2}$$

where the variable μ^* is the molecular viscosity and δ_{ij} is the Kronecker delta. Variations of viscosity due to temperature were taken into account by the classical law, $\frac{\mu^*}{\mu_{ref}} = (\frac{T^*}{T_{ref}})^{0.75}$ where μ_{ref} is molecular viscosity at reference temperature T_{ref}. The sensible energy in equation (3.1) is defined as follow [59, 60]:

$$E^* = c_v^* T^* + \frac{1}{2} U_i^* U_i^*, \tag{3.3}$$

The energy flux in equation 3.1 is defined as

$$q_i^* = -k^* \frac{\partial T^*}{\partial x_i^*} \tag{3.4}$$

Using Arhenius law, fuel and oxidizer consumption rates are given by [59, 60]:

$$\begin{aligned}
\dot{\omega}_F^* = \frac{1}{r}\dot{\omega}_O^* &= -A^* \rho^2 Y_F^* Y_O^* \exp\left[-\frac{\beta(1-T'^*)}{1-\alpha(1-T'^*)}\right], \\
\text{where } T'^* &= \frac{T^* - T_o^*}{T_{ad}^* - T_o^*}.
\end{aligned} \tag{3.5}$$

The variable A^* is the pre-exponential factor, T_o^* is the ambient temperature, T_{ad}^* is the adiabatic flame temperature of stoichiometric mixture, α is heat-release parameter given by

$(T^*_{ad} - T^*_o)/T^*_{ad}$ and β is Zeldovich factor given by

$$\beta = \frac{\left[E_a(T^*_{ad} - T^*_o)\right]}{RT^{*2}_{ad}}, \tag{3.6}$$

where E_a is the activation energy and R is the universal gas constant. To avoid computational truncation errors, the conservation equations are solved in non-dimensional form. The following non-dimensional variables are defined:

$$\begin{array}{lllll} x_j = \frac{x^*_j}{H}, & U_j = \frac{U^*_j}{a^*_o}, & \rho = \frac{\rho^*}{\rho^*_o}, & t = \frac{t^* a^*_o}{H}, & p = \frac{p^*}{\rho^*_o a^{*2}_o}, \quad T = \frac{T^*}{(\gamma-1)T^*_o}, \\ \mu = \frac{\mu^*}{Re\mu^*_o}, & \mathrm{Pr} = \frac{\upsilon^*}{\alpha^*}, & Le = \frac{\alpha^*}{D^*}, & Re = \frac{\rho^*_o a^*_o H}{\mu^*_o}, & Da = A\frac{H\rho^*_o}{a^*_o}, \quad Sc = LePr, \end{array} \tag{3.7}$$

where $\mathrm{x_j}$ is the spatial vector, H is the inlet jet width, $\mathrm{U_j}$ is the velocity vector, a is the speed of sound, ρ is the density, T is the temperature, t is the time, p is the pressure, γ is the heat capacity ratio, μ is the dynamic viscosity which is given by $\mu/\mu_\mathrm{o} = (\mathrm{T}/\mathrm{T_o})^{0.7}$, Re is Reynolds number, Le is Lewis number, Pr is Prandtl number, Sc is Schmidt number and A is the pre-exponential factor in Arrhenius law. The superscript $*$ represents the dimensional values and the subscript o is the fuel stream conditions at the inlet. Therefore, the non-dimensional inlet temperature is 2.5 considering $\gamma = 1.4$. The non-dimensional form of the equations are,

$$\begin{aligned} &\frac{\partial \rho}{\partial t} + \frac{\partial \rho U_i}{\partial x_i} = 0, \\ &\frac{\partial \rho U_i}{\partial t} + \frac{\partial \rho U_i U_j}{\partial x_j} = -\frac{\partial p}{\partial x_j} + \frac{\partial \tau_{ij}}{\partial x_j}, \\ &\frac{\partial \rho E}{\partial t} + \frac{\partial U_j(\rho E + p)}{\partial x_j} = \frac{\partial U_j \tau_{ij}}{\partial x_j} - \frac{\partial q_j}{\partial x_j} - \frac{\tau \dot{\omega}_F}{Y_{Fst}(\gamma-1)}, and \\ &\frac{\partial \rho Y_k}{\partial t} + \frac{\partial \rho U_j Y_k}{\partial x_j} = \frac{\partial}{\partial x_j}\left(\frac{1}{Sc}\mu\frac{\partial Y_k}{\partial x_i}\right) + \dot{\omega}_k,\ k = F, O\ , \end{aligned} \tag{3.8}$$

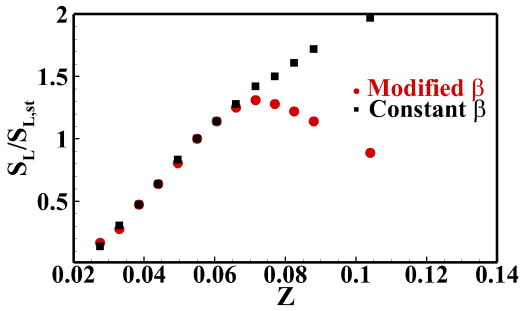

Fig. 3.1 Laminar flame speed dependency on mixture fraction with and without modification.

where

$$
\begin{aligned}
p &= \frac{\gamma-1}{\gamma}\rho T, \\
\tau_{ij} &= \mu\left[\frac{\partial U_i}{\partial x_j}+\frac{\partial U_j}{\partial x_i}-\frac{2}{3}\frac{\partial U_k}{\partial x_k}\delta_{ij}\right], \\
q_i &= -\frac{\mu}{\mathrm{Pr}}\frac{\partial T}{\partial x_i}, \\
\dot{\omega}_F &= \frac{1}{r}\dot{\omega}_O = -Da.\rho^2 Y_F Y_O \exp[-\frac{\beta(1-T')}{1-\alpha(1-T')}], \\
T' &= \frac{(\gamma-1)T-1}{\tau}, \\
E &= \frac{T}{\gamma}+\frac{1}{2}U_k U_k, \\
\tau &= \alpha/(1-\alpha), \\
\alpha &= \frac{(\gamma-1)T_{ad}-1}{(\gamma-1)T_{ad}}, \text{and} \\
Y_{Fst} &= \frac{Y_{F,o}}{1+rY_{F,o}/Y_{O,o}},
\end{aligned}
\tag{3.9}
$$

where τ_{ij} is the shear tensor, q_i is the heat flux, $\dot{\omega}_F$ is the fuel reaction rate, Y is the mass fraction, E is the sensible energy, T_{ad} is the adiabatic flame temperature and the subscripts F and O are fuel and oxidiser, respectively. Single-step chemistry with a constant Zel'dovich number suffers from a known deficiency that it over-predicts the laminar burning rate on the rich side. Given the significant role played by the flame speed in lifted flame stabilisation [61], it was considered important to rectify this problem. The approach adopted here uses a modified activation energy as suggested by Garrido-López and Sarkar [62] that was demonstrated to capture the experimentally observed dependence of the laminar burning rate s_L with equivalence ratio, in particular the significant reduction of s_L in very rich mixtures.

The Zel'dovich number is modified, as follows:

$$\beta(\phi) = \begin{cases} \beta_0(1+8.25(\phi-0.64)^2) & \phi \leq 0.64 \\ \beta_0 & 0.65 < \phi < 1.07 \\ \beta_0(1+1.443(\phi-1.07)^2) & \phi \geq 1.07 \end{cases}, \tag{3.10}$$

where $\beta_0 = 5.0$ in this study and ϕ is the local equivalence ratio. The dependency of the laminar flame speed normalized by the maximum laminar flame speed is presented for both cases with and without modification of the Zel'dovich number in figure 3.1.

3.3 Numerical solver

The DNS code S3D_SC is employed here. S3D_SC is a modified version of the detailed chemistry code S3D [63] and solves equations 3.1. The original DNS code S3D has been used in a large number of studies of combustion [42, 56, 63–72]. Like S3D, the solver S3D_SC uses high-order accurate, low dissipative numerical schemes and a 3D structured, Cartesian mesh. The spatial derivatives were computed using an 8^{th} order central differencing scheme and the time integration was performed with a 6-stage, 4^{th} order, explicit Runge-Kutta method. To suppress the numerical fluctuations at high wave numbers, a 10^{th} order filter [73] was applied to the solution vector every 10 time steps.

3.4 Simulation parameters and boundary conditions

The configuration is a slot jet flame similar to that studied in [42, 56] and is presented schematically in figure 3.2. The mean inlet axial velocity, U_{in} (and fuel mass fraction Y_F), were specified using a tanh-based profile as,

$$U_{in} = U_c + \frac{U_j - U_c}{2}\left(tanh\left(\frac{y+H/2}{2\delta}\right) - tanh\left(\frac{y-H/2}{2\delta}\right)\right), \tag{3.11}$$

where U_c and U_j are the mean co-flow and mean inlet jet velocities and the inlet momentum (and mixing layer) thickness, δ, is equal to 0.05H. To describe the velocity fluctuations at the inlet,u , a homogeneous isotropic turbulence field based on a prescribed turbulent energy spectrum [74] with a turbulence intensity of 5% is first produced. These velocity fluctuations are then added to the mean inlet velocity using the Taylor's frozen turbulence hypothesis [42, 56]. The same profile as inlet flow velocity was used for fuel and oxidizer and the inlet profiles are presented in figure 3.3. To determine appropriate simulation parameters, the bulk parameters were approximately matched with a case reported in Ref.

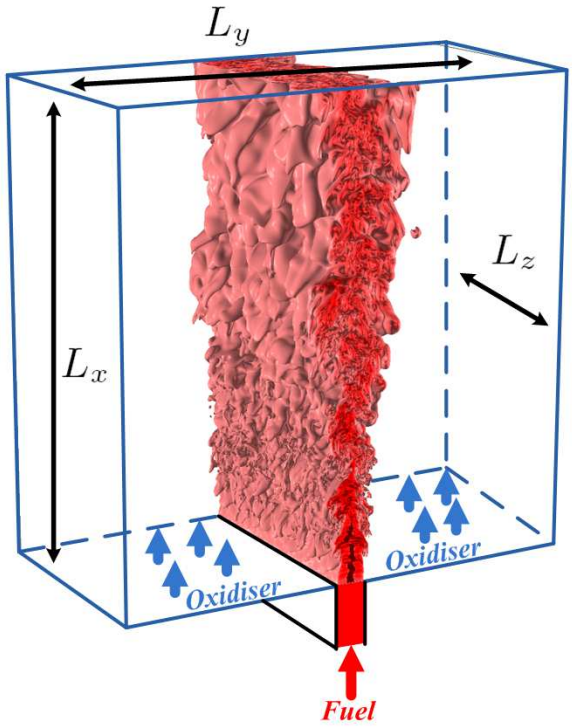

Fig. 3.2 Schematic of domain and configuration of this study.

Table 3.1 Numerical and physical parameters of the simulation

Jet width	H
Domain size ($L_x \times L_y \times L_z$)	$16H \times 24H \times 8H$
Number of grid points ($N_x \times N_y \times N_z$)	$800 \times 800 \times 400$
Mean inlet jet non-dimensional velocity (U_j)	0.48
Co-flow non-dimensional velocity ($U_{co-flow}$)	0.001
Jet non-dimensional temperature	2.5
Co-flow non-dimensional temperature	2.5
Jet Reynolds number	5,280
Inlet velocity fluctuation	5%
Fuel mass fraction in fuel stream ($Y_{F,o}$)	1.0
Oxidiser mass fraction in oxidiser stream ($Y_{O,o}$)	0.233
Stoichiometric mixture fraction (Y_{Fst})	0.055
Stoichiometric oxidiser to fuel mass ratio r	4.0
Heat release parameter (α)	0.86
Ratio of specific heat (γ)	1.4
Baseline Zel'dovich number (β_0)	5.0
Non-dimensionisation Damköhler number (Da)	800.0
Prandtl number (Pr)	0.7
Lewis number (Le=Sc/Pr)	1.0

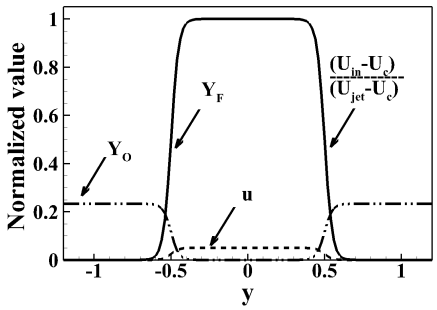

Fig. 3.3 Mean profiles of the axial velocity, fuel and oxidiser mass fractions at the inlet.

[75]. Therein, S_L/U_{jet}=0.013, δ_L/H=0.13, and Re=5280 while in our simulation we have S_L/U_{jet} =0.016, δ_L/H=0.16, Re=5,280 (Note: however that the experimental work considered a round jet while the DNS considered a slot jet, as it is a computationally cheaper geometry). The simulation parameters along with their values are presented in table 3.1. A uniform grid spacing of $0.02H$ was chosen for the streamwise and spanwise directions. An algebraically stretched mesh was applied [69] in the transverse direction which maintained uniform spacing of $0.02H$ in $|y| < 7.5H$ and less than 3% of grid stretching in the region of $|y| > 7.5H$. To enable very long-time simulations, a sponge region was used in the transverse direction in the region of $|L_y| > 10H$. In the sponge region, exponential damping terms were added to the governing equations [76].

$$\frac{\partial U^*}{\partial t} = \text{ Standard terms} - d_f(x,y)(U^* - U^*_{target}) \text{ and}$$
$$d_f(x,y) = \sigma(\frac{x-x_s}{L_x})^\zeta, \tag{3.12}$$

where U^* represents the conservative variables, U^*_{target} is the target values and are initial conditions in the domain, d_f is the damping function and the damping parameters σ and ζ are constant and there are 10.0 and 4.0 respectively in this simulation. x_s is the start point of the sponge region. This prevents instabilities developing where a net transverse velocity drift through the domain exists. The simulation was run for 18.0 jet flow through times, $t_j = L_x/U_j$ (where the L_x is the length of the computational domain in the streamwise direction), to obtain a statistically stationary solution the data of the last $12.0t_j$ were used for analysis.

Non-reflecting outflow boundary conditions were used in the streamwise and transverse directions [77–79].

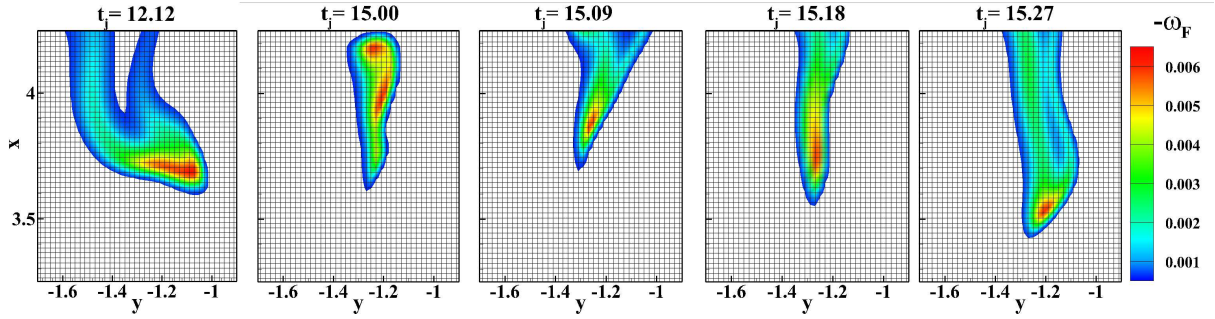

Fig. 3.4 Temporal evolution of the reaction rate contour plots with presence of grid structure for a typical (left) and worst case (right) scenario of local extinction at plan z=0.0.

3.5 Turbulence and flame resolution

The resolution of turbulence was assessed considering the Kolmogorov scale defined as $\tilde{\eta}_k = (\tilde{\nu}^3/\tilde{\varepsilon})^{1/4}$. The minimum $\tilde{\eta}_k/dx$ at the flame base is roughly 0.5 and most of the time the flame is located in the region of $\tilde{\eta}_k/dx > 0.5$. This resolution is normally considered sufficient for DNS [80].

To give an indication of the flame resolution, the thermal thickness of a symmetric laminar triple flame was calculated. The thermal thickness was equal to 0.16, and there are 8 grid points across this region, which is normally considered sufficient for one-step chemistry DNS, e.g. [81, 82]. To examine whether this resolution criteria is adequate in the presence of turbulence and high dissipative structures in the reaction zone, contour plots of the reaction rate in the worst case scenario of local extinction are presented on the grid in figure 3.4. Figure 3.4 shows that there are almost 8 grid points in the reaction zone which is considered to be sufficient in DNS of single step chemistry. Temperature on the mixture fraction iso-line crossing the flame base was extracted and presented in figure 3.5. All the symbols are representing the grid points and, as can be seen for $t_{jet} = 11.85, 11.94, 12.03$, there are more than 8 grid points across the thermal thickness. In addition at $t_{jet} = 12.12$, when there is a sharp drop and raise in temperature, there are sufficient grid points to resolve this sudden change. To do a more sophisticated analysis the thermal thickness can be defined as $\delta_{th} = (T_{ad} - T_o)/(\frac{\partial T}{\partial x})$, where T_{ad} is the adiabatic flame temperature, T_o is the unburned mixture temperature and x is the streamwise direction. Calculating this value for the temperature profiles presented in Fig. 3.5 shows values of 0.17, 0.14, 0.2 and 0.15 for the thermal thickness. As such, there are 7 and more grid points across this region, which is normally considered sufficient for one-step chemistry DNS, e.g. [81, 82].

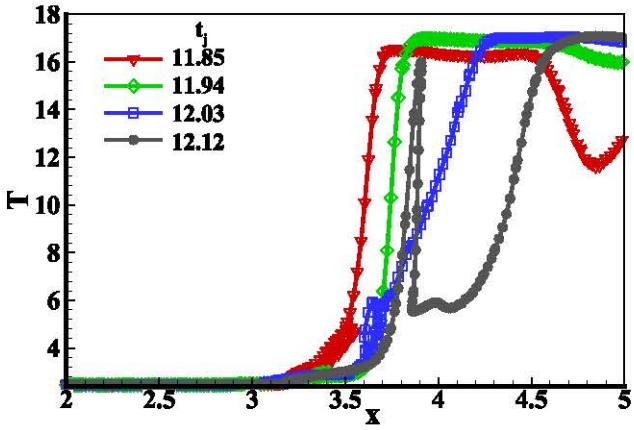

Fig. 3.5 Temperature extracted on the mixture fraction iso-line of 0.07 at the plane z=0.0 corresponding to the time sequences (the solid line is the $Z = 0.07$).

3.6 Flame diagnostics

In this section, the main parameters which will be used to understand the flame base characteristics are introduced.

3.6.1 Scalar dissipation rate

The scalar dissipation rate can be used to examine the rate of molecular mixing and is also the key parameter in many models for turbulent non-premixed combustion. Some experimental and theoretical studies showed that if the scalar dissipation is close to the ignition or extinction limits, dissipation effects can play an important role in determining the stabilisation location [10, 13, 24, 83]. The non-dimensional scalar dissipation rate is defined as

$$\chi = \frac{2\mu}{\rho \mathrm{Sc}} |\nabla Z|^2. \tag{3.13}$$

3.6.2 Normalised flame index (NFI)

The flame index (FI) representing the degree of mixedness was proposed by Yamashita *et al.*[84] to distinguish premixed from non-premixed flames. They defined the F.I. as a cosine of oxidizer and fuel gradient,

$$F.I. = \nabla Y_F \bullet \nabla Y_O. \tag{3.14}$$

Bray *et al.* [85], Domingo *et al.* [86] and Knudsen *et al.*[87] have used a normalized flame index (NFI), defined as

$$\mathrm{NFI} = \frac{\nabla \mathrm{Y_F} \bullet \nabla \mathrm{Y_O}}{|\nabla \mathrm{Y_F} \bullet \nabla \mathrm{Y_O}|}. \tag{3.15}$$

In areas that are burning (i.e. having a non-negligible reaction rate), the NFI can be used to determine the combustion mode. When the fuel and oxidiser gradients are aligned, this term is positive and indicates the presence of a premixed flame, while when these gradients are not aligned, the NFI will be negative indicating the presence of a non-premixed flame.

3.6.3 Edge flame identification and velocity

As stated in the introduction, one of the main objectives here is to analyse the edge-flame velocity. To achieve this, we first need to identify the flame base. Different approaches have been used for this purpose. In experimental studies of hydrocarbon flames, commencement of chemiluminescence of CH^* [1], CH-PLIF [8, 31, 88, 89] or OH-PLIF [17–19] has frequently been used as the flame base marker. The excited CH^* radical is short-lived and thought to mark the instantaneous reaction zone [1]. These locations coincide with high heat release rate.

In DNS of premixed flames, the high heat release region is often marked by a critical value of a reacting scalar [71, 72, 90–97]. In our case, a more involved approach is needed since we wish to separate the edges from the region downstream. Following earlier studies of extinction and reignition [57, 98, 99], we therefore select a edge-flame marker that is the intersection of a mixture-fraction iso-surface and a product mass-fraction iso-surface.

To select the mixture-fraction iso-value, it was first assumed that the leading edge would be found at the mixture fraction having the highest laminar flame speed, which is slightly rich of stoichiometric (0.07 in this study). To select the product mass-fraction iso-surface, a one-dimensional (1D) simulation of a laminar premixed flame having the same flame parameters as the turbulent lifted flame was performed. The product mass fraction corresponding to the location of maximum heat release rate was obtained from this simulation. The obtained value of Y_p was 0.2.

To extract the intersecting contour, the iso-surface of mixture fraction was triangulated with a parallel implementation of the marching-cubes algorithm. The edges of the resulting triangles were then searched for intersections with the product mass fraction iso-surface, and the intersection location was linearly estimated based on the vertex values of the product mass fraction. Quantities were then linearly interpolated to the intersection locations. It was verified that the mixture fraction and product mass fraction interpolated to the edge

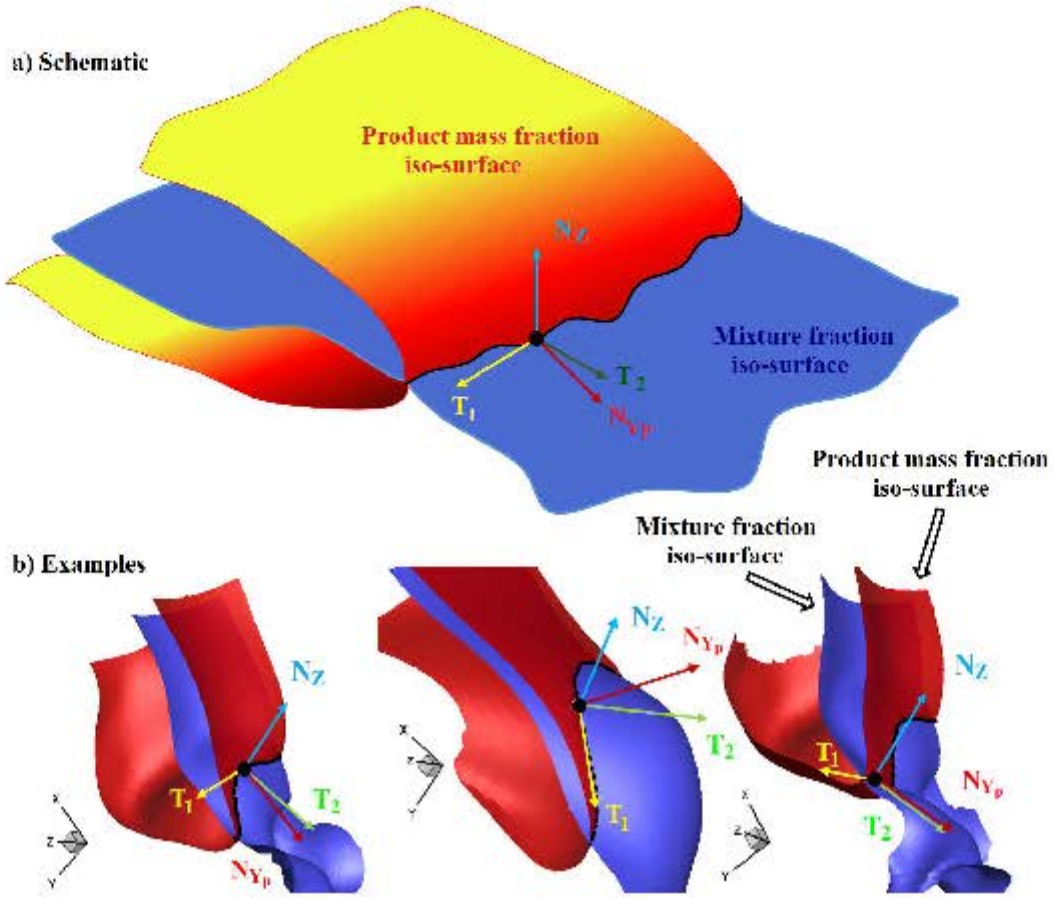

Fig. 3.6 The various normal and tangential vectors at the flame base, a) schematic and b) examples (the red-yellow surfaces are the product mass fraction iso-surface; the blue surface are the mixture-fraction iso-surface; and the solid black line is the identified edge-flame).

flames returned the expected values to typically within 1%. The resulting edge-flame regions from the turbulent flame DNS were then extensively visualised and compared with locations of high heat release. It was found that the leading edge flame as identified visually from reaction rate always remained very close to the intersection of the two iso-surfaces.

Flame edges defined in this way can move by three mechanisms: flow, motion relative to the flow of the product mass fraction iso-surface, and motion relative to the flow of the mixture-fraction iso-surface. Although the velocity tangential to the flame edge could be arbitrarily specified, we take it to be equal to the flow velocity, following previous works on flame surface evolution [100], and on the tracking of extinction holes [57].

To determine the edge motion, we first need a coordinate system, which we take to be moving with the flow velocity. Referring to figure 3.6, we define a tangent vector to the mixture-fraction iso-surfaces which points along the flame edge. Clearly, $\boldsymbol{T}_1$ is normal to

both the normal to the mixture-fraction iso-surface $\boldsymbol{N}_Z$ (pointing towards oxidiser) and to the normal to the product mass-fraction iso-surface $\boldsymbol{N}_{Y_p}$ (pointing towards reactants). Next, we define another vector $\boldsymbol{T}_2$ which is also tangential to the mixture-fraction iso-surface but normal to $\boldsymbol{T}_1$, and pointing towards the reactants. It is readily shown that these quantities are given by:

$$\begin{aligned}
\boldsymbol{N}_Z &= -\frac{\nabla Z}{|\nabla Z|}, \\
\boldsymbol{N}_{Y_p} &= -\frac{\nabla Y_p}{\left|\nabla Y_p\right|}, \\
\boldsymbol{T}_1 &= \frac{\boldsymbol{N}_{Y_p} \times \mathbf{N}_Z}{\left|\boldsymbol{N}_{Y_p} \times \mathbf{N}_Z\right|}, \\
\boldsymbol{T}_2 &= \frac{\mathbf{N}_Z \times (\boldsymbol{N}_{Y_p} \times \mathbf{N}_Z)}{\left|(\boldsymbol{N}_{Y_p} \times \boldsymbol{N}_Z)\right|} \\
&= \frac{\boldsymbol{N}_{Y_p} - \boldsymbol{N}_Z(\boldsymbol{N}_{Y_p} \cdot \boldsymbol{N}_Z)}{\sqrt{1-(\boldsymbol{N}_{Y_p} \cdot \boldsymbol{N}_Z)^2}}, \\
\boldsymbol{T}_3 &= \frac{\boldsymbol{T}_1 \times \boldsymbol{N}_{Y_p}}{\left|\mathbf{T}_1 \times \boldsymbol{N}_{Y_p}\right|}.
\end{aligned} \tag{3.16}$$

Figure 3.7 now shows a schematic, in the plane containing both $\boldsymbol{N}_Z$ and $\boldsymbol{N}_{Y_p}$, of the edge-point motion during an infinitesimal interval of time δt. Because the chosen coordinate system moves with the local flow velocity, only the motion of the iso-surfaces relative to the flow need be considered. During this time interval, the mixture-fraction iso-surface is displaced by $S_Z \boldsymbol{N}_Z \delta t$, while the $Y_p = Y_p^*$ iso-surface is displaced by $S_d \boldsymbol{N}_{Y_p} \delta t$, where the displacement speeds are given by [71, 100, 101] as

$$\begin{aligned}
S_Z &= \frac{1}{\rho \mid \nabla Z \mid} \left(-\frac{\partial}{\partial x_j} \left(\frac{\mu}{\mathrm{Sc}} \frac{\partial Z}{\partial x_j} \right) \right), \text{ and} \\
S_d &= \frac{1}{\rho \mid \nabla Y_P \mid} \left(-\dot{\omega}_P - \frac{\partial}{\partial x_j} \left(\frac{\mu}{\mathrm{Sc}} \frac{\partial Y_P}{\partial x_j} \right) \right).
\end{aligned} \tag{3.17}$$

We denote the overall displacement of the edge point $\boldsymbol{V}_e \delta t$ and break this down in the orthonormal coordinates $\boldsymbol{N}_Z$ and $\boldsymbol{T}_2$ as:

$$\boldsymbol{V}_e \delta t = S_z \boldsymbol{N}_Z \delta t + S_e \boldsymbol{T}_2 \delta t, \tag{3.18}$$

where $S_e = \boldsymbol{V}_e \bullet \boldsymbol{T}_2$ is the projection of $\boldsymbol{V}_e$ into in the plane of the mixture-fraction iso-surface and needs to be determined. By dividing by δt, and taking the dot product of

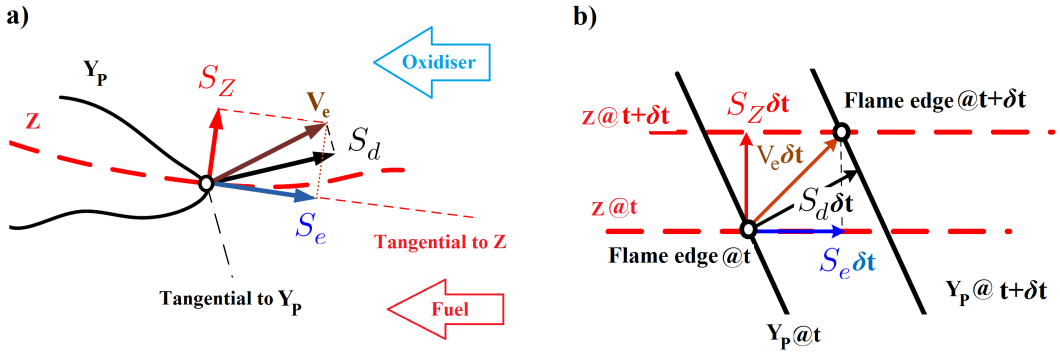

Fig. 3.7 Schematic of edge-flame propagation along the mixture-fraction iso-surface: a) instantaneous vectors and indicative flame edge; b) propagation of the edge point over an infinitesimal time interval δt.

equation3.18 with $\boldsymbol{N}_{Y_p}$, it is readily shown that:

$$S_e = \frac{S_d - kS_Z}{\sqrt{1-k^2}}, \tag{3.19}$$

where k is the inner product of the normal vectors $\boldsymbol{N}_{Y_p} \bullet \boldsymbol{N}_Z$.

Although the presentation here is slightly different, we have verified that the final result is the same edge speed used first by [57] to study extinction holes, and later by [98, 99] to study extinction and reignition, and also by [102] to study ignitions.

To provide a better interpretation of the observed edge flame speeds, some normalisation is required. In premixed combustion, where S_d is the relevant speed, a density-weighted normalisation is often applied to correct for expansion across the flame:

$$S_d^*/S_L = \frac{\rho S_d}{\rho_u S_L}, \tag{3.20}$$

where ρ_u is the unburned gas density and S_L is the laminar flame speed. This is equivalent to normalising by the S_d value at the $Y_p = Y_p^*$ iso-surface in the unstrained 1D laminar flame, which we denote $S_{d,L}$. In the case of an edge-flame, the normalisation is less straightforward because the expansion across the flame is less than ρ_u/rho due to streamline divergence around the edge-flame. However, there does not seem to be a straightforward way to define an appropriate density correction because the amount of streamline divergence is dependent on the mixture-fraction gradient. Therefore, following previous studies of edge flames [59, 71, 72, 91, 98, 99, 103], we simply adopt the same normalisation as used in premixed

combustion to normalise all of the relevant speeds, i.e.:

$$\begin{aligned}\frac{S_e^*}{S_L} &= \frac{S_e}{S_{d,L}}, \text{ and} \\ \frac{S_Z^*}{S_L} &= \frac{S_Z}{S_{d,L}}.\end{aligned} \tag{3.21}$$

To investigate the contribution of different terms in equations 3.17, the normalised displacement speeds are decomposed as [71],

$$\begin{aligned}S_{d,n}^* &= \frac{1}{S_{d,L}} \frac{\boldsymbol{N}_{Y_p} \bullet \nabla \left(\rho D \boldsymbol{N}_{Y_p} \bullet \nabla Y_p\right)}{\rho \mid \nabla Y_p \mid}, \\ S_{d,t}^* &= \frac{-1}{S_{d,L}} \frac{\mu}{\mathrm{Sc}} \frac{\kappa_{Y_p,m}}{\rho}, \\ S_{d,r}^* &= \frac{1}{S_{d,L}} \frac{\dot{\omega}_P}{\rho \mid \nabla Y_p \mid}, \\ S_{Z,n}^* &= \frac{-1}{S_{d,L}} \frac{\boldsymbol{N}_Z \bullet \nabla \left(\rho D \boldsymbol{N}_Z \bullet \nabla Z\right)}{\rho \mid \nabla Z \mid}, \text{ and} \\ S_{Z,t}^* &= -\frac{\mu}{\mathrm{Sc}} \frac{\kappa_{Z,m}}{\rho},\end{aligned} \tag{3.22}$$

where κ_{Y_p} is the curvature of the product mass fraction iso-surface defined as $\nabla \bullet \boldsymbol{N}_{Y_p}$ and κ_Z is the mixture-fraction surface curvature defined as $\nabla \bullet \boldsymbol{N}_Z$. The subscript n, t and r represent the components resulting from diffusion normal to product mass fraction iso-surfaces, diffusion tangential to product mass-fraction iso-surfaces, and reaction terms, respectively.

Strain can be an important parameter for edge flame response, and is often cast in terms of the total strain in the tangent plane of an iso-surface, or the component of strain in the normal direction. These strain rates are given as [100, 104]:

$$\begin{aligned}a_{t,Y_p} &= (\delta_{ij} - N_{Y_p i} N_{Y_p j}) \frac{\partial u_i}{\partial x_j}, \\ a_{n,Y_p} &= N_{Y_p i} N_{Y_p j} \frac{\partial u_i}{\partial x_j}, \\ a_{t,Z} &= (\delta_{ij} - N_{Zi} N_{Zj}) \frac{\partial u_i}{\partial x_j} \text{ and} \\ a_{n,Z} &= N_{Zi} N_{Zj} \frac{\partial u_i}{\partial x_j}.\end{aligned} \tag{3.23}$$

In the subscripts Y_p and Z represent the strain rates on the respective iso-surfaces of those variables while n and t represent normal and tangential components.

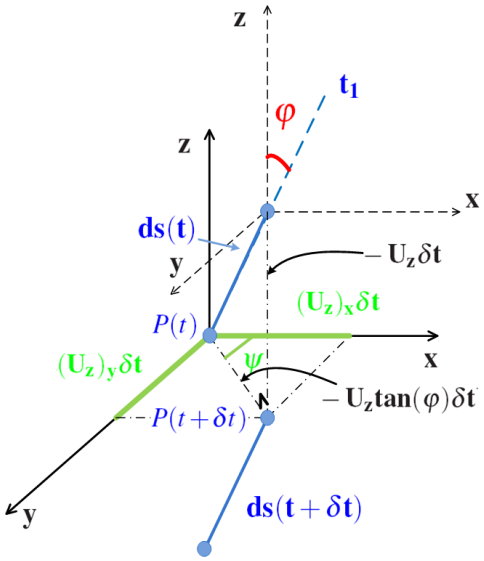

Fig. 3.8 Schematic of displacement of edge in the transverse and streamwise directions caused by out-of-plane motion.

3.6.4 Out-of-plane motion

Many experimental investigations of lifted flames have used laser-based planar measurements [7, 10, 11, 14, 16, 23, 25, 31, 35, 61, 105–120], and therefore there have been numerous questions raised about out-of-plane motion and its potential role in flame stabilisation. Out-of-plane motion of the flame is the consequence of two effects: flow motion and flame propagation. The out-of-plane flow velocity has recently become accessible in cinema particle image velocimetry (PIV) experiments (e.g. Gordon *et al.*[17], Boxx *et al.* [18, 19, 38] and Lyon *et al.* [8]). The flame propagation component in the out-of-plane direction is, however, not available experimentally, and while out-of-plane flow can be measured, the flame orientation is unknown in the out-of-plane direction such that its effect is unknown. However, when DNS is used the three-dimensional flow field and the flame propagation are simultaneously available for such an analysis.

Consider a infinitesimally small flame edge segment $ds(t)$ which is moving in the out-of-plane (spanwise, z) direction in a time δt to its new location $ds(t+\delta t)$. Over this period the point $P(t)$ intersecting the $x-y$ observation plane moves to location $P(t+\delta t)$ causing an apparent in-plane motion unless the flame edge happens to be oriented normal to the $x-y$ plane. (It also moves in the $x-y$ plane due to flow and propagation in that plane, but here we adopt a coordinate system that follows that motion in order to simplify the discussion.) Figure 3.8 shows a schematic of this concept. It is readily observed that the observed flow speed (or flame propagation speed) in the plane is obtained by projecting the z

component of the flow velocity (or relative flame propagation velocity) into the $\boldsymbol{T}_1$ direction, then projecting the result into the $x-y$ plane. We denote the apparent flow velocity by $(U_z)_x$, and the apparent flame propagation as $(V_{e,z)_x}$ (in the x-direction here). It is readily shown that these velocities are given by:

$$\begin{aligned}(U_z)_x &= -U_z \tan(\varphi)\cos(\psi), \\ (U_z)_y &= -U_z \tan(\varphi)\sin(\psi), \\ (V_{e,z})_x &= -V_{e,z} \tan(\varphi)\cos(\psi), \text{ and} \\ (V_{e,z})_y &= -V_{e,z} \tan(\varphi)\sin(\psi).\end{aligned} \tag{3.24}$$

3.7 Conclusion

In this chapter, the governing equations and their non-dimensional forms were presented. The details of the numerical schemes used in this study were also discussed. It was shown that the grid resolution was adequate to resolve both flame and turbulence. Finally, the concepts used for analysing the flame-turbulence interaction near the flame base was discussed.

Chapter 4

General structure of a turbulent lifted flame

4.1 Introduction

Capturing the complex physics in combustion phenomena is non-trivial even with the most modern laser imaging tools. Laser Induced Fluorescence (LIF) is one of the more common techniques to measure species concentration in turbulent reacting flows where the species concentration can be captured on a plane illuminated by a laser. However, this limits the observation to a two-dimensional plane. In addition to the two-dimensional limitations of the optical methods, variation of laser power and absorption of fluorescence are the other limiting factors. However, the third dimension is accessible when DNS is used. Therefore, the main objective of this chapter is to simulate a turbulent lifted flame using DNS apply the up-to-date post-processing approaches to investigate the instantaneous structure of the lifted flame, describe interesting features of the edge flames, and compare the observations against previous experimental studies.

4.2 Flame base structure

A volume rendering of logarithm of the scalar dissipation rate normalised by laminar flame time scale (blue/white) and reaction rate (red/orange) is presented in figure 4.1. Before reading further, the interested reader may consult an animation of vorticity magnitude (blue/white) and reaction rate (red/orange) which is presented in the online supplementary material to this thesis. This animation is quite instructive to gain an overall picture of the flame.

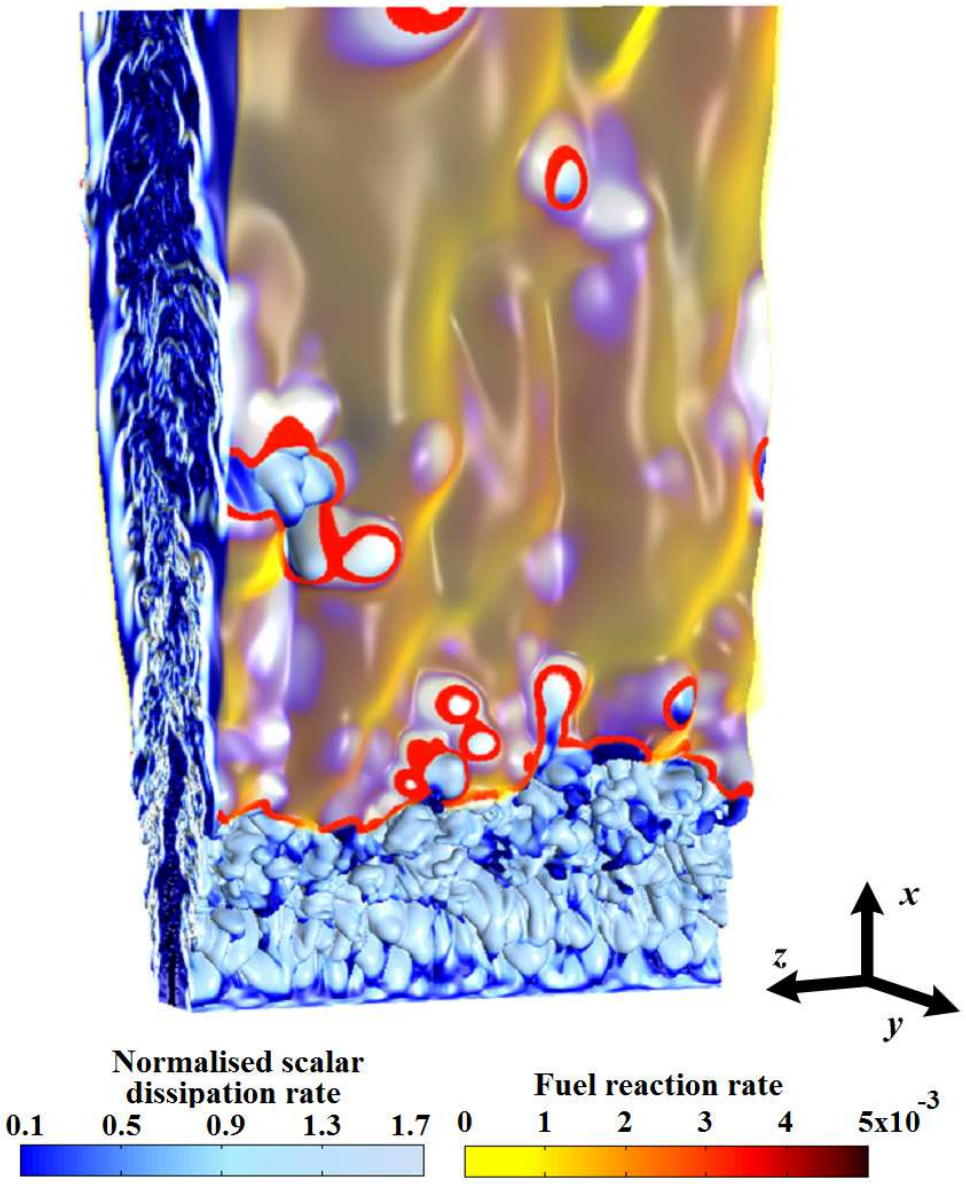

Fig. 4.1 Three-dimensional volume rendering of the logarithm of the scalar dissipation rate (blue/white) and reaction rate (red/orange). (Only the region $x/H < 14$ is shown.)

It may be observed in figure 4.1 that the flame has a complex structure which has features that are qualitatively similar to experimental observations of lifted flames [18, 19, 31, 89, 105, 109, 111, 113, 121]. Because the stoichiometric mixture fraction is small (0.055), the flame is found at the edge of the highly turbulent inner core of the jet. Heat release noticeably damps turbulence in the outer region.

Unlike the DNS of lifted hydrogen flames reported by Mizobuchi *et al.* [20, 21], no vigorous rich premixed flame core was observed. This difference is because hydrogen burns much more vigorously than hydrocarbons in rich mixtures. The mixture fraction dependence of the burning velocity is built into the present model by the mixture fraction dependent activation energy. Similarly, no diffusion flame islands on the lean side that were observed by Mizobuchi *et al.* [20, 21] were observed in this study. Once again this might have been a hydrogen-specific feature since much of the fuel was being consumed in the rich premixed branch.

To further elaborate this essential difference between hydrocarbon and hydrogen lifted flames, figure 4.2 shows an isosurface of product reaction rate coloured by the normalised flame index (NFI). It may be readily observed that the leading edges are premixed, followed by a trailing diffusion flame, which is mostly connected. Notably, there is not an extensive inner region of premixed flames, unlike in the case of hydrogen [20, 21]. Flame holes can be observed as the regions downstream of the leading edge, where high values of NFI indicate a locally premixed edge. (Other holes are observed without being surrounded by premixed edges, but these are still diffusion flames, which just have a lower reaction rate than the chosen threshold.) Returning to the discussion of figure 4.1, the leading flame edges at the base of the flame are highly convoluted. Consistent with many experimental observations of lifted flames [18, 19, 31, 89, 105, 109, 111, 113, 121], the leading edges do not typically exhibit a tribrachial structure. This lack of three distinct branches has been previously explained to result from mixture-fraction gradients ahead of the flame being too large to support distinct lean and rich branches [15]. Occasionally, when the flame is found in a low strain rate region, a short or weak rich premixed branch was observed, but a distinct lean branch was never observed.

The reaction rate is locally higher at the flame edges than further downstream, which is consistent with the existence of a premixed leading edge flame. It is also noted that in the present case, the premixed flame edges are quite narrow and of the order of the laminar flame thickness, which implies that the premixed edge flames are quite unlike a flat turbulent premixed flame with lateral dimensions much larger than the laminar flame thickness i.e. at

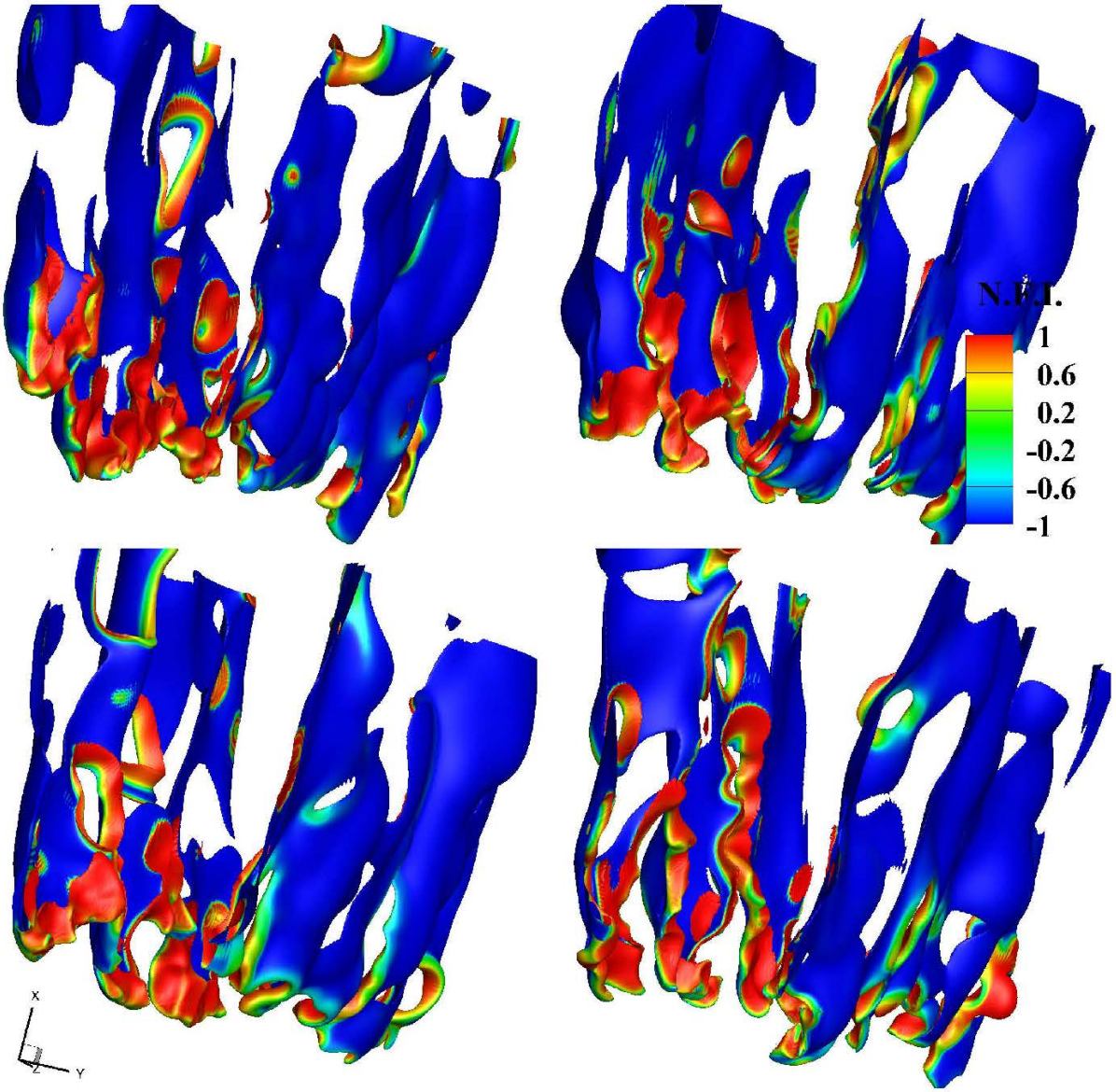

Fig. 4.2 The reaction rate iso-surface of fuel $|\dot{\omega}_F| = 0.001$ coloured by normalized flame index (NFI).

this lifted height, the premixed flame theory of stabilisation is ruled out[1], a fact which has already been noted by others e.g. see the discussion in [22].

There is a proliferation of flame holes, not observed in earlier DNS studies of lifted flames [20, 21, 42, 56]. In the case of Mizobuchi *et al.*[20, 21], conversely to this simulation, isolated burning islands in a mostly non-burning stoichiometric surface were observed rather than holes in a mostly connected burning surface. As will be presented in more detail shortly, these holes originate by two different mechanisms. Some of the holes are generated by flame propagation at the leading edge while others are caused by local flame extinction. Both kinds of holes can either grow or shrink and disappear as they go downstream. They can also merge with other holes and/or split into multiple holes. The existence of extinction holes suggests that in this flame (which has a relatively low lifted height), the critical scalar dissipation rate can be locally exceeded, which suggests that extinction can moderate the stabilisation process [8].

No unconnected regions of high reaction rate ahead of the leading edge were observed. All regions ahead of the leading edge are connected, even though in a two-dimensional (2D) streamwise-transverse plane they may appear as unconnected flame elements. (Although one still image cannot show this, the supplementary animations certainly do.) Neither transport of hot products or even large scale folding of the flame into upstream unburned regions was observed. The lack of any unconnected regions or large scale folding of the flame to upstream unburned regions therefore rules out, for the present flame, a stabilisation mechanism supported only by upstream turbulent transport. In an early theory Broadwell [34] proposed that lateral ejection of hot products and later re-entrainment into the jet could support stabilisation of the flame at a given location, but nonetheless it seems that some upstream transport mechanism would be needed in this theory to balance the oncoming flow once the flame is re-entrained into the high streamwise velocity region, and thus the present results seem to rule out this early theory.

The stabilisation mechanism is evidently far from being laminar in its overall structure. The large degree of convolution of the flame edge implies it can consume stoichiometric reactants at a much greater rate than in a laminar flame (which would present a single straight line here), similar to how increased surface area causes the turbulent burning velocity to be larger than the laminar one in premixed flames. (Note that similar to a turbulent premixed flame, the existence of locally laminar structures is however not ruled out.) Another way of thinking about this in a planar picture of the flame is that out-of-plane motion can lead to

[1] This is true in this interpretation at least which specifies that for a typical premixed flame to be supported it must be at least integral scaled in width.

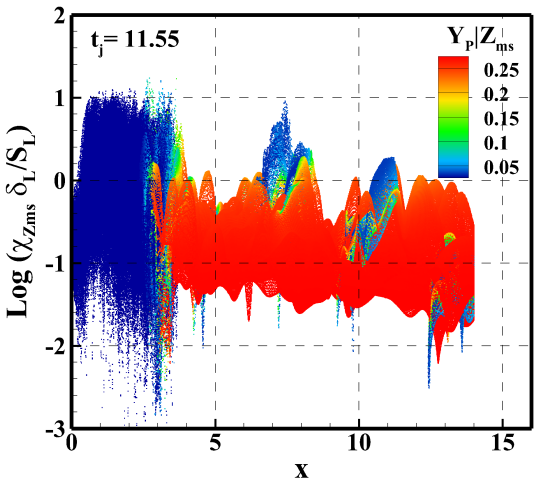

Fig. 4.3 Scatter plot of logarithm of the scalar dissipation rate conditioned on the mixture-fraction iso-surface $Z = 0.07$ versus the distance from the nozzle and coloured by the product mass fraction for $t_j = 11.55$.

additional upstream transport – i.e. that flames can propagate laterally around high velocity regions in large eddies eventually leading to additional upstream propagation. Later in this chapter and chapter 5, it will be shown that this mechanism is very significant in some regions of the flame.

It may be observed that the leading edge structure qualitatively seems to be convoluted on the scale of large eddies. The role of large eddies can also be qualitatively observed in the animation in the supplementary material. In chapter 5, evidence will be presented showing that large eddies definitely do play a role in the stabilisation.

4.2.1 Scalar dissipation and hole formation

As mentioned earlier, some of the observed holes in reaction sheet are consequence of local extinctions which occur when high scalar dissipation rate structures, with scalar dissipation rate comparable to quenching limit, occur near the mixture-fraction iso-surface. The scalar dissipation is a key parameter in many modelling frameworks and some stabilisation theories have been developed on the critical scalar dissipation concept [13, 24]. To assess this theory and the qualitative observations in figure 4.1, instantaneous scatter plots of conditional normalised scalar dissipation rate on the mixture-fraction iso-surface with the maximum laminar flame speed coloured by the product mass fraction at $t_j = 11.55$ are presented in figure 4.3. There are a couple of interesting features to be noted in this figure. Both scalar dissipation rate and its fluctuations are high upstream of the flame base. The highest scalar dissipation rate is more than $\log(\chi\delta_L/S_L) = 1$, and as expected it decays in

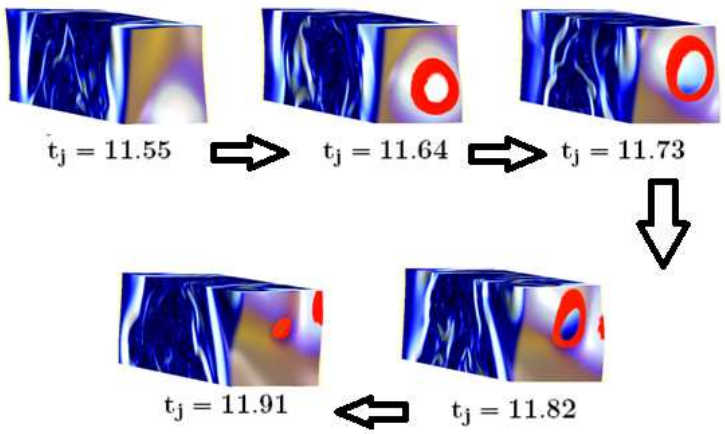

Fig. 4.4 Three-dimensional view of the creation and shrinking of an extinction hole. The same variables as in figure 4.1 are shown.

the streamwise direction. It is noticeably lower in the burning regions of the flame starting around $x \approx 3$ (as indicated by low product mass fractions) than in the upstream non-burning regions (as indicated by high product mass fractions). It may be noted that the highest dissipation rate regions correspond to the locations of holes (indicated by regions downstream of the lifted height but having a low product mass fraction). Some regions of lower dissipation rate are also noted in holes – these are probably in holes which are reigniting, but also may be holes which are formed by another mechanism which is discussed below. The structure of the observed holes are now identified and discussed in more detail using 3D visualisations. Figure 4.4 shows the same variables as figure 4.1 during the formation and reignition of an extinction hole. As shown in figure 4.4 the hole is formed in a region of high scalar dissipation rate which bulges out towards the oxidiser side, which appears to be connected with the passage of a large eddy. The hole is revealed to be significantly curved in the out-of-plane direction such that the high scalar dissipation region and thus extinction hole has approximately similar streamwise and spanwise extents. As the large eddy passes, the scalar dissipation rate relaxes and the hole reignites.

The formation of a different type of hole is examined in figure 4.5. It is observed that initially, there is a local downstream motion of the flame around a large eddy. This causes a horseshoe-like edge-flame structure to arise. In the subsequent frames the flame comes together in the upstream region, finally reconnecting to form a flame hole, which is termed here as an “inclusion hole". If observed in a two-dimensional $x-y$ plane, this would be seen as the appearance of an upstream island. The convergence of the flames on either side towards the reconnection point implies that flame propagation, and not simply out-of-plane

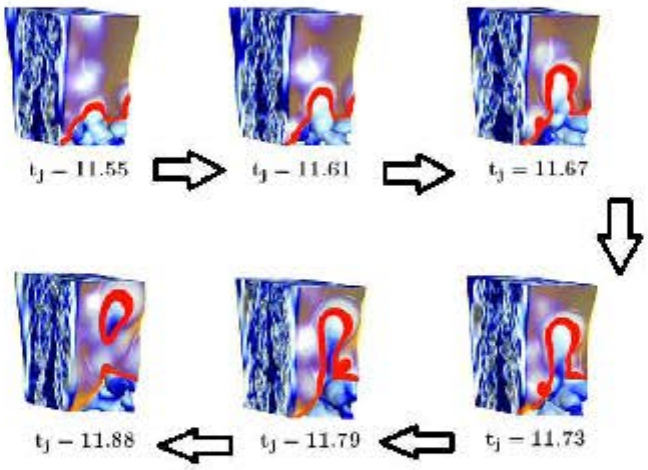

Fig. 4.5 Three dimensional time sequence of hole creation showing the same variables as figure 4.1

advection, must be involved in the appearance of the upstream island in this case. Thus, the present work demonstrates two distinct mechanisms of hole-formation and a connection of the appearance of some upstream islands (as observed in a plane) with the formation of an inclusion hole. Importantly, both of these mechanisms generate mixture-fraction conditional fluctuations of temperature and species, which may be important to represent from a modelling perspective. In planar experimental measurements it is impossible to definitely determine which mechanism causes the observed holes, because holes can be created by out-of-plane motion of reacting regions into the plane or of out-of-plane motion of non-reacting regions into the plane. However, a very recent study by Boxx *et al.* [38] used a combination of OH PLIF and line-of-sight OH* chemiluminescence to suggest that there can be very significant out-of-plane flame edge wrinkling such that apparently observed in-plane holes are actually not holes but are connected main leading edge flames which is consistent with the observations in this DNS.

Future work is planned to quantify the relative importance of these two types of holes, as well as to understand their time evolutions and geometries.

4.2.2 Time evolution of the flame base

A time series of the most-upstream flame-edge location is presented in figure 4.6 at the $z = 0$ plane. The flame edge was identified as the intersection of mixture-fraction and product mass fraction iso-surfaces as discussed in section 3.6.3, and when more than one such location appeared in a plane, the most upstream was selected. The mean stabilisation point is $3.2H$ in the streamwise direction. Fluctuations of the order of the jet width can occur

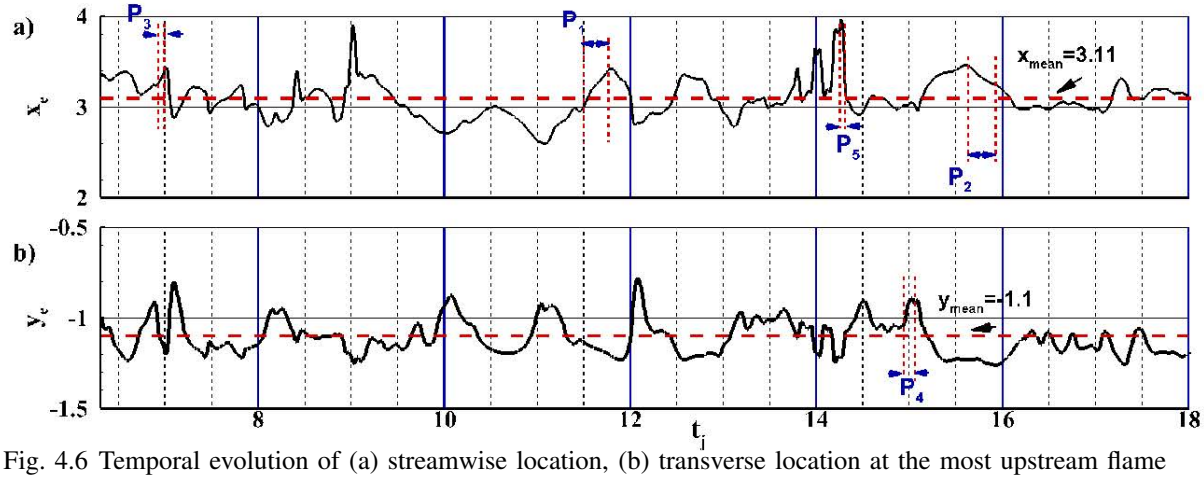

Fig. 4.6 Temporal evolution of (a) streamwise location, (b) transverse location at the most upstream flame edge on the plane $z = 0.0$.

in the streamwise direction. The mean transverse location is -1.2H. The maximum level of fluctuations is less than 0.5H in the transverse direction. Several different events involving upstream and downstream motion are noted in figure 4.6. At times there is smooth downstream (P_1, P_3) and upstream (P_2) motion, but also at times there are sudden jumps in lifted height (P_5). According to the literature, the upstream jumps are expected to be related to out-of-plane motion [8, 17–19] or conceivably to the appearance of isolated islands [20, 21, 34]. Sudden downstream motions of the flame base are also observed. The flame motion scenarios marked in figure 4.6 are now discussed in more detail.

Figure 4.7 presents, for the time period P_1: (a) contours of the reaction rate and vorticity magnitude, (b) contours of the logarithm of the normalised scalar dissipation rate and (c) the streamwise and transverse vector components of apparent flow and edge-flame propagation velocities at the flame-base location. The black solid line represents the product mass fraction of 0.2 and the dashed line corresponds to the mixture fraction of 0.07, which has the maximum laminar flame speed. (Recall that the intersection of these iso-surfaces define the “flame-edge" – it may be noted that they do indeed provide a good marker in the forthcoming figures.) The two red solid lines in figure 4.7(a) indicate the flammability limits. The lower and upper flammability limits of methane are ϕ =0.46 and 1.64, respectively [122]. These limits approximately correspond to the laminar flame speed being less than about 5% of the maximum laminar flame speed. The time sequences are presented from left to right. The fuel and oxidiser are on the right and left right hand sides, respectively. As can be seen, at times t_j =11.49 and 11.55, large eddies squeeze the flammable region (figure 4.7(a), marked as A_{P1}). This results in a comet-shape flame front as marked by B_{P1} in figure 4.7(a). As shown in figure 4.7(b), the scalar dissipation rate is also high at the flame

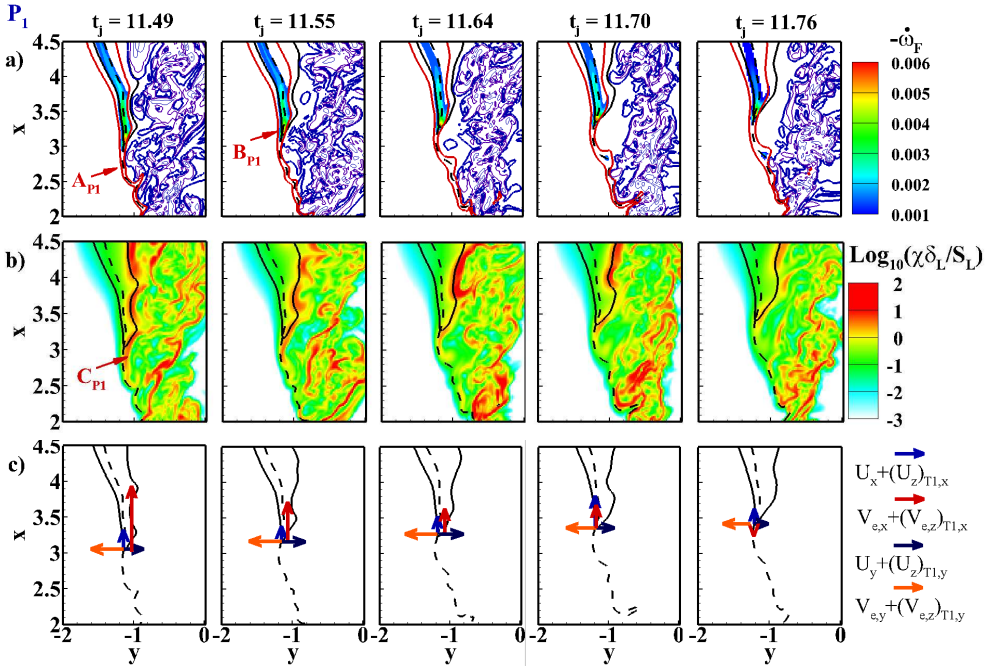

Fig. 4.7 Time evolution of the flame base in the plane $z = 0.0$ during the time period P_1 exhibiting smooth downstream motion when the apparent streamwise velocity and streamwise component of edge velocity are positive, showing: (a) reaction rate on a colour scale, vorticity contours in blue, and red solid lines marking the flammability limits (laminar flame speed less than 5% of maximum 1D laminar flame speed) (b) the logarithm of the scalar dissipation rate (c) the apparent flow and propagation velocity vector components. In all figures above the black solid line marks the product mass fraction of 0.2 while the dashed line is the mixture fraction of 0.07.

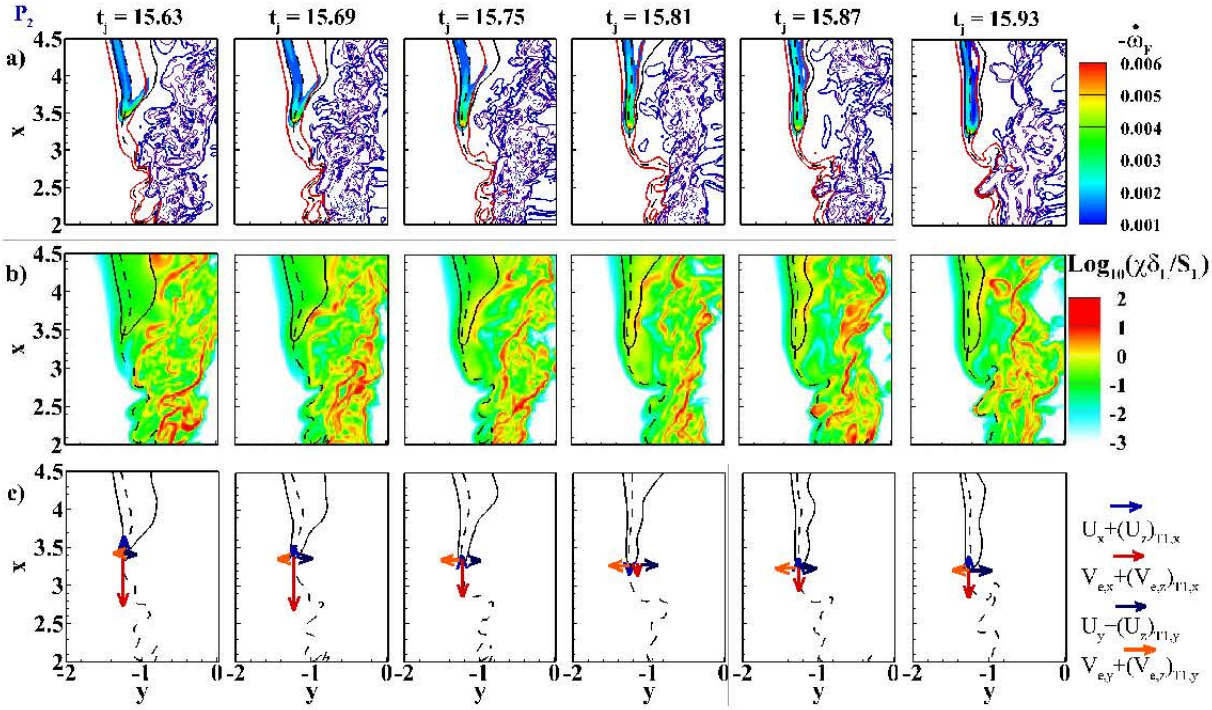

Fig. 4.8 Time evolution of the flame base on the plane $z = 0.0$ for a case involving a smooth upstream propagation during period P_2, showing: (a) reaction rate on the colour scale, vorticity contours in blue, and with the red solid lines marking the flammability limits, (b) the logarithm of the scalar dissipation rate and (c) the apparent flow and propagation velocity vector components. In all figures above the black solid line marks the product mass fraction of 0.2 while the dashed line is the mixture fraction of 0.07.

base (marked as C_{P1}). In this case, the dissipation rate is high enough to cause a positive apparent propagation velocity, i.e. a negative relative flame speed noting that the flame normal is pointing towards the negative streamwise direction. In the next two time sequences, t_j =11.64 and 11.70, there is no large structure in vicinity of the flame base and the scalar dissipation begins to relax, leading to less negative relative flame speeds by t_j =11.76 the flame speed becomes positive again and approximately balances the flow (figure 4.7(c)).

Figure 4.7(c) also presents the apparent transverse propagation and flow velocities by orange and dark blue horizontal vectors, respectively. It shows that the flame propagates relative to the flow towards the region of leaner mixtures and is dominant over the entrainment flow directing the flame towards the region of richer mixtures. During time period P_2, a case of upstream propagation is presented in figure 4.8. Once again, the same parameters as in figure 4.7 are shown. As shown in figure 4.8(a), at time $t_j = 15.63$, the flammable region is wide, about twice as wide the laminar flame thickness. There are no large eddies containing vortical fluid around the flame base to disturb the propagation process. The absence of such structures also allows the existence of a rich premixed wing. The scalar dissipation

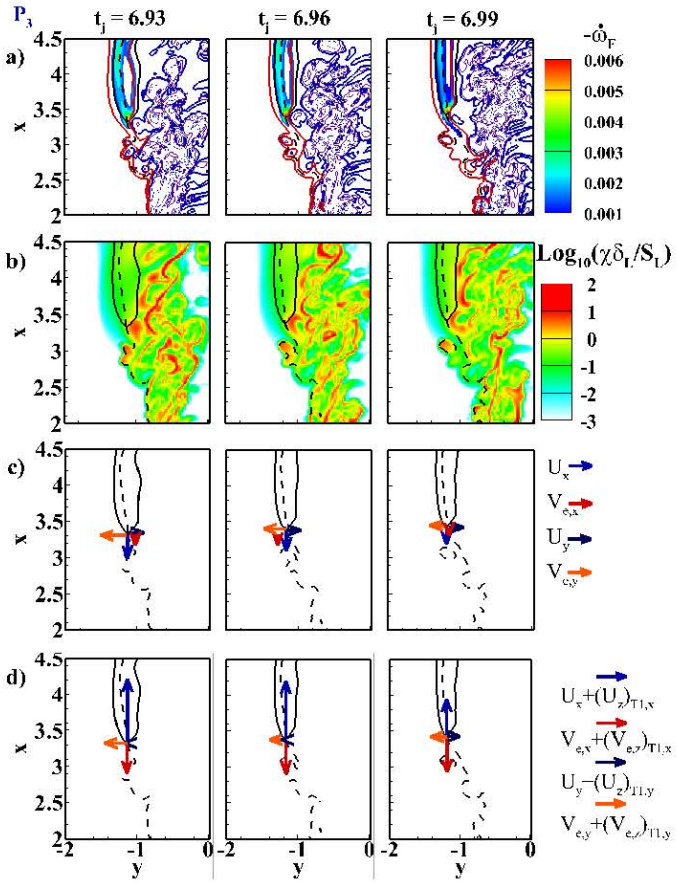

Fig. 4.9 Time evolution of the flame base at the plane $z = 0.0$ for a case of smooth downstream motion during time period P_3 when the apparent streamwise velocity and streamwise component of the edge velocity are negative, showing: (a) the reaction rate on a colour scale, contours of vorticity magnitude in blue, and with the red solid lines marking the flammability limits, (b) the logarithm of the scalar dissipation rate, (c) the streamwise and transverse flow and edge propagation velocity vector components, and (d) the apparent flow and propagation velocity vector components. In all figures above the black solid line marks the product mass fraction of 0.2 while the dashed line is the mixture fraction of 0.07.

rate is low in a large region upstream of the flame base. All these conditions sought by the flame to propagate, and as a result the upstream propagation speed of the flame is strong as shown in figure 4.8(c). Owing to the subsequent passage of a large eddy, the thickness of the flammable region decreases and scalar dissipation rate increases, which leads to the upstream propagation speed decreasing. At around $t_j = 15.87$, the dissipation rate relaxes and the upstream flame propagation speed increases again. The time period P_3 shown in figure 4.6 is considered now. Figure 4.9(a) and (b) present the same variables previously shown in figure 4.7(a) and (b). Figure 4.9(c) shows the in-plane flow and edge-flame propagation velocities and figure 4.9(d) shows the apparent flow and flame propagation velocities with the out-of-plane component included. In contrast to the previous downstream motion shown

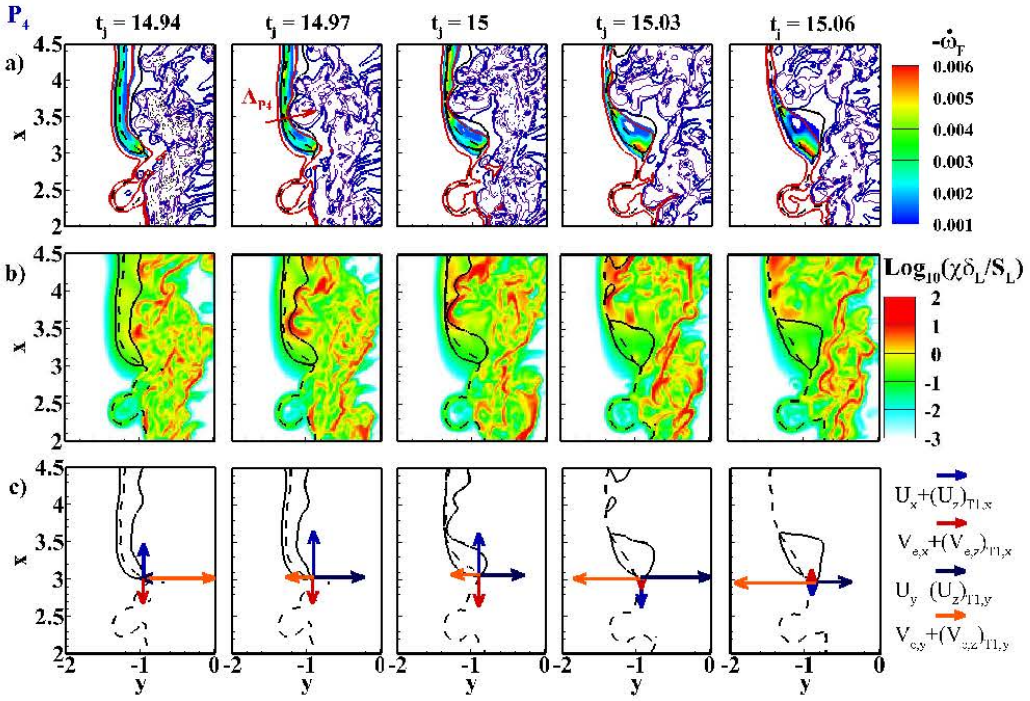

Fig. 4.10 Temporal snapshots during the event P_4 showing involving the appearance of a hook-shape, showing: (a) contours of reaction rate on a colour scale with vorticity contours in blue; (b) contours of the logarithm of scalar dissipation; and (c) flow and flame propagation velocity vector components. In all figures above the black solid line marks the product mass fraction of 0.2 while the dashed line is the mixture fraction of 0.07.

in figure 4.7, this case features a much wider flammable region (with a weak rich premixed branch being evident), a lower scalar dissipation rate, and as a result the flame speed is positive, which according to the in-plane picture would lead to an upstream propagation, since the flow velocity is also in the upstream direction. However, when the out-of-plane components are added in, the picture is rather different. While the upstream flame propagation is stronger including the out-of-plane propagation, including the z-component of the flow velocity results in an even larger downstream apparent velocity, thus demonstrating that out-of-plane motion definitely needs to be considered in the overall picture.

Before moving on, it is remarked that nearly every other combination of different components (flow/flame and in-plane/out-of-plane) being dominant also were observed. The above cases were selected only to provide some examples, and should not be interpreted as the statistically most significant situations. The statistically averaged picture is discussed in chapter 5. Figure 4.10 shows an example which involves a large transverse velocity resulting the creation of a hook structure (time period P_4 in figure 4.6). The variables shown are once again the same as in figure 4.7. At $t_j = 14.94$, the flame initially has a fairly unconvoluted structure which is propagating towards the fuel side. At the second time instant

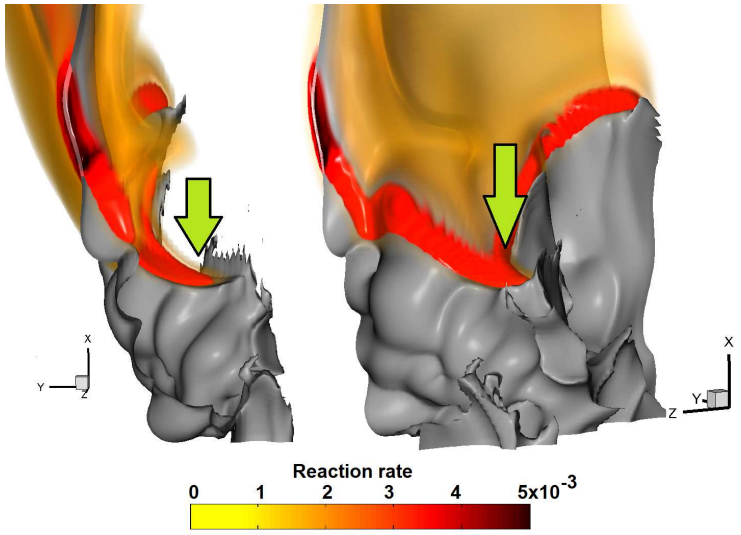

Fig. 4.11 Three-dimensional view of a hook shape structure(the red/orange is reaction rate and the the grey surface is Z_{st} surface.

shown, a large turbulent eddy bulges out towards the oxidiser side, which may be observed at the point marked "A_{P4}", where the high vorticity region impinges onto the flame from the oxidiser side. At the same time, a large entrainment flow is occurring at the base. The coupling of the bulging turbulent eddy and the entraining flow cause an anti-clockwise rotation of the flame and distort it into a "hook" structure. Such hook structures have been observed frequently in experimental measurements of lifted flames (for instance, figure 7 in Ref. [108], figure 3a in Ref. [109], figure 3f and 4a in Ref. [31], figure 4 in Ref. [123], figure 5 in Ref. [19], figure 4 in Ref. [18] and figure 3 in Ref. [17]) and are confirmed by the present DNS. This structure is also examined in 3D (figure 4.11) and shows to have a complex shape with significant curvatures in the out-of-plane direction - i.e. it is not a simple 2D structure. The role played by large eddies in the creation of these structures supports the schematic of Kelman *et al.* [108] (figure 4.12), and it is consistent with experimental measurements by Upatnieks *et al.* [9, 123] and Boxx *et al.*[18, 19]. In the example shown in figure 4.10, the large eddy is even strong enough to cause an extinction hole above the leading edge location.

4.2.3 Out-of-plane motion

The appearance of flame islands upstream of the main flame has been observed in many experimental studies of lifted flames [8, 17–19, 38, 123]. The laser-based diagnostic techniques used in these studies rely on the measurements in two-dimensional sheets. An example of the upstream island observed in experimental results by Boxx *et al.* [19] is presented in figure 4.13. To analyse the effect of the out-of-plane motion on flame stabilisation, access

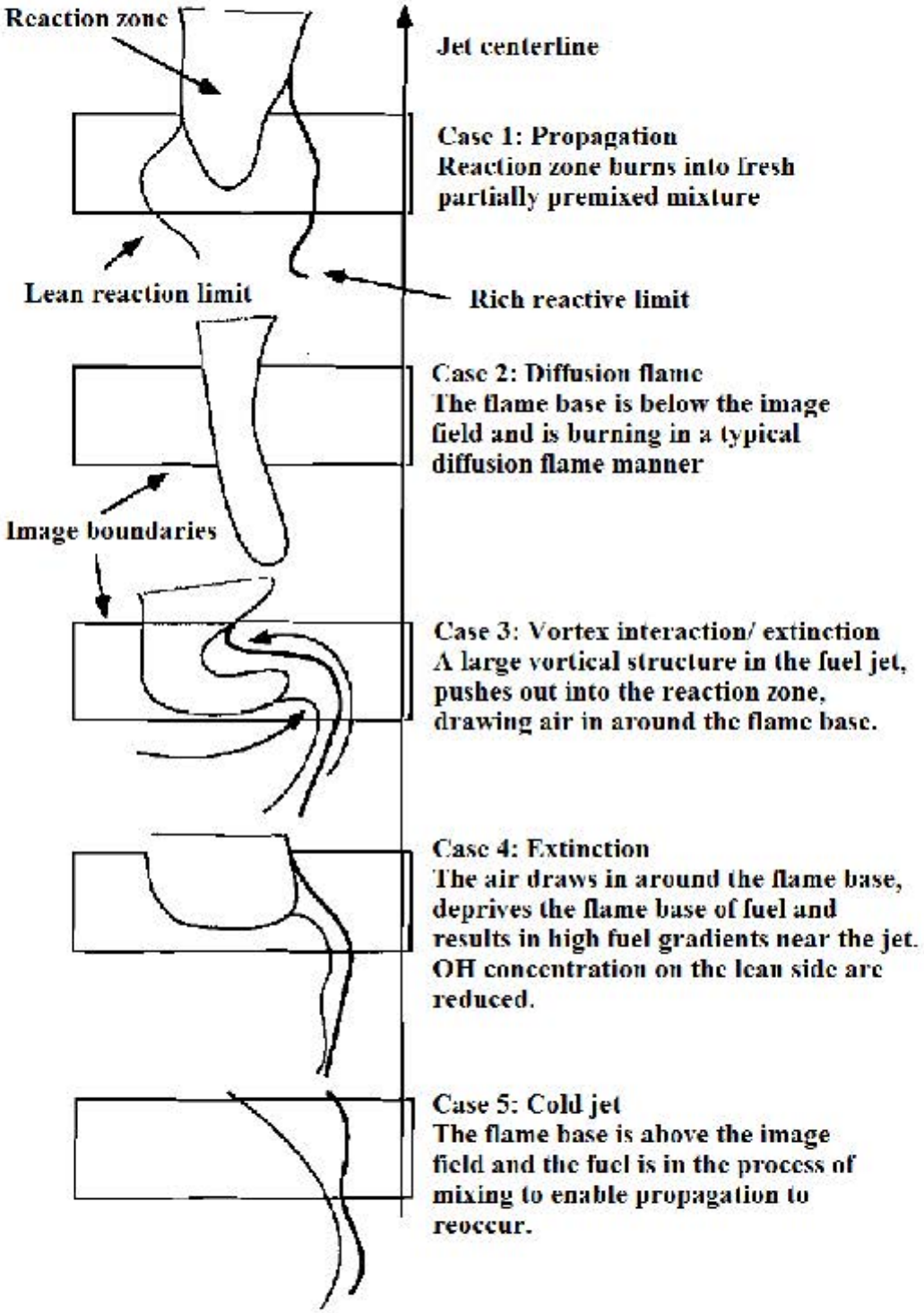

Fig. 4.12 Schematic of the creation of hook structure [108].

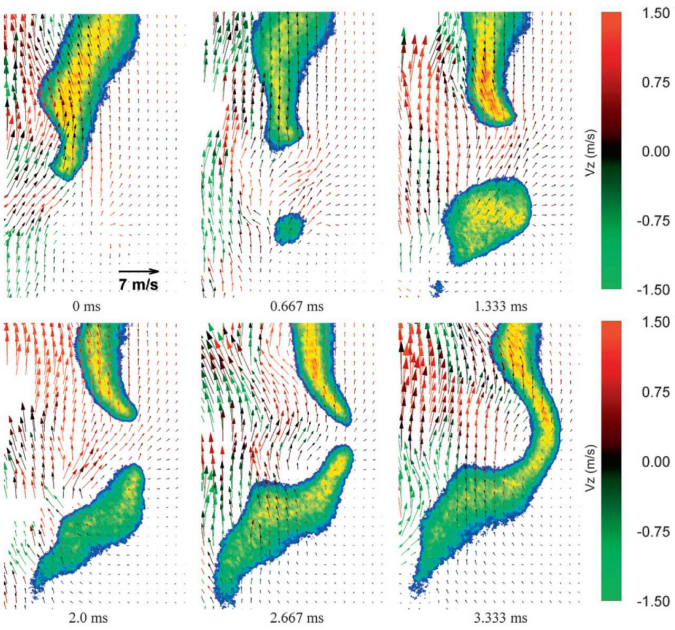

Fig. 4.13 OH-PLIF/PIV measurement sequence highlighting the formation, distortion and merging of a flame island [19].

to both the out-of-plane flow and flame propagation velocities is necessary, which has not yet been demonstrated experimentally. DNS however provides the full three-dimensional data which allows for a detailed examination of the out-of-plane flame motion. In this section, an example for appearance of a flame island near the flame base is presented. The effects of flow and flame propagation are also investigated. Figure 4.14 shows the contour plots of the out-of-plane (spanwise) flow velocity. At t_j =14.13, a small island appears in a region where the out-of-plane velocity is positive. This island (marked as A_{P5}) grows rapidly as can be seen in the next time, t_j =14.28 and 14.31. At t_j =14.34, the island disappears. The appearance of islands in the observation plane has been reported in many experimental studies of the lifted flame ([8, 17–19, 38, 123]); however, the inaccessible third dimension in the experiments has limited investigations of the physical reasons for the observed islands. It has been suggested that islands can results from either propagation or convective motion of the flame edge from the negative z direction. To examine this hypothesis, the $x-z$ plane view of the flame base is presented in figure 4.15. Shown here, the flame base is a continuous structure and there is no disconnected pocket of product or reaction zone upstream of the flame base. Instead, the island is observed in the $x-y$ plane due to contortion and motion of the edge. (We also reiterate at this point that we never observed any disconnected upstream islands in the 3D animations of this case.) In figure 4.15, the flame base is also coloured by (a) spanwise velocity and (b) spanwise edge base propagation. At t_j =14.13

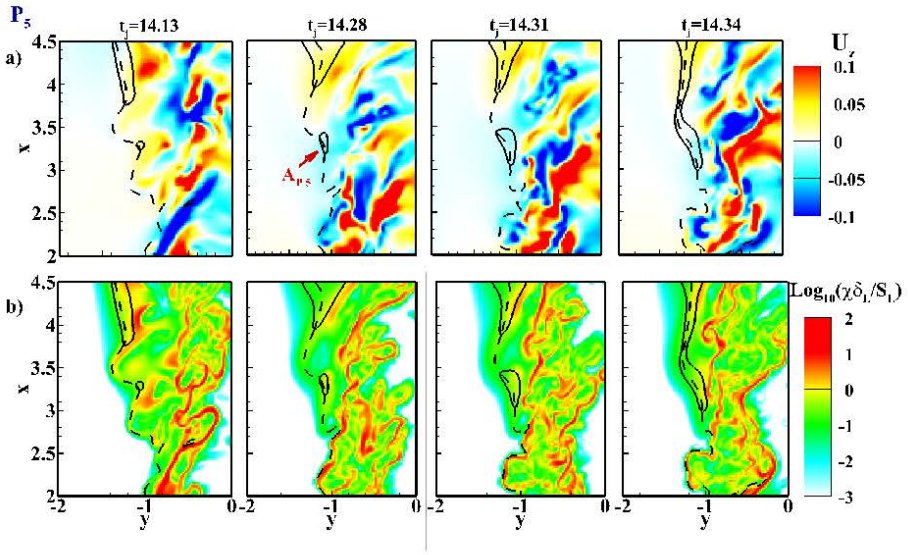

Fig. 4.14 Time evolution of the flame base at plane $z = 0.0$ for sudden upstream jump in lifted height: (a) out-of-plane flow velocity and (b) scalar dissipation rate (the black solid line in all figures is product mass fraction of 0.2 and the dashed line is the mixture fraction of 0.07).

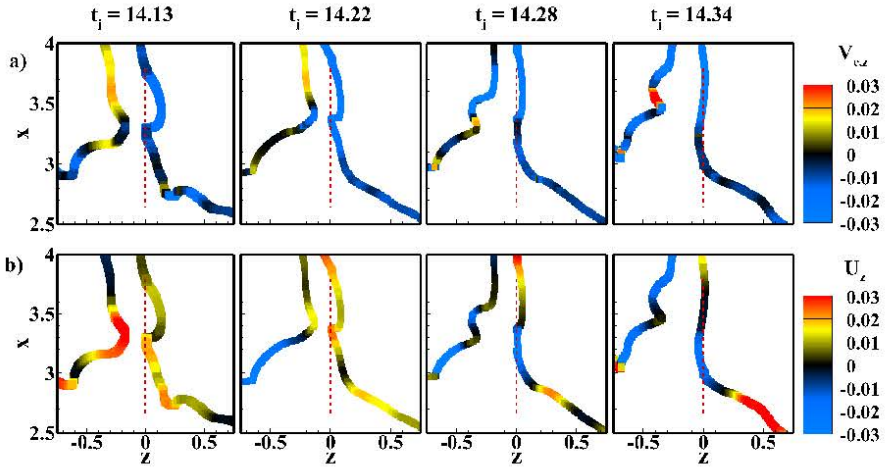

Fig. 4.15 The $x-z$ plane view of the out-of-plane motion of the flame base corresponding to appearance of an island in figure with flame base coloured by (a) spanwise and (b) edge-flame velocity.

while the out-of-plane velocity is positive, the out-of-plane propagation exceeds the flow and is in the opposite direction, leading to the flame island actually appearing from the opposite side as suggested by the flow alone. Eventually, the out-of-plane flow reverses and both components promote the growth of the island in the $x-y$ plane. We also observed cases of the opposite scenario, and cases when the flow and flame velocities were aligned and not aligned. But overall, the results certainly suggest that flame propagation in the out-of-plane direction cannot be ignored. Planned future work will quantify in an averaged sense the role of out-of-plane flow and flame propagation on the appearance of upstream islands, as well as to quantify other out-of-plane effects in an effort to better understand the existing, very substantial, body of experimental work based on in-plane measurements.

4.3 Conclusions

In summery, the structure of the leading edge of the flame was first examined and related to previous two-dimensional experimental observations of lifted flames. The edge-flames were found to be composed of a single branch centred close to the stoichiometric contour – lean and rich premixed branches were not observed. Hook-like structures, similar to those observed experimentally, were noted. These were not parts of a triple flame branch but were distorted flame elements that occurred when turbulent eddies pushed the flame outwards downstream of the leading edge and entrainment flow upstream of the edge caused rotation. No instances of unconnected flame elements either upstream or as diffusion flame islands in lean regions were observed. Two types of flame holes were found to occur. The first was termed as an extinction hole and this resulted from large eddies which caused the flow to bulge out towards the oxidiser, creating a high scalar dissipation region and leading to local extinction. The second was termed as an inclusion hole and it was found when there was a local downstream motion of the flame and subsequent transverse flame propagation and flow motion at an upstream location which reconnected the flame there, leading to a hole downstream.

Chapter 5

Stabilisation mechanism of a turbulent lifted flame

5.1 Introduction

As briefly outlined in chapter 3 and more comprehensively in the review articles by Pitts [7], Lyons [8] and Lawn [22], the stabilisation mechanism has still not been determined. It has been widely reported that flame propagation plays a key role; however, there has been no complete experimental measurement of edge flame velocities, principally because the out-of-plane flame propagation is unknown. A few experimental studies have reported relative flame propagation velocities [9, 11, 17, 118, 124]. In all these studies, the flow velocity is measured using PIV. The absolute edge-flame velocity is accessible by comparing flame base location in two sequential measurement of the flame base. To mark the flame location, some experiments used the evaporation of liquid PIV seeding particles [11] which involved a large uncertainty, while others used PLIF of a radical species, such as OH or CH [9, 17, 118, 124]. While uncertainties associated with measuring the flame location by applying the latter method are reduced, there are other systematic errors that should be considered. The main challenge is a lack of knowledge of the out-of-plane velocities or any knowledge of flame structure in the third dimension. To partly address this challenge Gordon *et al.* [17] conditioned their results on low out-of-plane velocities, but this still does not capture out-of-plane flame propagation. This is the principal gap that will be addressed in this chapter. The presented DNS data provides both the flow and propagation velocities in three dimensions, which eliminates the uncertainties embedded in the above experimental studies.

Therefore, the first objective of this chapter is to quantify the motion of the flame base

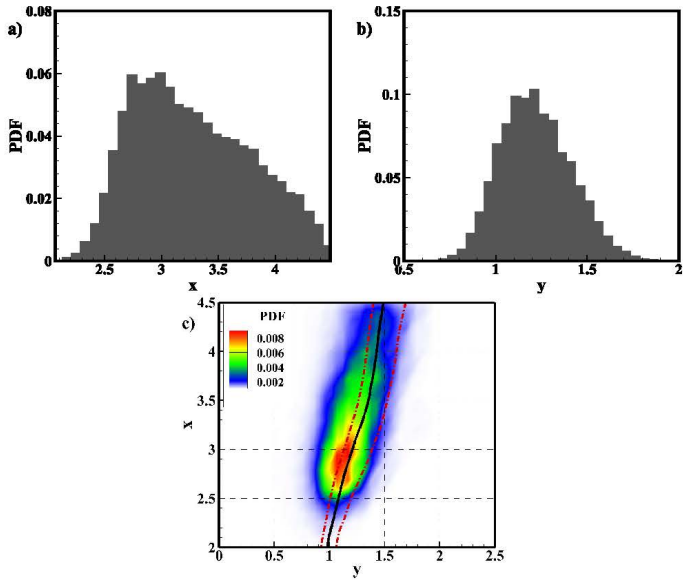

Fig. 5.1 Locations of the flame, showing: (a) PDF of the streamwise location of the instantaneous edge-flame locations; (b) PDF of the transverse location of instantaneous edge-flame locations; and (c) joint PDF of the streamwise and transverse locations. In the above, the solid line is the temporal and spatial Favre averaged mixture fraction equal to 0.07 and the dashed lines are temporal and spatial Favre averaged mixture fraction corresponding to flammability limits .

in an instantaneous and local manner, in order to reveal the roles played by flame propagation and turbulent eddies, and thus propose the flame stabilisation mechanism. The second objective is to analyse the flame base from an averaged standpoint to provide additional support for the proposed mechanism.

5.2 Statistics of the flame base

5.2.1 Flame base location

This section now seeks to address quantitatively the dynamics of the flame base region (conditional on $x/H < 4.5$) and the turbulent flow/flame-edge interaction by studying the flow and flame velocities conditional on the instantaneous edge-flame locations. Figure 5.1(a) and (b) present the PDF of the streamwise and transverse locations of the instantaneous edge-flame locations, whereas figure 5.1(c) shows the joint PDF of the streamwise and transverse location of the edge-flame. The solid black line in figure 5.1(c) is the temporally and spatially Favre-averaged mixture fraction equal to 0.07 (which as explained earlier has the maximum laminar flame speed). The time-averaged location of the flame base is $3.2H$ and $1.2H$ in streamwise and transverse directions, respectively. The PDFs of the streamwise

and transverse location of the flame base (figure 5.1(a) and (b)) show a wide distribution around the time-averaged values which is caused by the turbulence-flame interaction at the leading edge. Figure 5.1(c) shows that the flame base moves on the periphery of the jet with a higher probability of being located close to the averaged mixture fraction corresponding to the maximum laminar flame speed, Z_{ms} =0.07. The same observation was reported in previous experimental studies [1, 11, 23, 33, 113, 116, 123].

The joint PDF of the flame base location represents a similar shape to the scatter plots of the flame base location presented by the experimental lifted slot-jet flames presented in Ref. [38], even though the present conditions are somewhat different, having a much lower co-flow velocity and a lower density ratio between the fuel and oxidiser jets.

5.2.2 Flow and propagation velocities at the flame base location

The velocity statistics are now examined. Figure 5.2 shows: in the first row from left to right, the PDF of the streamwise, transverse and spanwise velocities conditioned on the instantaneous edge-flame locations; in the second row from left to right the joint PDF of the streamwise, transverse and spanwise velocities conditioned on the streamwise location of the flame base; and in the third row the joint PDF of the streamwise, transverse and spanwise velocities conditioned on the transverse location of the flame base. The parameter r noted in the figures (and subsequent ones) is the correlation coefficient between the two plotted variables. All velocities are normalised by the laminar flame speed of a flat premixed flame.

We first discuss the PDFs considering the ensemble over all flame-edge locations having $x < 4.5$, shown in figures 5.2(a)-(c). The streamwise flow velocity has a mean of $2.5S_L$ with fluctuations from -$12S_L$ to $20S_L$. Before discussing some comparisons of the present results to experimental observations, it is important to caveat these comparisons in that the locations at which we observe the velocities are within the inner reaction layer of the flame (since this is where a flame displacement speed can be sensibly evaluated) while the experimental measurements are often taken at a location where very small, low boiling point droplets evaporate (for example Su *et al.* [1] seeded co-flow with glycerol/water fog droplets and Yuen and Gülder [125] used submicron oil as seeding particles), which is likely to be slightly further upstream. Alternatively, where a flame marker based on OH or CH PLIF has been employed, the velocity measurements are deliberately off-set towards the upstream locations [9, 11, 17, 123]. Proceeding with this caveat in mind, experimental observations of a CH_4 lifted flame by Muniz and Mungal [16] shows that the mean streamwise flow velocity conditioned on flame base locations for different flow conditions ranges from 2.1 to $2.4S_L$,

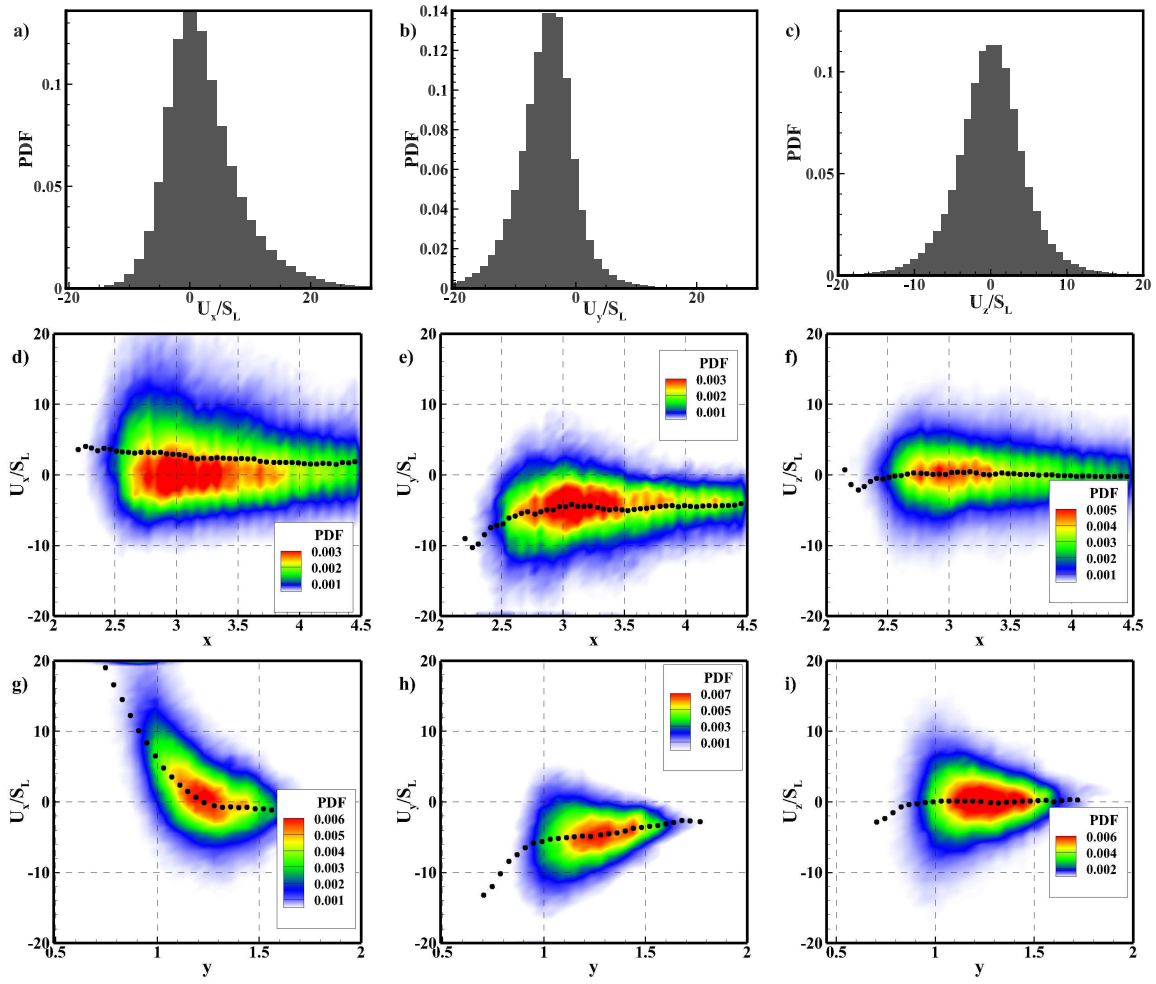

Fig. 5.2 Flow velocities conditioned on instantaneous flame-edge locations, showing: (a,b,c) the PDFs of different components; (d,e,f) joint PDFs of flow velocity components and streamwise location of the edge-flame locations, and the mean velocities conditional on streamwise location; and (g,h,i) joint PDFs of flow velocity components and transverse locations and velocity means conditional on the transverse location.

which is close to our observation for the mean velocity. Similarly low mean streamwise velocity conditioned on flame base locations was also reported in other experimental studies of CH_4 lifted flames [1, 9, 11, 123].

The most probable streamwise velocity is very close to zero, but the PDF is positively skewed, thus resulting in a positive mean velocity. These observations are very consistent with experimental observations at low lifted heights discussed in Ref. [1]. Interestingly, there is a significant probability, 34%, of observing negative streamwise velocity, suggesting a local deceleration, an observation also noted in Ref. [1, 9, 123].

Now turning to the transverse velocity, it is noted that the mean of the transverse velocity is -5S_L with just 10% possibility of being positive. The statistics of the transverse velocity therefore demonstrate a strong role of the entrainment at this lifted height. Experimental measurements of radial velocities support a role for entrainment in lifted flames [105]. The PDF is also slightly negatively skewed.

Finally, the spanwise velocity has a nearly Gaussian distribution with zero mean as expected in a homogeneous direction.

Moving on to the statistics conditioned on streamwise distance shown in figures 5.2(d)-(f). It is observed that the conditional mean of streamwise velocity is positive and of the order of a few S_L and weakly decays with downstream distance. Fluctuations are significant and decay more significantly than the mean with downstream distance. The entrainment flow in the transverse direction generally decays with downstream distance, as expected, and its fluctuations also decay strongly. While the mean spanwise velocity remains zero its fluctuations are large at lower streamwise stations, suggesting it can still play a role in the stabilisation mechanism.

Considering the dependence of the velocities on transverse distance in figures 5.2(g)-(i), the picture becomes more complicated. The flame-edge conditioned streamwise velocity is very high towards the centre of the jet, greatly exceeding S_L, suggesting the flame must move downstream in that region. However, observing the trend for the transverse velocity, a confusing feature is observed – there is an overall positive correlation of transverse velocity with transverse position such that the highest negative streamwise velocities tend occur on average when y is smallest. As such, it is unclear from this picture how the flame can escape from regions of low y where, on average, streamwise velocities then would push the flame downstream, and transverse velocities push it further inwards.

The effect of flame propagation is now folded in. Figure 5.3(a)-(c) show the PDF of the absolute velocities (flow plus relative propagation) in the streamwise, transverse and spanwise directions, respectively. Considering first the streamwise component in figure 5.3(a), it

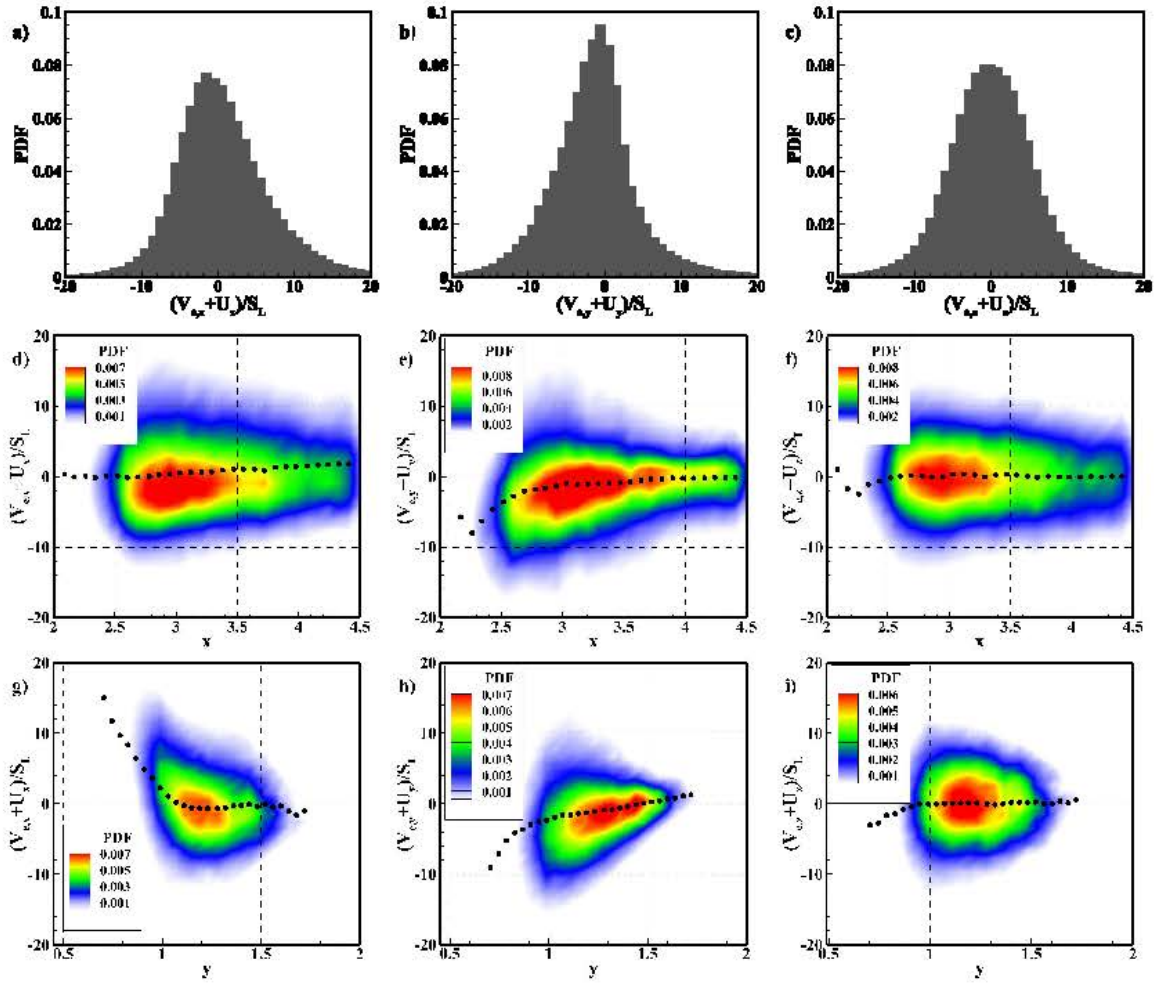

Fig. 5.3 Absolute flame velocity components conditioned on the edge-flame locations (including both flow and flame propagation velocities), showing: (a,b,c) PDFs of the components; (d,e,f) contour plots of the joint PDFs of the net velocity components and streamwise location of the flame edge and the streamwise conditional mean net velocities; and (g,h,i) the joint PDFs of the net velocity components and transverse location and corresponding conditional means.

is noted that compared with the previous PDF of the flow velocity in figure 5.2(a), the mean is now nearly zero, owing to reduced probabilities of high positive velocities (downstream motion) and increased probabilities of negative velocities (upstream motion). (The positive skewness is also visibly reduced.) Compared with the PDF of the transverse flow velocity in figure 5.2(b), the net transverse velocity shown in 5.3(b) is shifted towards positive values such that the mean and most-likely values are close to zero. The spanwise net velocity component is unremarkably different from that of the flow velocity, except that it exhibits similar fluctuation levels relative to the other velocity components.

Now turn to the means and PDFs conditional on streamwise distance shown in figure 5.3(d)-(f). Before discussing the more interesting streamwise and transverse components, it is noted that the spanwise net velocity component is not remarkable other than by having fluctuations that are significant relative to the other components, similar to the situation with the flow velocity only.

Here figure 5.3(d) shows that the streamwise flow velocity on average balances the streamwise upstream flame propagation in the most probable regions of flame stabilisation. This demonstrates that the flame is stabilised by edge-flame propagation, which is a major result of the paper. It may be noted that there is some lack of balance in the downstream regions starting from about $x \approx 3.5$. This is probably connected with flame holes which are move further downstream before they are annihilated. Another point to be noted in figure 5.3(d) is that the net velocity fluctuations are somewhat smaller than the flow velocity fluctuations in figure 5.2(d), suggesting that the flame speed tends to be negatively correlated with the flow speed.

Moving on to the transverse net velocity conditional on streamwise distance shown in figure 5.3(d), it is noted that while the conditional mean of the flow plus flame propagation velocity is smaller than it was for the flow velocity alone, it still does not balance in the upstream region, where on average the flame is entrained into the jet core.

Similarly, while the streamwise net velocity conditioned on transverse distance shown in figure 5.3(g) has a greatly reduced conditional mean, which is close to zero at larger y values, it is still positive towards the core of the jet. Finally, the transverse net velocity conditioned on transverse distance shown in figure 5.3(h) still cannot explain how on average the flame-edges escape from the inner core of the jet, since the average velocity is negative there. Interestingly, the average propagation velocity is also now somewhat positive for large y locations, suggesting outwards on-average movement at large y, which seems paradoxical.

To explain these apparently counter-intuitive results, now the two-dimensional picture is presented. To better understand the dynamic motion of the flame base, the flame base ve-

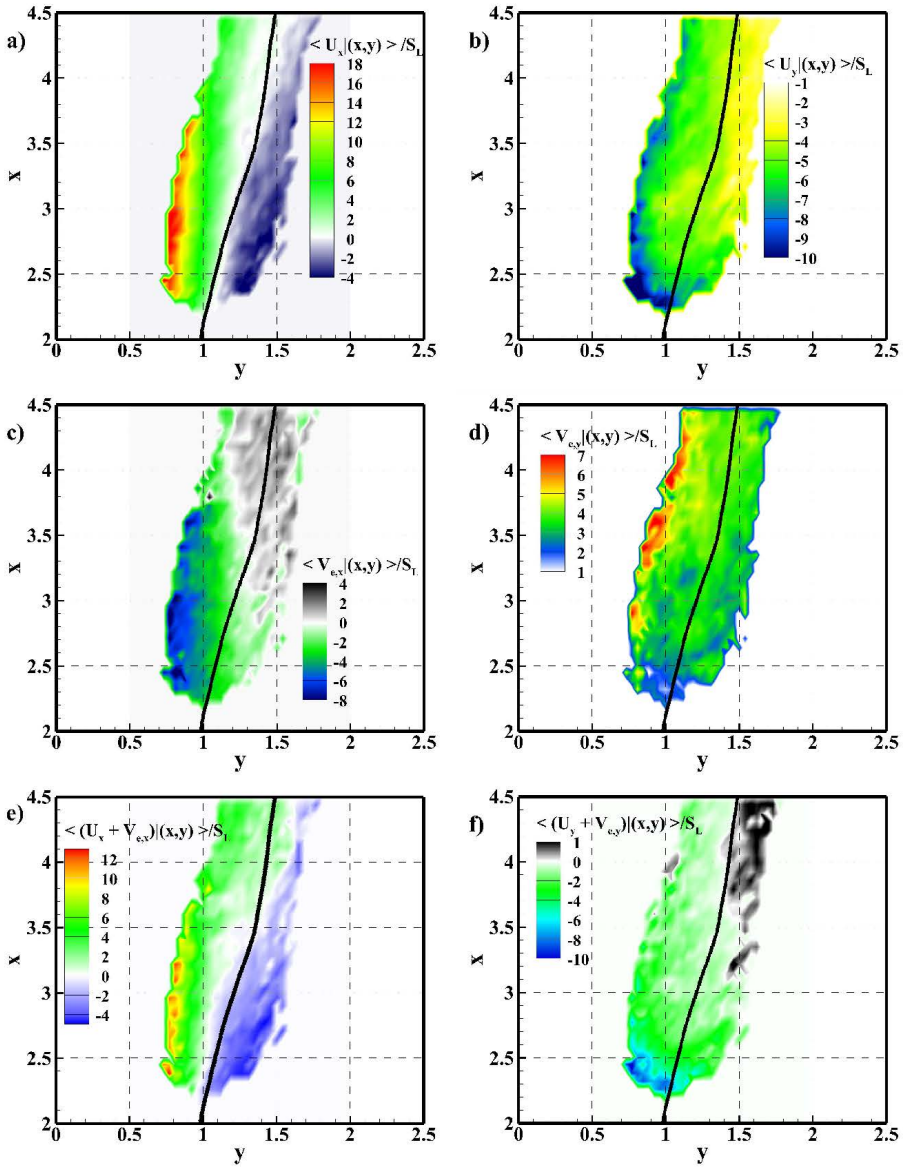

Fig. 5.4 The following quantities, conditionally averaged on both streamwise and transverse locations of the instantaneous flame base: (a) streamwise flow velocity; (b) transverse flow velocity; (c) the streamwise edge propagation velocity; (d) the transverse edge propagation velocity; e) the net streamwise velocity; and f) the net transverse velocity (the solid line is the temporally and spatially Favre-averaged mixture fraction equal to 0.07).

locities are doubly conditioned on streamwise and transverse locations of the instantaneous edge-flame locations. Figure 5.4 presents the (a) streamwise velocity, (b) transverse velocity, (c) streamwise edge propagation velocity and (d) transverse edge propagation velocity conditionally averaged on the streamwise and transverse instantaneous location of the flame base. The notation $< \ldots | (x,y) >$ represents the averaged quantity doubly conditional on streamwise and transverse locations of the edge flames.

The picture that now emerges is much clearer. In the below, it will be shown that the flame tends, on average, to move sequentially around its mean location in a clockwise manner. First, considering the mean streamwise velocity in figure 5.4(a), it tends towards being upstream movement on the lean side and downstream on the rich side. It is remarked that here when the rich/lean side is discussed at this point in the thesis it means the on-average rich/lean side, but note that by construction the edge flames are always located on a particular mixture-fraction iso-surface. In the transverse velocity, shown in figure 5.4(b), there is a tendency towards a strong entraining flow at low streamwise locations and a much smaller transverse (but still negative) flow at larger x values.

Flame propagation velocities also play key roles. The streamwise flame-propagation, shown in figure 5.4(c), tends mostly to counteract the streamwise flow, being generally positive on the lean side (i.e. the local flame speed is negative leading to downstream relative motion – suggesting an influence of high scalar dissipation values in some locations) and generally large and negative on the rich side (i.e. leading to upstream relative motion). The transverse flame propagation velocity, shown in 5.4(d), similarly seems to counteract the flow velocity in very rich mixtures and towards lower lifted heights. However, it does seem to play a key role towards longer lifted heights, as it causes the flame to propagate outwards despite the small inwards flow velocity.

The net streamwise and spanwise velocities are finally shown in figures 5.4(e)-(f). Now the proposed clockwise rotation is apparent. While there are obviously large fluctuations around the averaged picture, an indicative cycle could start from the 3 o'clock location, around $x \approx 3.3$ and $y \approx 1.4$, where the flame moves downwards and inwards. At 6 o'clock, around $x \approx 2.3$ and $y \approx 1.0$, the flame is being strongly entrained into the jet, where it reaches a region of high streamwise velocity that exceeds the flame propagation speed, pushing it downstream again. In principle the flame would then need to move through 9 o'clock ($x \approx 3.3$ and $y \approx 1.0$) then 12 o'clock to complete a cylce. Indeed, it can be observed that there is an outwards motion near 1 o'clock, round $x \approx 4.2$ and $y \approx 1.6$. It is proposed that this motion is connected with the passage of large eddies, a point which will be elaborated later. However, this two-dimensional picture still does not fully explain things, since the

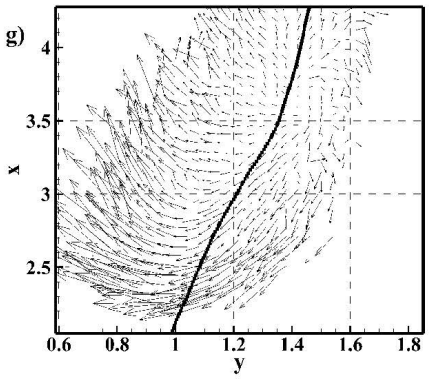

Fig. 5.5 The conditional average on both streamwise and transverse locations of the instantaneous of the relative velocity vectors conditionally averaged on streamwise and transverse location of the flames (the solid line is the temporally and spatially Favre-averaged mixture fraction equal to 0.07).

mean transverse velocity remains negative on the entire lean side, and hence the outwards motion through 9 o'clock and 12 o'clock is not supported by this analysis. To reinforce this, the mean velocity vectors are shown in 5.5. While the mean vectors clearly suggest a rotating pattern, they seem to suggest there is no way for flame edges to escape the high streamwise velocity and negative transverse velocity regions on the lean side.

At this point, out-of-plane motion needs to be invoked. While the mean out-of-plane velocities are obviously zero, they can be correlated with the flame-edge orientation to create a non-zero effect in this two-dimensional picture. Figures 5.6(a)-(b) now show the flow velocities with the out-of-plane component also considered. The out-of-plane component has little effect for the streamwise direction but noticeably reduces the magnitude of the inward transverse velocities on the lean side. Figures 5.6(c)-(d) show the net relative flame propagation velocities in the streamwise and transverse directions, respectively, with the out-of-plane components added in. Comparing these to the earlier figures 5.4 showing the in-plane components only, it may be observed that the out-of-plane flame propagation essentially tends to amplify the flame propagation effect. Of particular note in the transverse velocity is that it amplifies the positive velocity on the lean side. The resulting net velocities including both the flow and flame velocities and both in-plane and out-of-plane components are shown in figures 5.6(e)-(f). As can be seen while the streamwise component has a similar structure to the earlier discussion when out-of-plane motion was not considered, the transverse component is now much more consistent with an overall clockwise rotation, being consistently negative at low y values and consistently positive at higher values. Finally, the implied vectors are shown in figure 5.6(g), clearly showing a nearly complete clockwise rotation around the region of the most likely stabilisation point.

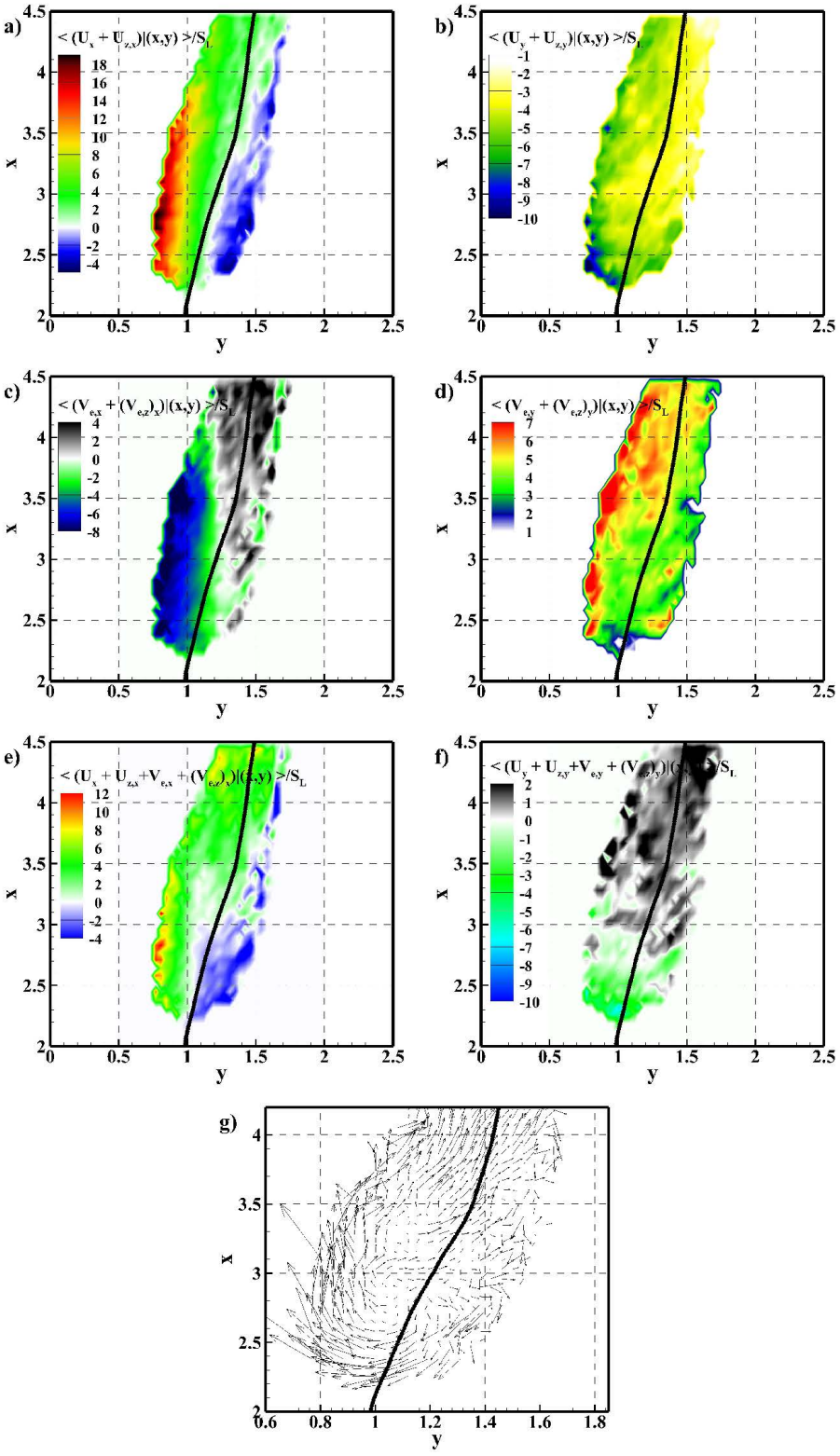

Fig. 5.6 The following quantities, conditionally averaged on both streamwise and transverse locations of the instantaneous flame base: (a) streamwise flow velocity with the out-of-plane component added; (b) transverse flow velocity with the out-of-plane component added; (c) the streamwise edge propagation velocity with the out-of-plane component added; (d) the transverse edge propagation velocity with the out-of-plane component added; e) the net streamwise velocity with the out-of-plane component added; f) the net transverse velocity with the out-of-plane component added; and g) the vectors of the relative velocity with the out-of-plane component added conditionally averaged on streamwise and transverse location of the flames (the solid line is the temporally and spatially Favre-averaged mixture fraction equal to 0.07).

There are two caveats to this picture that need to be mentioned. The first and most obvious is that the vectors suggest that flame edges that are located further downstream than $x \approx 3.5$ tend to continue to move downstream. It is suggested here that these are due mainly to the flame holes, both extinction and inclusion holes, which were not conditioned out of this analysis. It is also suggested that these are advected and eventually heal up at some location downstream. Further investigation of the evolution of the holes left for future work.

A second caveat is added that the consideration of the out-of-plane component disconnects the averaged picture with a Lagrangian coordinate system following individual flame-edge points, which despite any out-of-plane motion still move towards the jet centre, on average, in the on-average lean regions. It is speculated that this suggests that the on-average lean regions need to be a region of destruction of edges for this overall picture to be supported (with on-average production probably occurring towards the richer side). The destruction of these edges is presumed to occur, in the in-plane picture, mainly as a result of out-of-plane propagation and compressive out-of-plane strain, thus potentially explaining how the out-of-plane velocity components correct the overall picture. A framework for analysis of creation and destruction of flame edges has been developed, but this is left for future work, as it requires a significantly longer exposition.

5.3 Transport budget analysis

To complement the analysis of the instantaneous flame structures as performed in the previous sections, terms involved in the transport equations of the product mass fraction are analysed from a different, time and space-averaged standpoint. Following an earlier similar analysis of a lifted flame in a hot co-flow [41], the roles played, on average, by chemical reaction, mean convection and turbulent and molecular transport are identified. First, to provide some essential background, the average velocity field close to the flame base will be discussed. Earlier in section 5.2, it was noted that locally upstream flows were observed around the flame base. As this was an initially unexpected feature it is investigated in more detail. In figure 5.7, the colour contours represent the Favre-averaged product mass fraction, the dashed line is Z_{ms}, and the solid black and red lines are Y_p of 0.01 and 0.05, respectively. Velocity vectors, magnified by a factor of 5.0 in the region of $|y| > 1.0$, are shown to emphasise the flow structure. All quantities presented in this figure are averaged in the spanwise direction and time. Upstream of the flame in the region $0-1.5H$ a conventional entrainment flow is observed. However, around the flame base on the lean side, a *negative* axial velocity

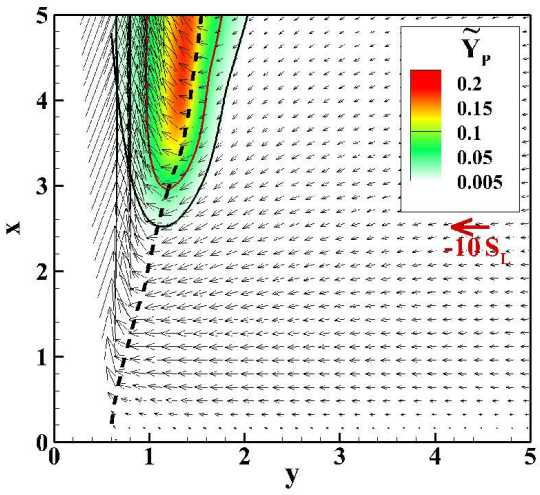

Fig. 5.7 Contours of product mass fraction with velocity vectors overlaid (the solid black and red lines are $\widetilde{Y}_p = 0.01$ and 0.05, respectively, and the black dashed line is $\widetilde{Z}_{ms}$).

may be noted. Lateral entrainment flow towards the jet in the outer regions is a well-known consequence of jet spreading and mass continuity, e.g. Ref. [80]. It is also obvious that flow has to diverge around a local heat releasing region, for example as observed around triple flames [126], and as in the well-known hydrodynamic Darrieus-Landau instability mechanism [127]. Given the heat releasing region has a large extent downstream of the flame base, the only region the entrainment flow can diverge towards is back towards to the nozzle. In this simulations, the co-flow velocity is very small ($0.002U_j$), so this leads to a locally negative velocity. This result is not without experimental support – a PIV-based study by Su *et al.* [1] found that for small lifted heights ($< 12H$), as is the case here, streamwise mean velocities lower than the co-flow were observed. The present work shows that this is due to entrainment flow. It is important to note however that this observed feature of averaged *upstream* streamwise flow is almost certainly only possible at low lifted heights, which may be observed for example in the measurements of Su *et al.* [1]. The role of flow divergence and deceleration around the flame edge was also reported by Upatnieks *et al.* [9, 123], although an on-average negative flow was not observed, consistent with expectations of the much larger lifted heights in those experiments.

The terms in the transport equation for the Favre-average of the instantaneous product mass fraction, Y_p, are defined in table 5.1, where U_x and U_y are the instantaneous streamwise and transverse velocities, respectively. Figure 5.8 shows the terms in table 5.1 on a colour scale. For reference the Favre-mean mixture fraction of 0.07 and the product mass fraction of 0.01 are also represented as dashed and solid black lines, respectively. As expected, the reaction rate (RR) is a strong positive term centred on the stoichiometric region. The

Table 5.1 Transport budgets of convection, diffusion and reaction

Mean convection in x (CX)	$-\frac{\partial \bar{\rho}\tilde{U}_x\tilde{Y}_p}{\partial x}$
Mean convection in y (CY)	$-\frac{\partial \bar{\rho}\tilde{U}_y\tilde{Y}_p}{\partial y}$
Turbulent transport in x (TTX)	$-\frac{\partial \bar{\rho}\widetilde{U_xY_p}}{\partial x}+\frac{\partial \bar{\rho}\tilde{U}_x\tilde{Y}_p}{\partial x}$
Turbulent transport in y (TTY)	$-\frac{\partial \bar{\rho}\widetilde{U_yY_p}}{\partial y}+\frac{\partial \bar{\rho}\tilde{U}_y\tilde{Y}_p}{\partial y}$
Laminar diffusion (LD)	$\overline{-\frac{\partial}{\partial x_j}\left(\frac{\mu}{\mathrm{Sc}}\frac{\partial Y_p}{\partial x_j}\right)}$
Product reaction rate (RR)	$\overline{\dot{\omega}_p}$

reaction rate term is contributed both from edge flames and the trailing diffusion flames. Convection in the streamwise direction (CX) is strongly negative in most regions but slightly positive on the outer edge of the flame base, which corresponds to the locally negative streamwise velocities that were observed in figure 5.7. The effects of the entrainment flow are strong and clearly observed in the convective term in the transverse direction (CY). There are a few experimental works that have discussed entrainment in lifted flames [1, 18, 105]. The present DNS shows it to be significant, at least at this lifted height. The turbulent transport in the streamwise direction (TTX) is weaker than other terms; however it has a positive contribution on the rich side which corresponds to gradient transport of products from downstream locations in the upstream direction. However, its contribution on the lean side is small, but negative over most regions of the flame, which corresponds to counter-gradient transport. The transition from gradient transport on the rich side to counter-gradient transport on the lean side is probably due to the decreasing turbulence intensity going from the jet core to the outer region. As discussed by Veynante *et al.* [128] such a transition with turbulence intensity also occurs in fully premixed turbulent flames.

A similar transition is observed in the transverse direction. In the inner turbulent core on the rich side, the transport is clearly out of the high product region and into the core. On the other hand, on the lean side, the transport term is once again negative, corresponding to counter-gradient diffusion, though it makes only a small contribution here relative to other terms. This counter gradient transport may be connected with heat release, but may also be connected with intermittent entrainment-driven eddies which cause the hook shaped structure noted earlier in figure 4.10, and appear to be involved.

Laminar diffusion is a relatively smaller term in all regions except the reaction zone.

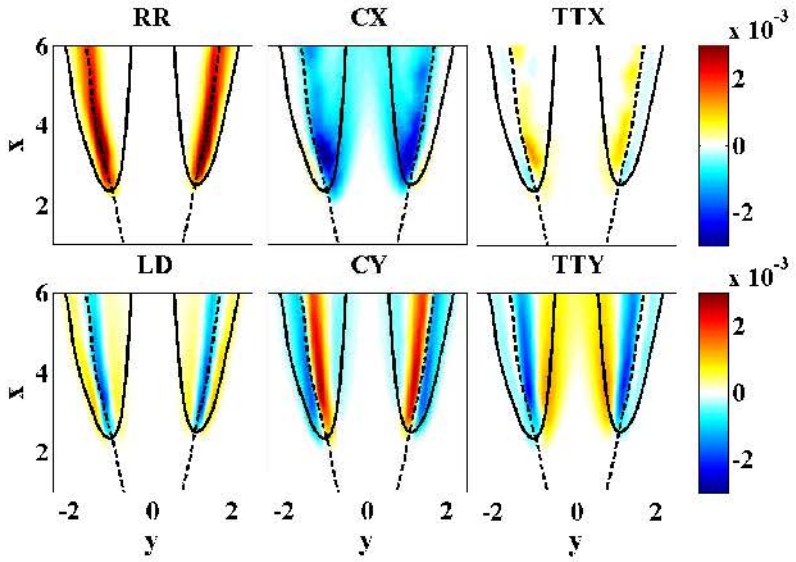

Fig. 5.8 Contours of the reaction, convection, diffusion, and turbulent transport terms(the solid line is $\widetilde{Y}_p = 0.01$ and the dashed line is $\widetilde{Z}_{ms}$).

The balance between these different terms is now discussed. This depends on the location within the flame, so for the sake of brevity in the next part of discussion, the right branch of the lifted flame will be discussed and to make the analysis more precise, the flame base is categorised into five distinguishable regions as shown in figure 5.9 and described as follows:

Region A is the starting point to understand the stabilisation mechanism in this particular flame. Region A is on the lean side and upstream of $Y_p = 0.01$ contour. A transverse cut through this region at a location upstream of the flame at $x = 2.2$ is shown in figure 5.10(a). In this region, the streamwise convection (towards the jet exit), turbulent transport, laminar diffusion all play a similar role and promote upstream flame transport. These are balanced by the transverse mean and turbulent convection terms, which both transport the flame into the jet core. Note that the role of these terms is consistent with the role of upstream transport played on the lean side in the instantaneous picture, and transverse transport into the jet core. The effect of propagation at this very farthest upstream region only involves the laminar diffusion part.

Region B is the region upstream of the flame base and on the rich side. The transport budgets in this region can be seen in the left side of stoichiometric line in figure 5.10(a) . In this region there is a balance of three terms: streamwise convection balances streamwise turbulent transport, and both mean and turbulent convection in the transverse direction, which as discussed with respect to region A, transport hot products from the lean to the rich side. In

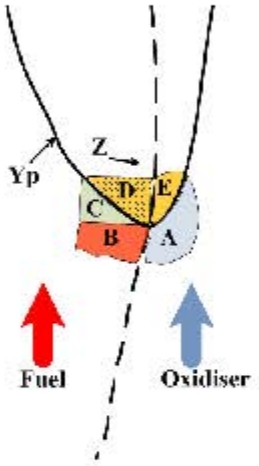

Fig. 5.9 Different regions in the vicinity of the flame base.

a flat turbulent premixed flame, one would expect the balance to be between convection and turbulent transport in this region – but in this lifted jet flame the entrainment flow complicates this situation and makes the stabilisation mechanism fundamentally two-dimensional.

Region C is inside the stoichiometric contour and outside of the contour of $\widetilde{Y}_p = 0.01$. The indicative transverse cut in this region, at $x = 3.6$, is shown in figure 5.10(b). In this region, there is a straightforward balance of transverse turbulent gradient transport and downstream convection.

Region D is inside the stoichiometric contour, downstream of the isoline of $Y_p = 0.01$, and within the region of high reaction rates. Figure 5.10(b) presents a transverse cut through this region at $x = 3.6$. On the lean side of $y = 1$, there is a complex balance between reaction rate, the effect of entrainment CY, and gradient turbulent transport in the streamwise direction, which are all positive terms, balancing streamwise mean convection and gradient turbulent transport in the transverse direction. Here the effects of propagation, which in the instantaneous picture, tends to balance flow in this region, would be observable indirectly via the reaction rate term. However, in this averaged picture the diffusion flame also contributes.

Region E is the final region and it is inside the stoichiometric contour, downstream of the isoline of $Y_p = 0.01$, and on the rich side of the region of high reaction rates. Figure 5.10(b) presents a transverse cut through this region at $x = 3.6$. In Region E, the laminar diffusion and reaction rate are positive terms that balance the incoming entrainment flow in the transverse direction, which is a similar balance that would be expected on the lean side of a counter-flow diffusion flame.

In summary, the transport budgets show the stabilisation mechanism is fundamentally two-

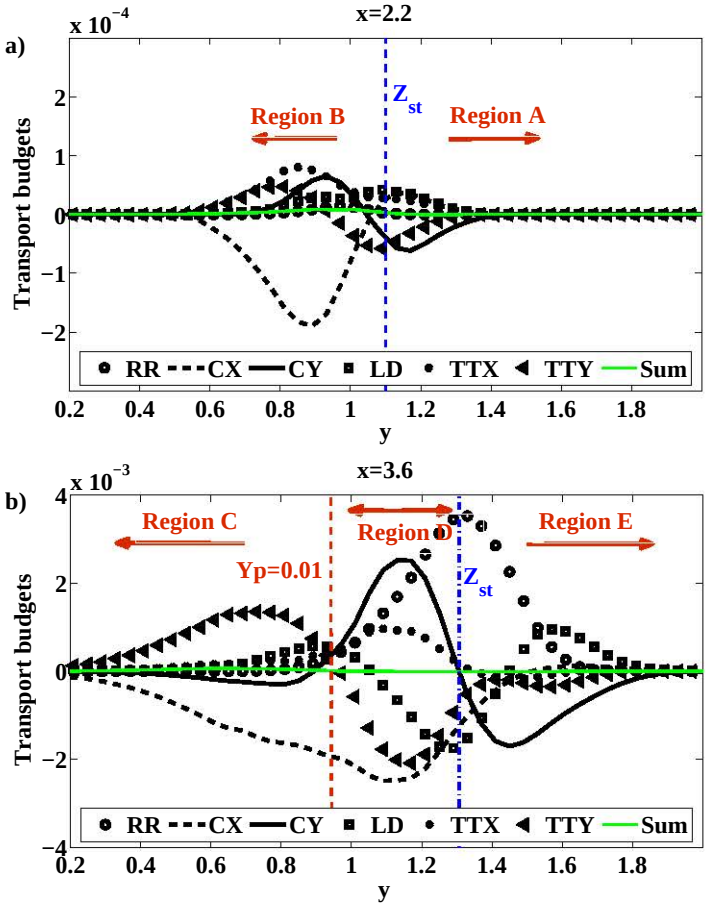

Fig. 5.10 The convection, diffusion, turbulent transport, reaction budgets in different streamwise location (the blue and red dashed lines are Z_{ms} and $Y_p = 0.01$, respectively).

dimensional: Region A is stabilised by upstream transport balanced against transverse transport into Region B; Region B is stabilised by transport from Region A and upstream; in region C there is a simple balance of downstream convection and transverse turbulent transport from the flame region; and finally in region D transverse transport out of the flame and downstream convection balance reaction and upstream transport. The two-dimensional structure of this balance seems to be consistent with the instantaneous picture, with instantaneous flame edges (and the trailing diffusion flames) essentially moving around between these regions in a cyclic, clockwise motion. Because averaging was performed in the third direction, it is however impossible to assess any out-of-plane effects in this framework. It is stated that its effect is embedded within the reaction term – i.e. the existence of high reaction rate regions in high average velocity regions is supported by the ability of flames to locally circumvent high streamwise velocity eddies by flows and flame propagation in the spanwise direction.

5.4 Conclusions

The statistics of flow and edge-flame propagation velocity components conditioned on the instantaneous locations of the flame revealed that the flow on average balances the relative propagation in the streamwise direction, thus demonstrating that the flame is stabilised essentially by edge-flame propagation. This is the first such demonstration, in a turbulent lifted flame, employing local flame propagation speeds.

There are significant fluctuations in lifted height and conditioning of the net flame velocity on streamwise and transverse location revealed an elliptical pattern of flame motion around the average stabilisation point. The motion was clockwise on the right-hand side of a vertical flame viewed horizontally. It is proposed that this motion is connected with the passage of large eddies. The observations are mostly consistent with the picture proposed by Su *et al.* [1], but suggest that in addition an out-of-plane motion around large eddies is required to explain how flames can escape the high streamwise velocity and entraining flow in the central region of the jet. In addition, at this small lifted height, local edge-flame velocities can be significantly lower than the laminar flame speed in some regions, suggesting a moderating role is also played by scalar dissipation.

It is also worth noting that the present results are in many respects consistent with the studies of Upatnieks *et al.*[9], who found that the passage of eddies was correlated with the perturbations in the height of the flame base. Similarly to Upatnieks *et al.* [9], in most phases through the passage of large eddies, we did not observe a positive correlation of the

edge flame relative speed with the flow velocity. However, fluctuations of the edge flame propagation speed did play key roles in certain phases of the cycles, particularly once the out-of-plane components of propagation were included, as this was needed to explain how the flame can escape the inner regions of high streamwise velocity.

Next, the flame was then analysed in an averaged sense. An interesting effect was observed where the entrainment flow locally bent around the flame location, which is a source of volume, to result in locally upstream flow on the lean side of the averaged flame stabilisation location. A budget of terms in the transport equation for the Favre-averaged mass fraction was then presented to provide support for the proposed stabilisation mechanism based on the instantaneous picture. The averaged structure was found to be fundamentally two-dimensional. On the lean side, upstream mean, turbulent, and laminar transport were balanced by entrainment into richer regions. On the rich side, the upstream turbulent transport and transport due to entrainment from the lean region balanced downstream convection. Downstream of this point the flame had a structure quite similar to a diffusion flame with subtle differences. On the lean side a quasi-laminar balance of reaction, laminar diffusion and entrainment was observed. In the core of the flame the downstream convection and laminar and turbulent transport of products out of the flame balanced reaction, entrainment from leaner regions, and – in contrast to what is expected in a diffusion flame – upstream turbulent transport of products. In very rich conditions downstream convection simply balanced transverse turbulent transport. Turbulent transport was found to be gradient-like on the highly turbulent rich side, and to have a small, but counter-gradient contribution on the weakly turbulent lean side. The averaged picture was broadly consistent with the instantaneous one (except of course that the out-of-plane effect could not be observed) with the proposed clockwise motion of individual flames leading to the above-described two-dimensional structure.

Overall the results provide strong support for the edge-flame theory of lifted flame stabilisation, with large eddies playing a key role in lifted height fluctuations.

Chapter 6

Edge flame statistics in a turbulent lifted flame

6.1 Introduction

In chapter 5, the stabilisation mechanism of a lifted flame was discussed and it was found that the edge-flame propagation is the main reason of the stabilisation. The importance of the edge-flame propagation in stabilisation, extinction and reignition have been highlighted in different previous laminar and turbulent flames numerically [3, 91, 129] and experimentally [13, 16, 109].

The edge-flame propagation velocity is a function of the propagation velocities of the product mass fraction and mixture-fraction iso-surfaces. The product mass fraction propagation velocity has been shown to be affected by local curvature in turbulent premixed flames [92, 103, 130]. However, in non-premixed flames, the edge-propagation velocity is affected by both the local mixture fraction gradient (scalar dissipation rate) and local curvature [91]. Non-premixed flames also experience contributions from the propagation velocity of the mixture fraction iso-surface. To the best of our knowledge this contribution has not been discussed in the literature.

This chapter therefore aims to shed light on the behaviour of the edge-flame with respect to the important parameters such as edge propagation velocities of the product mass fraction and mixture fraction iso-surfaces, curvatures and strain rates of the product mass fraction and mixture fraction iso-surfaces and scalar dissipation rate. Chapter 6 is organised as two main parts. In the first part, instantaneous behaviour of the edge-flame is investigated using the joint PDFs of the important quantities. In the second part, the quantities are analysed in a conditionally-averaged sense. This part includes the averaged quantities conditioned on

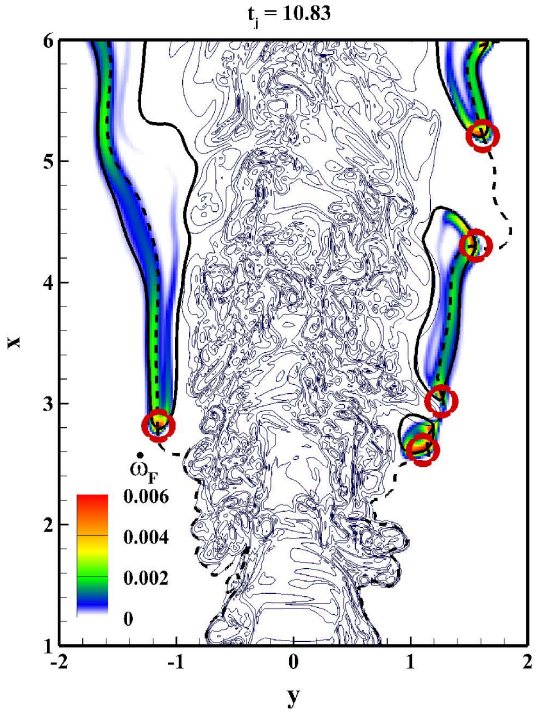

Fig. 6.1 Contour plots of reaction rate and vorticity on the plane $z = 0$. The solid black line is the product mass fraction, Y_p, of 0.2 and the dashed black line is the mixture-fraction, Z, of 0.07. The identified flame edges are marked as the centres of the red circles.

the streamwise and transverse locations of the flame base. The results of this part are used to support the observation in the first part of this chapter.

6.2 Orientation and motivating results

For orientation, figure 6.1 shows an instantaneous contour plot of reaction rate and vorticity at the $z = 0$ plane. The solid line shows the line of constant product mass fraction $Y_p = 0.2$ and the dashed line represents the mixture fraction equal to 0.07. The identified flame edges are marked as the centres of the red circles. It may be observed that the identified flame edges correspond well with regions of high reaction rate at the leading edge as well as at flame holes observed downstream.

The key results of chapter 5 are now recounted. In chapter 5, it was shown that on-average, the streamwise flow and flame propagation balance, thus demonstrating that the flame is stabilised by flame propagation. However, fluctuations of the edge-flame locations are significant. To demonstrate this point, figure 6.2(a) presents the joint PDF of the streamwise and transverse locations of the flame edge. The solid line is the temporally and

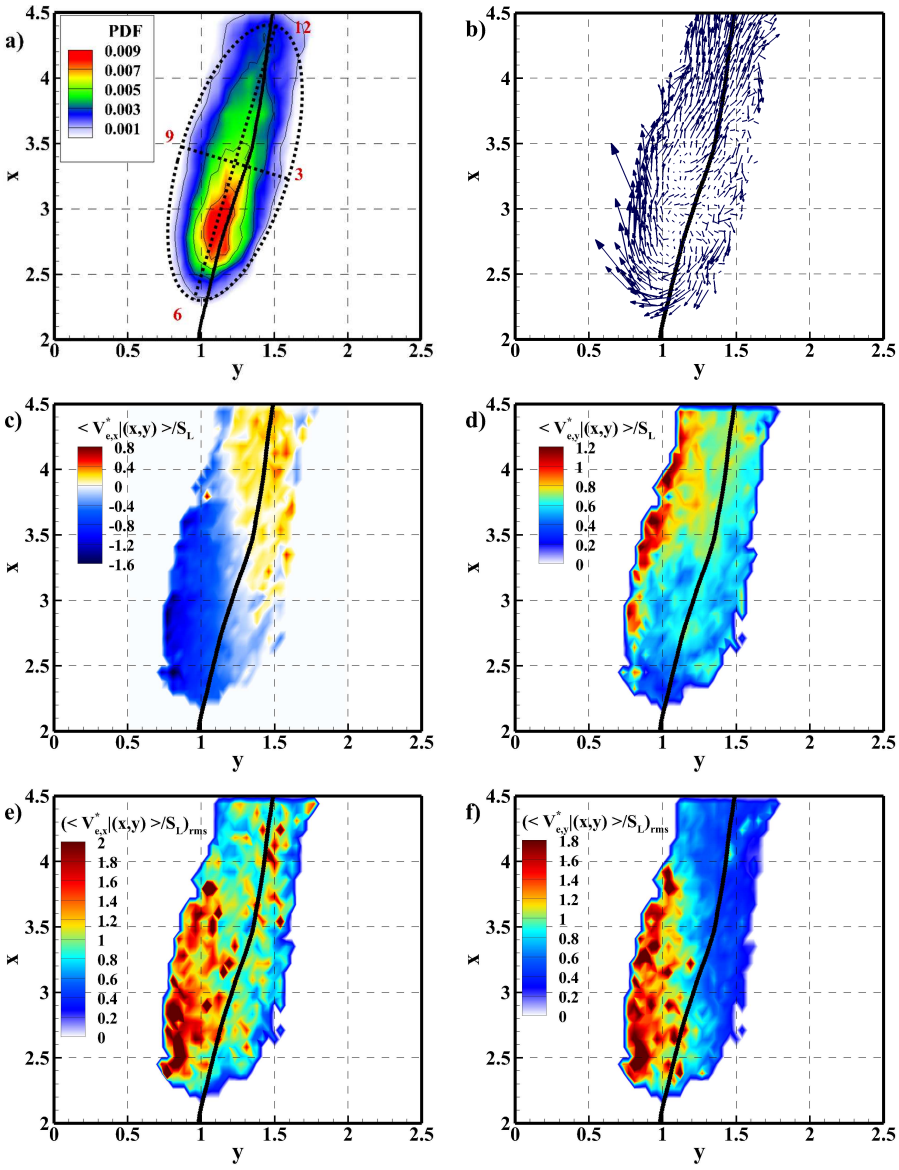

Fig. 6.2 a) the joint PDF of the transverse and locations of edge-flames. Overlaid is a representative clock face which will be referred to in order to facilitate discussions of the spatial structure in different regions. b)-f), the following quantities, conditionally averaged on the streamwise and transverse instantaneous location of edge-flames: b) the vectors of relative velocity with the out-of-plane component added, c) streamwise edge propagation velocity, d) transverse edge propagation velocity e) the root-mean-square fluctuation of the streamwise edge propagation velocity and f) root-mean-square fluctuation of transverse edge propagation velocity. In all the figures, the solid line is the temporally and spatially Favre-averaged mixture-fraction equal to 0.07.

spatially Favre-averaged mixture fraction equal to 0.07. As shown in several experimental studies [11, 23, 33, 113, 116, 123], the flame base moves on the periphery of the jet with a higher possibility of the flame base being close to the mixture-fraction of the maximum laminar flame speed, $Z_{ms} = 0.07$, and significant fluctuations of the edge-flame locations occur. To explain the key reasons behind the fluctuations, figure 6.2(b) shows vectors of the net edge-flame velocity (flow plus propagation). These vectors correspond to the net velocity at flame edges, observed by averaging over all x, y planes and time, including the effect of out-of-plane motion in each plane. The reader is directed to chapter 5 for further details of the methodology used to construct this plot. The key point is that a clockwise rotating pattern is observed. In chapter 5, it was suggested that this clockwise rotation is due to the passage of large eddies, along the lines of a previous suggestion by Su et al. [1], which refined earlier theories invoking a role of large eddies by Miake-Lye and Hammer [35], Kelman et al. [108], Tacke et al. [115] and Baillot & Demare [117].

In chapter 5, it was observed that the mean relative displacement speeds were not always close to S_L, and that fluctuations of the edge flame velocities were quite significant. The intent of this chapter is to investigate the cause of these on-average departures of the relative edge-flame propagation speed from the laminar burning velocity, as well as to understand the causes of the speed fluctuations.

To orient later discussions relating to this clockwise rotation and to different regions within the spatially-averaged flame structure, a representative clock face is sketched in figure 6.2(a). We will also refer to the lean and rich sides, which should be understood as the on-average lean or rich sides, since the flame-edges are always located instantaneously on the same mixture-fraction iso-surfaces.

Figures 6.2(c) and (d) show the normalised, density-weighted, streamwise and transverse components of the edge propagation velocity, conditionally averaged on the instantaneous streamwise and transverse locations of the flame base. The symbol $< \ldots | (x,y) >$ is the averaged quantity doubly conditioned on streamwise and transverse locations of the edge-flames. As may be observed, the streamwise flame propagation speed is mostly order of S_L. The streamwise component of the edge-flame relative velocity is small but positive (i.e. the propagation is in the downstream direction) towards the upper right half of the plot (i.e. from around 10:30 o'clock through around 5 o'clock), while it is negative (i.e. upstream propagation) and larger than S_L on the lower right hand side (from around 5 o'clock through 10:30). The transverse component is generally positive, i.e. the flame is tending towards outwards propagation, and significantly larger than S_L in the upper left of the plot (from 9 o'clock through 12 o'clock), and towards very rich regions from 6 o'clock through

9 o'clock. The on-average cyclic edge-flame motion around the stabilisation point shown in figure 6.2 implies that the flame undergoes cyclic fluctuations of the relative speeds as well.

The root mean square (RMS) fluctuations of streamwise and transverse edge propagation velocities are presented in figures 6.2(e) and (f), respectively, where the RMS fluctuation is defined for a quantity q as:

$$\langle q|(x,y)\rangle_{RMS} = \left(\langle q^2|(x,y)\rangle - \langle q|(x,y)\rangle^2\right)^{1/2}. \tag{6.1}$$

As can be seen, the fluctuations of the streamwise propagation velocity are high, at least the order of the mean velocities, and larger than S_L, and occur across all flame locations, but are somewhat stronger in the upstream and inner regions (bottom left of the plot). The fluctuations of the transverse flame propagation velocity are large on the rich side and relatively small on the lean side.

In summary the mean velocities can be significantly different from S_L while the velocity fluctuations are also significant in comparison to the mean and to S_L. This motivates further investigation of the reasons underlying these trends.

6.3 Edge-velocity statistics

In this section, the statistics of quantities obtained at all identified edge-flame locations are considered to learn which variables the speeds and orientations depend upon, in order to understand the overall dynamics. No spatial conditioning is applied in this section.

6.3.1 Contributions of S_d^*, S_Z^*, and normal vector orientations

The statistics of S_e^*, i.e. the edge-flame displacement speed along the mixture-fraction iso-surface towards reactants, are first investigated by looking into the correlations from its contributors, namely the term involving the displacement speed of product mass-fraction iso-surfaces, $S_d^*/S_L/\sqrt{1-k^2}$, and the term involving the displacement speed of the mixture-fraction iso-surfaces, $-k^*S_z/S_L/\sqrt{1-k^2}$. The effect of the normal vector alignment, measured by $k = \boldsymbol{N}_Z \bullet \boldsymbol{N}_{Y_p}$, is also considered.

Figure 6.3(a) shows the joint PDF of S_e^*/S_L and $S_d^*/S_L/\sqrt{1-k^2}$, whereas figure 6.3(b) shows the joint PDF of S_e^*/S_L and $-kS_z^*/S_L/\sqrt{1-k^2}$. In both figures, the conditional mean of the ordinate on the abscissa is also shown as a black line. Such conditional means will be shown throughout the chapter, but for brevity the fact that these lines represent the conditional means will not be mentioned henceforth. As shown in figure 6.3(a), the contribution

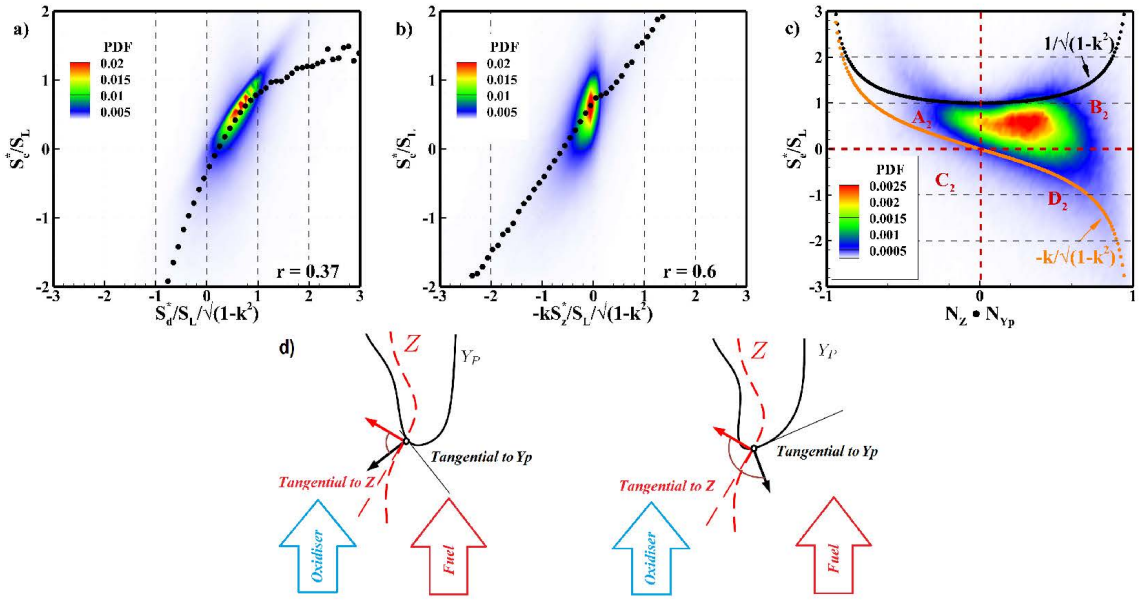

Fig. 6.3 Contours of joint PDFs of S_e^*/S_L with a) the contribution to S_e^*/S_L of the normalised product mass-fraction displacement speed ($S_d^*/S_L/\sqrt{1-k^2}$), b) the contribution to S_e^*/S_L of the normalised mixture-fraction displacement speed ($-kS_Z^*/S_L/\sqrt{1-k^2}$), c) the inner product k of the normal vectors to product mass-fraction and mixture-fraction iso-surfaces, and (d) a schematic of two scenarios for the alignment of the normal vectors.

of the product mass-fraction displacement speed, $S_d^*/S_L/\sqrt{1-k^2}$, is positive on average, although negative values are sometimes observed. The joint PDF is narrow and aligned with the conditional mean of S_e^*/S_L.

In contrast, figure 6.3(b) shows that the term $-kS_z^*/S_L/\sqrt{1-k^2}$ is generally negative. The joint PDF shows a broader region around the conditional mean value compared with figure 6.3(a). A positive correlation between S_e^*/S_L and both terms is observed.

Figure 6.3(c) shows the joint PDF of S_e^* and the inner product of the unit vectors normal to the mixture-fraction and product mass-fraction iso-surfaces, k. The yellow and orange dots show the terms $1/S_L/\sqrt{1-k^2}$ and $-k/S_L/\sqrt{1-k^2}$ which appear as coefficients of S_d^* and S_Z^* in equation 3.19. It is observed that the joint PDF of S_e^* and k generally lies between the orange and yellow curves. The significance of the black curve is that it is the expected behaviour if S_d^*/S_L is order of unity and $S_Z^*/S_L \approx 0$. The latter curve is the expected behaviour in the opposite situation ($S_d^*/S_L \approx 0$ and $S_Z^*/S_L \approx 1$). This latter situation is artificial, but it does seem to bound the likely regions quite well, perhaps coincidentally.

The most likely value of $k = \boldsymbol{N}_Z \bullet \boldsymbol{N}_{Y_p}$ is positive, but significantly smaller than unity, i.e. the vectors are somewhat but not fully aligned. Concerning the direction of the alignment, two possible scenarios corresponding to the alignment of $\boldsymbol{N}_Z$ and $\boldsymbol{N}_{Y_p}$ are presented in figure 6.3(d), schematically. Figure 6.3(c) shows that a positive inner-product is more probable,

i.e. the left schematic in figure 6.3(d). Further discussion of the reason for this bias requires an understanding of the spatially averaged picture, and this will be discussed later.

6.3.2 Responses to scalar dissipation rate

It has been suggested that scalar dissipation contributes to the stabilisation mechanism of non-premixed flames [10, 88]. Therefore, in this section the effect of scalar dissipation rate on the edge-flame displacement speeds and orientations will be discussed.

Figure 6.4(a) shows the joint PDF of S_e^*/S_L and logarithm of the normalised scalar dissipation rate and its conditional mean. The joint PDF shows a predominant negative correlation consistent with expectations from theory [33, 86, 128, 131–133] and the previous DNS study of Pantano [57]. The most probable S_e^* is approximately $0.6S_L$. A sudden drop of S_e^*, leading to negative values (i.e. local extinctions), may be observed in figure 6.4(a) to occur around $\chi S_L/\delta \approx 1$, as may be expected.

Figures 6.4(b) and (c) show the joint PDF of the contributions of the displacement speeds of the product mass-fraction (b) and mixture-fraction iso-surfaces (c) to S_e^*/S_L with the logarithm of the normalised scalar dissipation rate, and their conditional means. Both quantities show a negative correlation with scalar dissipation rate.

Figure 6.4(b) shows a smooth transition from high to low values of $S_d^*/S_L/\sqrt{1-k^2}$ as scalar dissipation rate increases, with a somewhat sharper fall-off after $\chi S_L/\delta \approx 1$. However, the term $-kS_Z^*/S_L/\sqrt{1-k^2}$ (figure 6.4(c)) features a more sudden drop at high values of scalar dissipation rate, suggesting it plays the leading role in such conditions.

Figures 6.4(d) and (e) show the joint PDFs of S_d^*/S_L (d) and S_Z^*/S_L (e) with scalar dissipation rate. It is noted that both PDFs are broad. A negative correlation with scalar dissipation rate is exhibited by S_d^*/S_L, as expected, whereas S_Z^*/S_L exhibits a positive correlation.

To explain the differences between the PDFs of the displacement speeds with and without the orientation factors included (e.g. that of $S_d^*/S_L\sqrt{1-k^2}$ in figure 6.4(b) versus that of S_d^*/S_L in figure 6.4(d)), the joint PDF of the inner-product of the normal vectors, k, is shown in figure 6.4(f). A clear correlation is observed, with low levels of alignment more likely at lower dissipation rate, and higher levels of alignment more likely at higher dissipation rates. This of course affects the joint PDFs of the orientation coefficients for S_d^*/S_L and S_Z^*/S_L in equation 3.19 with scalar dissipation rate, which are shown in figures 6.4(g) and (h). As can be seen, the orientation coefficient of S_d^* features a narrow PDF and a positive correlation with scalar dissipation rate, whereas the coefficient of S_Z^*/S_L features a broad PDF and a negative correlation with scalar dissipation rate. For large dissipation rates, the

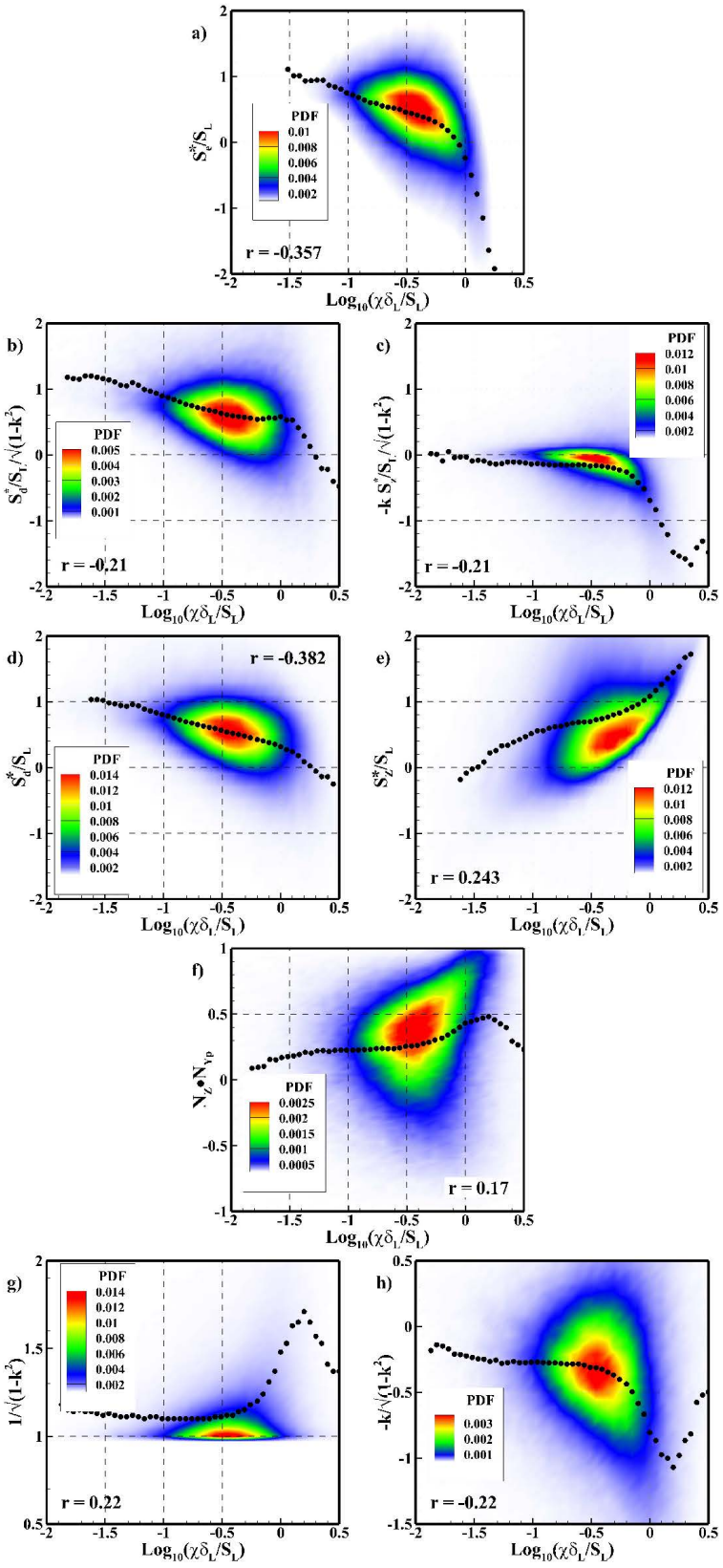

Fig. 6.4 The joint PDFs with logarithm of the normalised scalar dissipation rate of the following quantities and their conditional means: a) S_e^*/S_L, b) the net contribution of normalised product mass-fraction displacement speed to S_e^*/S_L, c) the net contribution of normalised mixture-fraction displacement speed to S_e^*/S_L, d) S_d^*/S_L, e) S_Z^*/S_L, f) the inner product of the normal vectors, k, g) the orientation term in contribution of S_d^*/S_L, and h) the orientation term in contribution of S_Z^*/S_L.

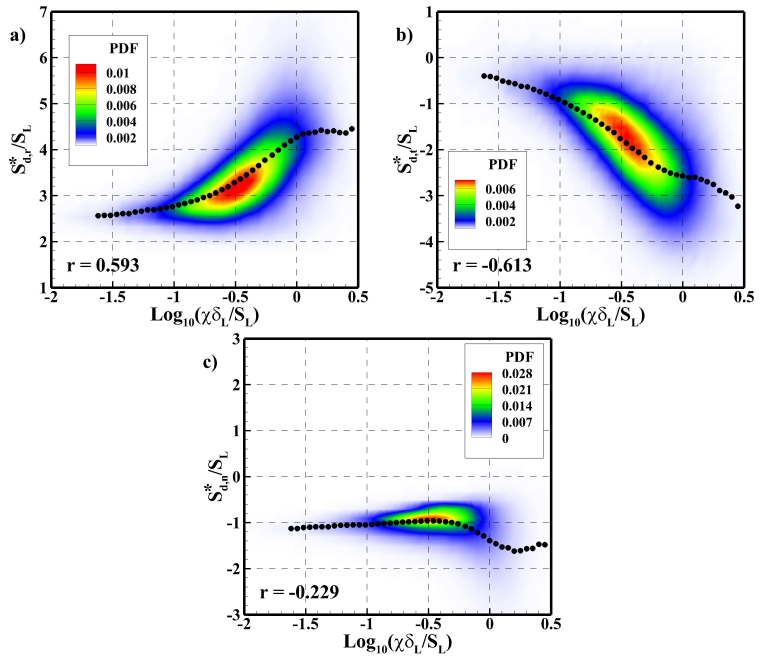

Fig. 6.5 The joint PDFs of the components of the product mass-fraction propagation velocity a) $S^*_{d,r}/S_L$, b) $S^*_{d,t}/S_L$ and c) $S^*_{d,n}/S_L$ with the logarithm of normalised scalar dissipation rate.

effect of the orientation coefficients can be quite significant. The orientation coefficient for S^*_d/S_L becomes large and positive while the orientation coefficient for S^*_Z/S_L becomes large and negative. This is a result of the normal vectors becoming well aligned, i.e. k increasing towards unity and thus the denominator becoming small. Such alignment is expected, because high dissipation rates are the result of persistent straining, which also tends to align scalar gradients, as noted in early studies of passive scalar mixing, for example study by Juneja and Pope [134].

Synthesising the picture from figures 6.4(a)–(g), S^*_d plays the main role in the scalar dissipation rate response for moderate dissipation rates. The mixture-fraction iso-surface displacement speeds are not insignificant for moderate scalar dissipation rates but a small orientation factor reduces their overall role. However, at large dissipation rates, the normal vectors tend to become aligned, which steepens the response of the S^*_d-related term, and results in a large contribution from S^*_Z to significantly increase the negative correlation with scalar dissipation rate, thus leading to more rapid extinction.

To further understand the response of S^*_d to scalar dissipation, S^*_d is broken down into components representing the effects of reaction, normal and tangential diffusion [71] – see equation 3.22.

The joint PDFs of the reaction, tangential and normal diffusion components of S^*_d with

scalar dissipation rate are presented in figure 6.5. It may be observed that the reaction term features a strong positive correlation with scalar dissipation rate whereas the tangential diffusion term exhibits a strong negative correlation. Figure 6.5(c) shows a weaker non-monotonic contribution of the normal diffusion term, especially at moderate dissipation rates, and also a narrow PDF around the conditional mean. Comparison of figures 6.4(d) and 6.5 suggests that the positive correlation of the reaction term with scalar dissipation rate must be dominated by the negative correlation of the tangential diffusion term for moderate scalar dissipation rates, with the normal diffusion term playing a role at larger dissipation rates.

The reason behind these correlations is now investigated. We first note that because the flame-edges are located at fixed product mass-fraction and mixture-fraction iso-surfaces, the reaction rate itself only experiences small fluctuations due to compressibility effects[1]. It can therefore be taken as a constant in this discussion. The reaction term is then simply proportional to the reciprocal of the magnitude of the product mass-fraction gradient, $1/|\nabla Y_P|$, which scales with the thermal thickness. The normal diffusion term is approximately proportional to the second derivative of mass fraction in the normal direction $-\nabla_n^2 Y_P/|\nabla Y_P|$ and the tangential term is curvature dependent. Figure 6.6(a) presents the joint PDF of $|\nabla Y_P|$ and scalar dissipation rate. In figure 6.6(a), a negative correlation of $|\nabla Y_P|$ and scalar dissipation rate may be observed. This can easily be understood in terms of the PDF of k, which shows that on average the normal vectors are not strongly aligned, and often close to perpendicular, implying that a compressive strain for mixture-fraction iso-surfaces, leading to high dissipation rates, corresponds more often to an extensive strain on product mass-fraction iso-surfaces. This correlation in turn leads to a positive correlation of the reaction term and scalar dissipation term (figure 6.5(a)). As shown in equation 3.22, the tangential diffusion term is proportional to the curvature of the product mass-fraction iso-surfaces. Figure 6.5(b) therefore suggests that there is an underlying correlation between the curvature and scalar dissipation rate. To confirm this, figure 6.6(b) shows the joint PDF of κ_p and $\log_{10}(\chi\delta_L/S_L)$. A strong positive correlation is observed as expected. Similarly to the above discussion, this may be explained considering the earlier result for the alignment of the normal vectors, shown in figure 6.3(c), which demonstrated that the most likely inner product of the normal vectors was significantly smaller than unity. In this situation, compressive strain in the direction of the mixture-fraction normal, which leads to high dissipation rates, causes increases of the product mass fraction curvature. Further discussion of curvature-related effects will

[1]This is the case because in this one-step chemistry model with unity Lewis number, the thermochemistry is completely determined to within compressible fluctuations by mixture fraction and product mass fraction.

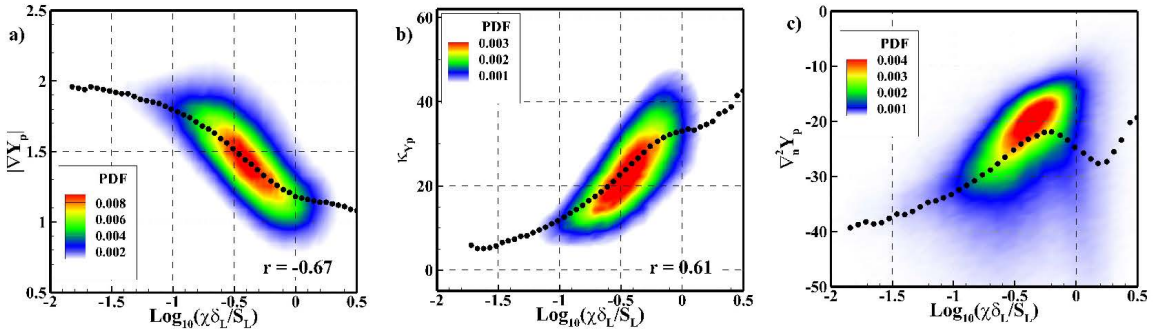

Fig. 6.6 Contours of the joint PDFs with normalised scalar dissipation rate of: a) the magnitude of the product mass-fraction gradient, b) the product mass-fraction curvature, and c) the second derivative of the product mass fraction in the normal direction.

be given in section 6.3.3.

To explain the trends for the normal diffusion component, figure 6.6(c) shows the joint PDF of $\nabla_n^2 Y_P$ and χ. As maybe observed, $\nabla_n^2 Y_P$ is negatively correlated in magnitude with χ, but this is offset by a positive correlation between χ and $1/|\nabla Y_P|$, which can be inferred from figure 6.6(a). For moderate dissipation rates, the correlation with $\nabla_n^2 Y_P$ is dominant, leading to a positive correlation for $S^*_{d,n}/S_L$ with χ. In contrast, for larger dissipation rates ($\log_{10}(\chi\delta_L/S_L) > -0.5$), the correlation with $1/|\nabla Y_P|$ dominates, leading to a negative correlation for $S^*_{d,n}/S_L$ with χ. We now investigate the behaviour of S^*_Z components. The joint PDFs of tangential and normal diffusion components of S^*_Z/S_L with scalar dissipation rate are presented in figures 6.7(a) and (b). The normal diffusion term in figure 6.7(a) shows a positive correlation with scalar dissipation rate whereas a negative correlation is observed for the tangential diffusion term in figure 6.7(b). The normal diffusion term is dominant, explaining the positive correlation of S^*_Z with scalar dissipation rate that was observed in figure 6.4(e).

The normal diffusion component is approximately proportional to $\nabla_n^2 Z/|\nabla Z|$. Figure 6.7(c) shows that $\nabla_n^2 Z$ varies approximately quadratically with $|\nabla Z|$, which can be understood with the scalings $\nabla_n^2 Z \approx 1/\delta_Z^2$ and $|\nabla Z| \approx 1/\delta_Z$, where δ_Z is a diffusive length scale. This explains the positive correlation observed between $S^*_{Z,n}$ and the scalar dissipation rate.

To explain the relatively weaker positive correlation between $S^*_{Z,t}$ and scalar dissipation rate, figure 6.7(d) shows the joint PDF of κ_Z and scalar dissipation. In the region that contains most of the sample, the correlation is positive. Extensive visual inspections of three-dimensional renderings of mixture-fraction iso-surfaces coloured by dissipation rate (not shown) suggest that this positive correlation results from specific eddy structures in the jet. The highest dissipation rates are observed to occur in structures which bulge out towards the oxidiser side, thus having a positive mixture-fraction curvature. (Further support for this

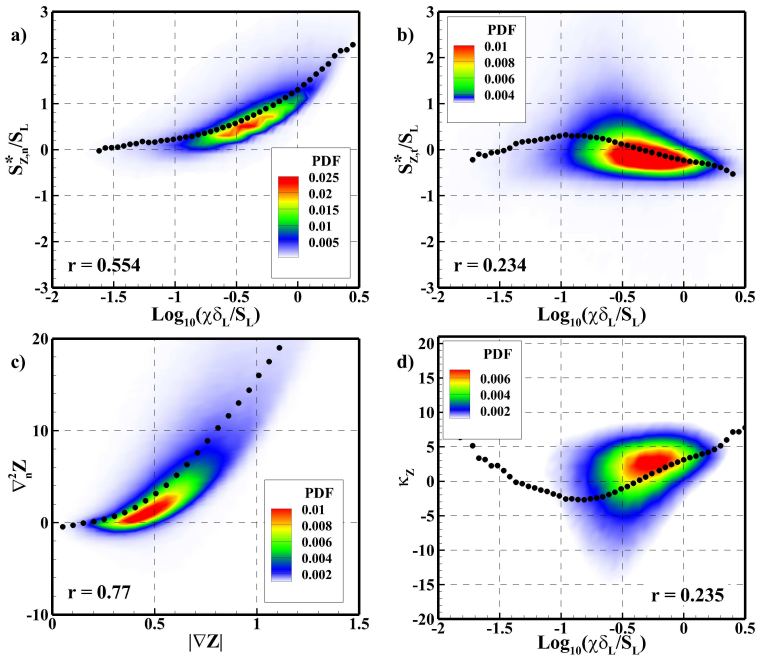

Fig. 6.7 The joint PDFs of the components of the mixture-fraction propagation velocity a) $S^*_{Z,n}$, b) $S^*_{Z,t}$ with the logarithm of normalised scalar dissipation rate, c) Laplacian of mixture-fraction normal to mixture-fraction iso-surface with mixture-fraction gradient; and d) the joint PDF of the mixture-fraction curvature and the scalar dissipation rate.

is given later.) As discussed above, higher gradients correspond to an even higher normal second derivative, which leads to the increase in the normal diffusion component of S^*_Z with χ.

6.3.3 Responses to curvatures

In fully premixed flames, it is well known that the curvature of reactive scalar iso-surfaces has a strong effect on local propagation speeds [71, 81, 91, 97, 102, 103, 135–139], the effect being Lewis-number and equivalence-ratio dependent. Moreover, as discussed in previous literature, for near-unity Lewis-number conditions, edge-flame propagation speeds respond negatively to the curvature of product mass-fraction iso-surfaces [81, 91, 97, 133, 140]. Although there is less discussion of its effect in the literature, in partially premixed flames, the curvatures of mixture-fraction iso-surfaces are also potentially important.

The aim of this section is therefore to understand the effects of these two curvatures on the behaviour of the edge-flame.

Figure 6.8(a) shows the joint PDF of S^*_e/S_L and the product mass-fraction curvature, κ_{Y_p}, whereas figure 6.8(b) shows the joint PDF of S^*_e and the mixture-fraction curvature, κ_Z. It is

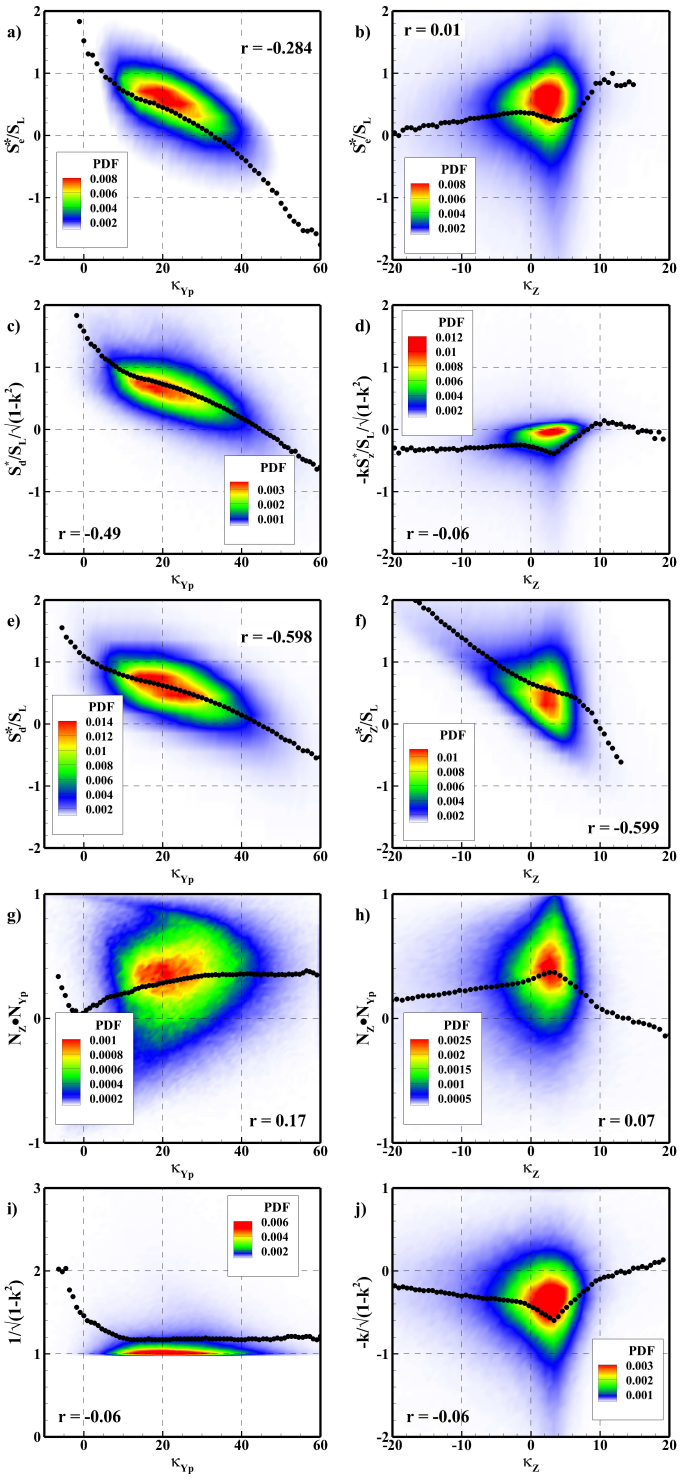

Fig. 6.8 Contours of: the joint PDFs of S_e^*/S_L with a) product mass-fraction iso-surface curvature κ_{Y_p} and b) mixture-fraction iso-surface curvature κ_Z; c) the joint PDF of the product mass-fraction displacement speed contribution to S_e^*/S_L and κ_{Y_p} ; d) the joint PDF of mixture-fraction displacement speed contribution to S_e^*/S_L and κ_Z; e) the joint PDF of the product mass-fraction displacement speed and κ_{Y_p}; and f) the joint PDF of mixture-fraction displacement speed and κ_Z; the joint PDF of k with g) κ_{Y_p}, h) with κ_Z, i) the joint PDF of the orientation factor in the contribution of the product mass-fraction displacement speed and κ_{Y_p}; and j) the joint PDF of the orientation factor in the contribution of the mixture-fraction displacement speed and κ_Z.

first observed that the product mass-fraction curvatures are almost always positive, unlike in fully premixed flames, where negative curvatures are observed frequently [81, 97, 102, 136, 138]. This is because of the strong curvature of the product mass-fraction iso-surface in the plane $\boldsymbol{N}_Z - \boldsymbol{T}_2$ - i.e. the plane containing the mixture-fraction variations and the direction of flame propagation. In contrast both positive and negative mixture-fraction curvatures are observed. Moving on to the correlations, it may be observed that the normalised edge-flame speed, S_e^*/S_L, is negatively correlated with the product mass-fraction curvature whereas it shows a weak positive correlation with the mixture-fraction curvature.

Figures 6.8(c) and (d) present the joint PDF of the terms involving in S_d^* and S_Z^* in equation 3.19 and the curvatures of the corresponding iso-surfaces. As shown in figure 6.8(c), the term corresponding to S_d^*/S_L exhibits a negative correlation with κ_{Y_p}. This is the main reason for the observed negative correlation for S_e^*/S_L in figure 6.8(a). However, as can be seen in figure 6.8(d), the term corresponding to S_Z^* shows a weak negative correlation with κ_Z.

Figures 6.8(e) and (f) show the joint PDFs of S_d^*/S_L and S_Z^*/S_L with the curvatures of their corresponding iso-surfaces. A clear negative correlation between each speed and its corresponding curvature is observed. A negative correlation of the displacement speed and flame front curvature was observed in previous studies of laminar edge-flames [140], premixed turbulent flames [103, 136, 137], and turbulent edge flames [81]. There is a good match for the qualitative trends with κ_{Y_p} between S_d^* and its component in S_e^*; however, while S_Z^* showed a clear negative correlation, the effect of κ_Z on S_e^* was much weaker. To explain these observations, the joint PDF of the inner product of the normal vectors k with the product mass-fraction and mixture-fraction curvatures are shown in figures 6.8(g) and (h), respectively. It may be observed that the correlation with κ_{Y_p} is weak except towards small and negative κ_{Y_p} values, while the correlation with κ_Z is stronger and non-monotonic. The effect of the orientation coefficients of S_d^* and S_Z^* in equation 3.19 (i.e. $1/\sqrt{(1-k^2)}$ and $-k/\sqrt{(1-k^2)}$ respectively) with the curvatures of their corresponding iso-surfaces are shown in figures 6.8(i) and (j). As can be seen, the coefficient of S_d^* has a low level of fluctuations and has a weak correlation with the product mass fraction curvature. Towards negative product mass-fraction curvatures, which occur very rarely, the orientation factor reaches higher values compared with the normal situation of positive curvatures. In other words, more alignment of the normal unit vectors is observed for negative curvatures. For the typical situation of positive curvatures, however, the mean value is almost constant. The orientation coefficient of S_Z^* in equation 3.19 in contrast features a much larger degree of fluctuations compared with that of S_d^*. It is negatively correlated with curvature for cur-

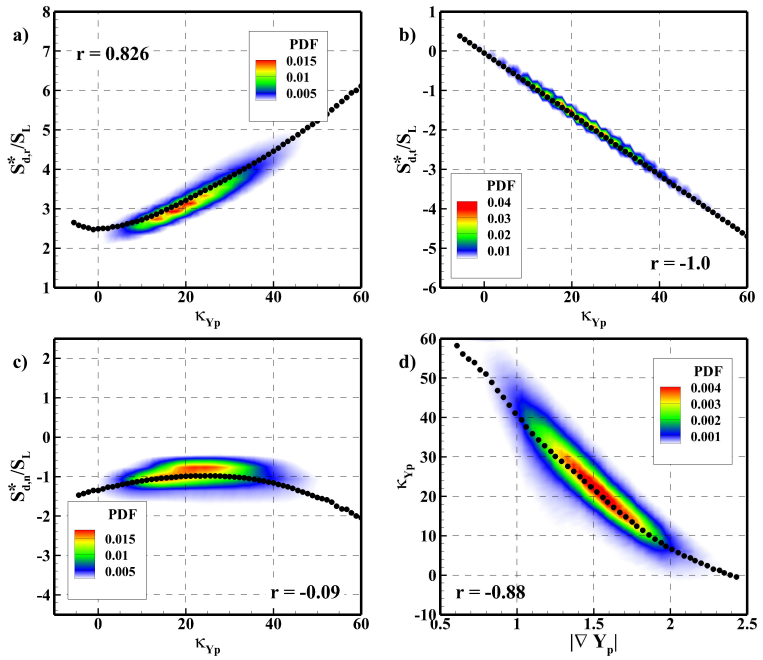

Fig. 6.9 Contours of: the joint PDFs with product mass-fraction curvatures (κ_{Y_p}) of a) $S^*_{d,r}/S_L$, b) $S^*_{d,t}/S_L$, c) $S^*_{d,n}/S_L$; and d) the joint PDF of κ_{Y_p} and the magnitude of the product mass-fraction gradient.

vatures smaller than roughly $4/H$, thus weakening the effect of the negative correlation of S^*_Z with curvature in this regime. For curvatures greater than roughly $4/H$, the orientation factor's correlation changes sign and therefore it increases the effect of the correlation of S^*_Z with curvature; however, in this region that correlation is small, so the net effect on S^*_e is minimal.

Understanding the behaviour observed in figures 6.8(e) and (f), requires the knowledge of the components of these two displacement speeds in response to their corresponding curvatures. The joint PDF of the components of S^*_d/S_L presented in equation 3.22 with the curvature of the product mass-fraction iso-surface are shown in figures 6.9(a)-(c). The reaction term is positive and increases with κ_{Y_p} (figure 6.9(a)). As discussed earlier, the product mass-fraction reaction rate is approximately constant. Therefore, this strong positive correlation is linked to the response of curvature to the product mass-fraction gradient, which will be demonstrated below. The tangential term shown in figure 6.9(b) has the expected negative correlation as per equation 3.22. The normal diffusion term presents a weak negative correlation with κ_{Y_p}. In contrast to the other two terms, it features a lower level of variations suggesting that it is not as important as the other terms in determining the overall trend.

To explain the trend for the reaction term, figure 6.9(d) shows the joint PDF of κ_{Y_p} and

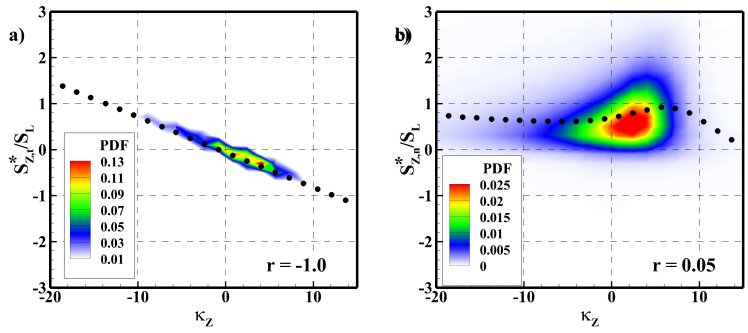

Fig. 6.10 Contours of: the joint PDFs with mixture-fraction curvature of the components of the mixture-fraction displacement speed a) tangential diffusion component; and b) normal diffusion component.

the magnitude of the product mass-fraction gradient, $|\nabla Y_p|$. The curvature of the product mass-fraction iso-surface is negatively correlated with $|\nabla Y_p|$. As $S^*_{d,r} \approx 1/|\nabla Y_P|$ this confirms that a $|\nabla Y_p|$ $-\kappa_{Y_p}$ correlation is the reason for the positive $S^*_{d,r}$ $-\kappa_{Y_p}$ correlation. Such a correlation is expected because the largest curvature of the product mass fraction iso-surfaces is expected to be found in the $\boldsymbol{N}_Z - \boldsymbol{T}_2$ plane. Compressive strain in the $\boldsymbol{N}_Z$ direction therefore increases this curvature, while simultaneously decreasing the $|\nabla Y_P|$ since the $\boldsymbol{N}_Z$ and $\boldsymbol{N}_{Y_p}$ vectors are not generally aligned. Note that this physical picture is quite consistent with the earlier discussion of the negative correlation of scalar dissipation rate with κ_{Y_p} that was discussed in relation to figure 6.6(b).

The joint PDFs of the components of S^*_Z/S_L, equation 3.22, and the mixture-fraction curvature, κ_Z, are presented in figure 6.10. The tangential term shows the expected linear relationship dictated by equation 3.22. However, within the region that contains most of the sample, the normal component shows only a weak positive correlation with the curvature leading us to conclude that the tangential term is the main reason for the observed negative correlation of S^*_Z with κ_Z. The earlier discussion regarding the positive correlation between curvature and scalar dissipation rate in figure 6.10(d) explains the weak positive correlation between the normal diffusion term and κ_Z.

6.3.4 Responses to strain

Many previous studies of premixed flames and partially-premixed edge-flames [81, 97, 102, 136, 138] have demonstrated strong effects of strain. These effects are therefore investigated in this section.

Figure 6.11(a) shows the joint PDF of S^*_d/S_L and the tangential strain rate of the product mass-fraction iso-surfaces. For strain rates up to about $0.1/t_j$, there is a positive correlation between S^*_d/S_L and a_{t,Y_p} while for higher strain rates, there is a negative correlation.

The above result can be explained considering the different effects of tangential strain according to the tangent orientation. Recall that the $\boldsymbol{T}_1$ direction is the mutual tangent vector between mixture-fraction and product mass-fraction iso-surfaces, while the $\boldsymbol{T}_3$ direction is the tangent to product mass-fraction iso-surfaces which is normal to $\boldsymbol{T}_1$. The alignment of $\boldsymbol{T}_3$ with $\boldsymbol{N}_Z$, which points towards the oxidiser side, tends to be good. Figure 6.11(b) shows the joint PDF of S_d^*/S_L with the strain rate $a_{\boldsymbol{T}_1}$ in the $\boldsymbol{T}_3$ direction while figure 6.11(c) shows the joint PDF of S_d^*/S_L with the strain rate $a_{\boldsymbol{T}_3}$ in the $\boldsymbol{T}_1$ direction. While both of these strain rates show the same non-monotonic trend, the decreasing response of S_d^* to increasing compressive strain (i.e. more negative) in the $\boldsymbol{T}_3$ direction is much stronger than the response in the $\boldsymbol{T}_1$ direction. In contrast, the decreasing response of S_d^* to increasing extensive strain is much stronger in the $\boldsymbol{T}_1$ direction than it is in the $\boldsymbol{T}_3$ direction. In a flat fully premixed flame, no statistical difference should be observed between these strain rates. Moreover, it is well known that for unity Lewis number conditions, S_d^* has a decreasing response to strain [97, 102, 138]. This therefore suggests that the different response of the edge-flame compared with a statistically flat premixed flame is due to curvatures. The largest curvature of the edge-flame is generally found in the plane containing $\boldsymbol{T}_3$ and $\boldsymbol{T}_2$ - i.e. the curvature moving around the narrow flame edge from the rich to the lean side. A compressive strain in this direction causes the curvature to increase, which significantly decreases the flame speed, explaining the overall positive correlation to the strain in the $\boldsymbol{T_3}$ direction. This picture is confirmed in figures 6.11(c) and (d), which plot the joint PDFs of product curvature and the strain rate in the $\boldsymbol{T}_1$ and $\boldsymbol{T}_3$ directions, respectively. As may be observed, the correlation for $a_{\boldsymbol{T}_3}$ is strong and negative, and recalling figure 6.8(e), a larger product curvature leads to a lower flame displacement speed. In contrast, extensive strain in the $\boldsymbol{T}_1$ does not affect the curvature, as it is mainly found in the orthogonal $\boldsymbol{T}_3$ and $\boldsymbol{T}_2$ plane, as shown in figure 6.11(c). Thus the strain tends to increase the product mass fraction gradient, which decreases the reaction term in S_d^* while leaving the normal diffusion term largely unaffected (c.f. figure 6.5(a) and the earlier discussion of the scalar dissipation effects in section 6.3.2). Considering the reaction term is decreased, and there is only a minimal effect on the curvature term, the overall S_d^* decreases with increasing strain in the $\boldsymbol{T}_1$ direction.

To investigate strain effects on the mixture-fraction displacement speed, figure 6.12 shows joint PDFs of: a) the normalised mixture-fraction displacement speed S_Z^*/S_L and the tangential strain rate of mixture-fraction iso-surfaces $a_{t,Z}$, b) $a_{t,Z}$ and the scalar dissipation rate χ, and c) $a_{t,Z}$ and the mixture-fraction curvature κ_Z. Figure 6.12(a) shows that like the product mass fraction iso-surfaces, the relationship is non-monotonic. The explanation

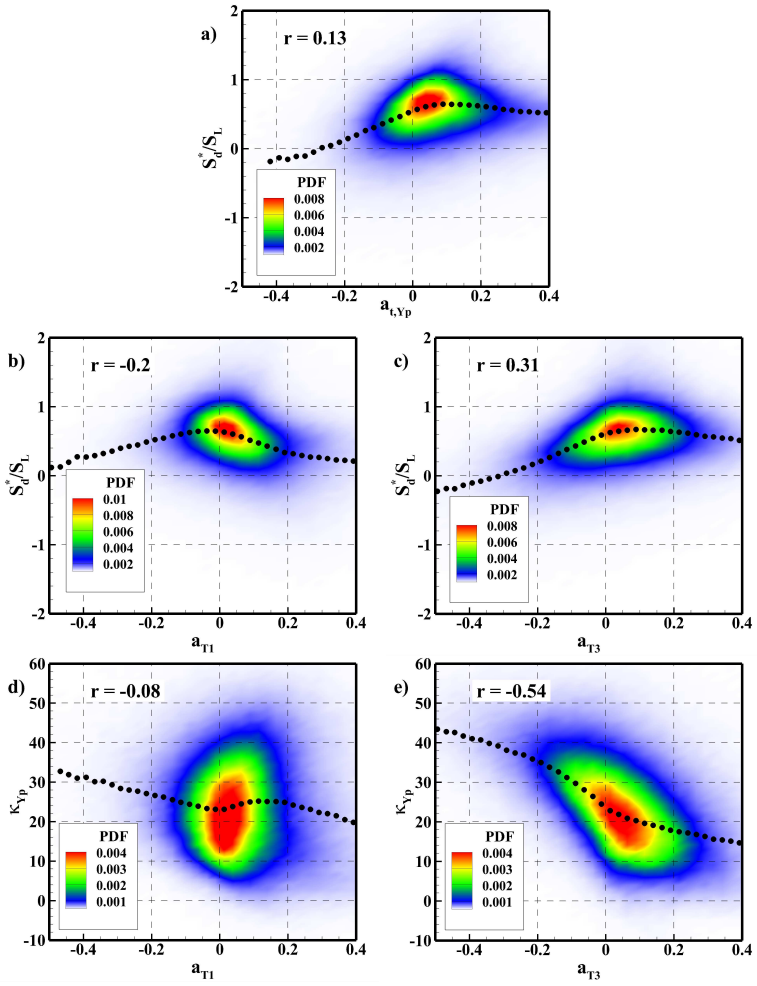

Fig. 6.11 Contours of: the joint PDFs of a) the product mass-fraction displacement speed and the tangential strain rate of product mass-fraction iso-surfaces; the product mass-fraction displacement speed and the strain rate of product-mass fraction iso-surfaces in the b) $\boldsymbol{T}_1$ and c) $\boldsymbol{T}_3$ directions; the product mass-fraction curvature and the strain rate of product-mass fraction iso-surfaces in the d) $\boldsymbol{T}_1$ and e) $\boldsymbol{T}_3$ directions.

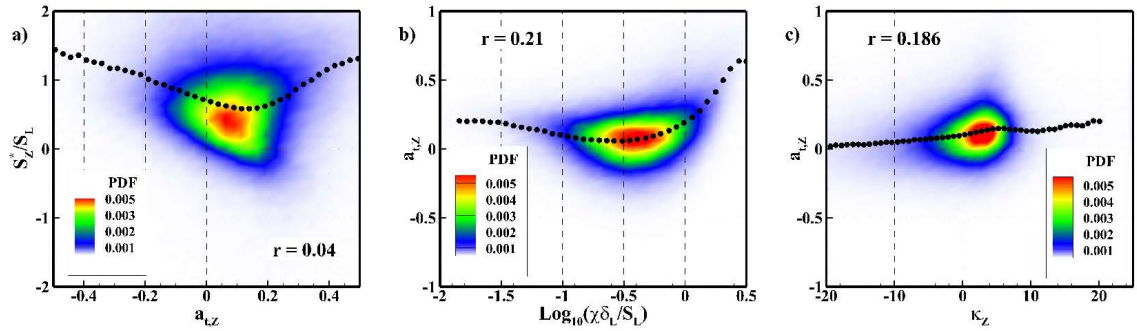

Fig. 6.12 Contours of: the joint PDFs of a) S_Z^*/S_L and the tangential strain rate of mixture-fraction iso-surfaces $a_{t,Z}$, b) $a_{t,Z}$ and the scalar dissipation rate , and c) $a_{t,Z}$ and the mixture-fraction curvature.

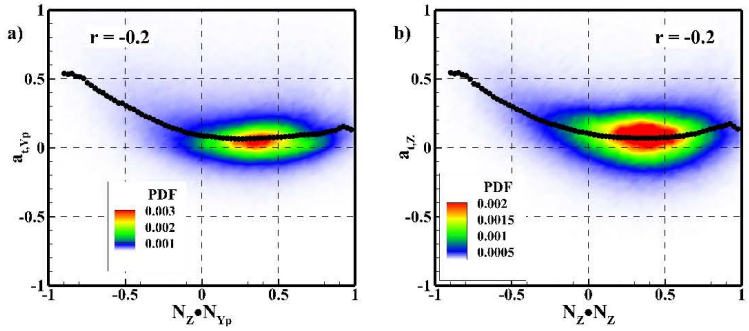

Fig. 6.13 Contours of: the joint PDFs of the tangential strain rates of a) the product mass-fraction iso-surfaces and b) the mixture-fraction iso-surfaces with the inner product of the normal vectors to these iso-surfaces k.

however is more straightforward. The positive correlation on the high strain rate side is explained by a positive correlation between scalar dissipation rate and tangential strain rate at high strain rates which is shown in figure 6.12(b), recalling from the discussion of scalar dissipation effects in section 6.3.2 that S_Z^*/S_L is positively correlated with χ (c.f. figure 6.4(e)). On the compressive strain side, the effect is explained by a negative strain-curvature correlation, shown in figure 6.12(c). Since more negative curvatures increase the flame speed, this explains the negative correlation with strain.

Orientation effects are now considered. Figures 6.13(a) and (b) show the joint PDFs of the tangential strain rate of product mass-fraction (a) and mixture-fraction (b) iso-surfaces with the inner product of the normal vectors to these iso-surfaces, k. The PDFs have the expected shape. For small extensive strains, the alignment is weak and the correlation is not strong, while for larger extensive strains the normal vectors tend towards being aligned or anti-aligned, with the former possibility being much more likely.

6.4 Averaged edge-flame responses

6.4.1 Averaged edge-flame velocity components

To explain the fluctuations of $V^*_{e,x}/S_L$ and $V^*_{e,y}/S_L$, the streamwise and transverse components of the edge-flame propagation, $S^*_e/S_L\boldsymbol{T}_2$, and mixture fraction iso-surface propagation, $S^*_Z/S_L\boldsymbol{N}_Z$, (see figure 3.7 for a schematic) are now discussed. Figures 6.14(a) and (b) present the streamwise component of $S^*_e/S_L\boldsymbol{T}_2$ and $S^*_Z/S_L\boldsymbol{N}_Z$, respectively, conditionally averaged at the instantaneous locations of the edge-flames. (Henceforth, we will simply refer to this as “conditionally averaged" and the quantity as the “conditional mean".)

As can be seen both streamwise components are negative on the rich side at low lifted heights and contribute almost equally to the negative $V^*_{e,x}/S_L$ (figure 6.2(c)), indicating upstream propagation. (We remind the reader that in the discussion of these figures, when we refer to the rich or lean side, we mean the on-average rich or lean side.) At higher lifted heights, either on the rich or lean side, the streamwise component of $S^*_e/S_L\boldsymbol{T}_2$ is positive, whereas the streamwise component of $S^*_Z/S_L\boldsymbol{N}_Z$ is negligible. Therefore, S^*_e/S_L dominantly contributes to the positive $V^*_{e,x}/S_L$ at high lifted heights, figure 6.2c. The conditional RMS fluctuations of the streamwise component of $S^*_e/S_L\boldsymbol{T}_2$ and $S^*_Z/S_L\boldsymbol{N}_Z$ are presented in figures 6.14(c) and (d). As can be seen, the streamwise fluctuations of $S^*_e/S_L\boldsymbol{T}_2$ are distributed relatively uniformly, whereas the streamwise fluctuations of $S^*_Z/S_L\boldsymbol{N}_Z$ are only strong on the rich side at low lifted heights. We can therefore conclude that the fluctuations of $V^*_{e,x}$ (figure 6.2(c)) at low lifted heights on the rich side is due to the contribution of both S^*_e and S^*_Z whereas in the other regions, S_e has the dominant contribution. Comparison of figure 6.14(b) with figure 6.14(d) also reveals that on average there is a positive correlation between the magnitude of $S^*_Z/S_L\boldsymbol{N}_{Z,x}$ and its fluctuations, while this is not the case for $S^*_e/S_L\boldsymbol{T}_{2,x}$.

Now turning to transverse propagation velocities (figures 6.14(e) and (f)), it is noted that the transverse component of $S^*_e/S_L\boldsymbol{T}_2$ is mostly positive except for a weakly negative central region in downstream areas. The transverse component of $S^*_Z/S_L\boldsymbol{N}_Z$ is positive across all flame locations, and strongly positive on the rich side at high lifted heights. Once again, therefore, both transverse component of $S^*_e/S_L\boldsymbol{T}_2$ and $S^*_Z/S_L\boldsymbol{N}_Z$ play a role to determine the net transverse edge flame propagation in figure 6.2. At large lifted heights, the contribution of $S_Z\boldsymbol{N}_{Z,y}$ is dominant on the rich side, while $S^*_e\boldsymbol{T}_{2,y}$ plays the leading role on the lean side.

The RMS of the transverse component of $S^*_e/S_L\boldsymbol{T}_2$ and $S^*_Z/S_L\boldsymbol{N}_Z$ are shown in figures 6.14(g) and (h). The fluctuations are observed to be particularly strong on the rich side, with both components contributing about equally, which leads to the trends observed in figure 6.2(f).

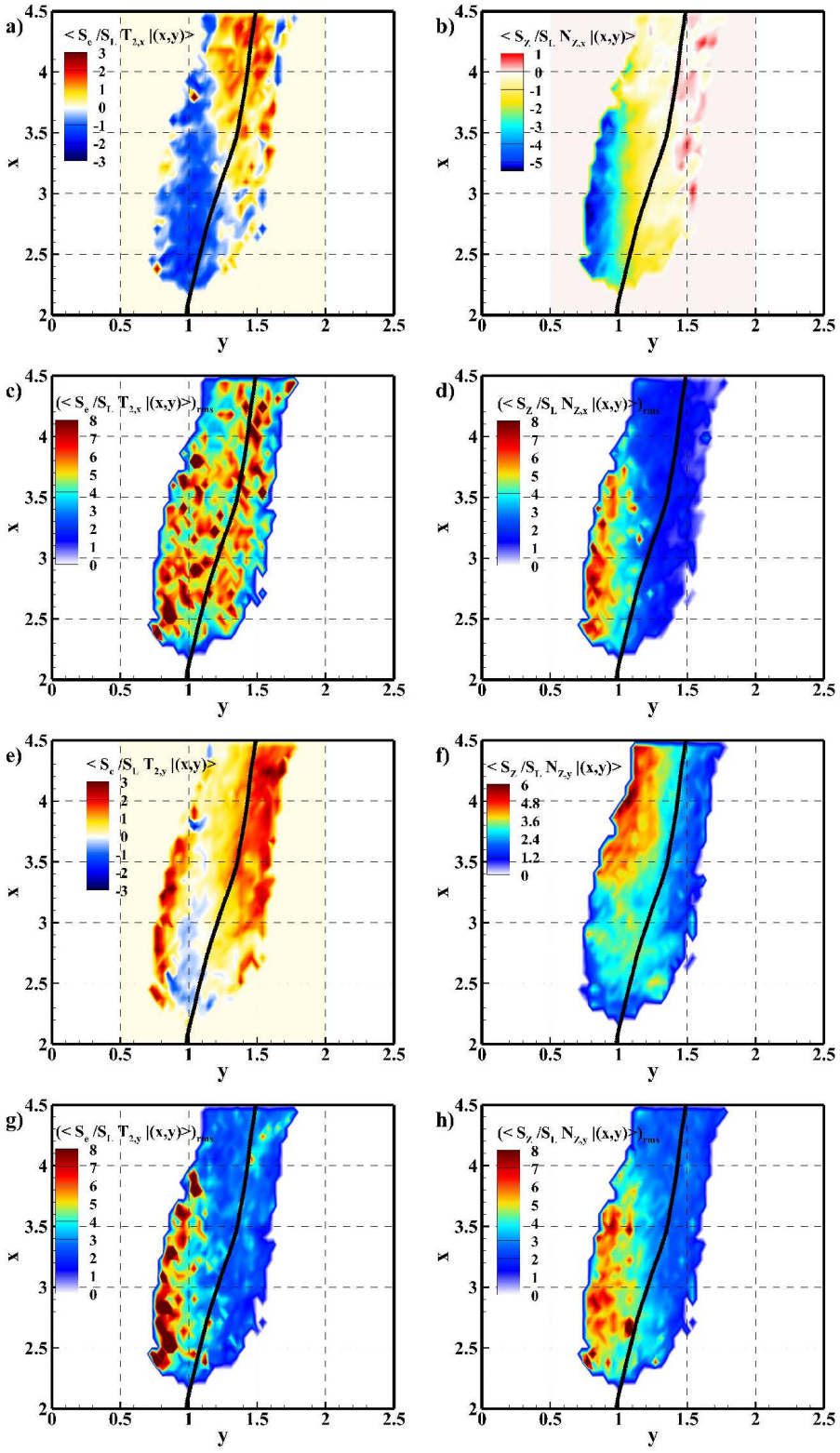

Fig. 6.14 The following quantities, conditionally averaged on both streamwise and transverse locations of the instantaneous flame base: the streamwise component of a) $S_e^*/S_L\boldsymbol{T}_2$ and b) $S_Z^*/S_L\boldsymbol{N}_Z$; the root-mean-square fluctuation of the streamwise component of c) $S_e^*/S_L\boldsymbol{T}_2$ and d) $S_Z^*/S_L\boldsymbol{N}_Z$; the transverse component of e) $S_e\boldsymbol{T}_2$ and f) $S_Z^*/S_L\boldsymbol{N}_Z$; and the root-mean-square of the transverse component of g) $S_e^*/S_L\boldsymbol{T}_2$ and h) $S_Z\boldsymbol{N}_Z$. In all figures, the solid line is the temporally and spatially Favre-averaged mixture-fraction equal to 0.07.

To explain the above observations, both the effects of variations of edge-flame orientations and edge-flame speed need to be considered. We begin by considering the former. To do so, it is necessary to first understand the trends for strain, since these significantly affect the orientations.

6.4.2 Strain and flame orientation variations

Figure 6.15(a) shows the conditionally averaged tangential strain rates of the mixture-fraction iso-surfaces, $a_{t,Z}$. It is readily observed that $a_{t,Z}$ is mostly positive, and strongest between around 10:30 though around 5 o'clock. Since mixture-fraction is a non-reacting scalar, its normal is likely to align well with the most-compressive fluid dynamic strain rate [101, 141] such that the regions of high $a_{t,Z}$ are likely to correspond with regions of high fluid dynamic strain. As such, effects on the orientations of the edge-flames and the relative orientations of the vectors normal to mixture-fraction and product mass-fraction iso-surfaces are expected.

To demonstrate the above point, figure 6.15(b) shows the conditional mean of the inner product $\boldsymbol{N}_{Y_p}$ and $\boldsymbol{N}_Z$, k. It may be observed that k exhibits a bias towards alignment on the upper right side, and a bias towards non-alignment on the lower left, except on the far left. The trends are remarkably consistent with those for the tangential strain rate $a_{t,Z}$.

The strain rates also affect the averaged orientations of the vectors. Figures 6.15(c) and (d) show the conditionally averaged unit vector normal to the mixture-fraction iso-surfaces, $\boldsymbol{N}_z$, and the unit vector normal to the mixture-fraction iso-surfaces, $\boldsymbol{N}_{Y_p}$, respectively. The unit normal vector of the mixture-fraction iso-surface is pointing towards the oxidiser at high lifted heights and turns somewhat towards clockwise at low lifted heights, indicating an on-average rotation of mixture-fraction iso-surfaces as they move through the clockwise rotating cycle of the flame edge around the mean stabilisation point. The vector $\boldsymbol{N}_{Y_p}$ (and also $\boldsymbol{T}_2$, not shown) goes through an even more significant rotation. Starting at large lifted heights on the lean side, around 1 o'clock, $\boldsymbol{N}_{Y_p}$ points outwards towards the oxidiser, and is well aligned with the averaged $\boldsymbol{N}_Z$. Moving downwards and inwards, through to 6 o'clock, $\boldsymbol{N}_{Y_p}$ rotates clockwise and eventually points downwards towards unburned reactants (approximately in the 7 o'clock direction). From 6 o'clock through around 10:30, the flame maintains this orientation, until it suddenly changes from 10:30 through 12 o'clock to point outwards towards the oxidiser side.

The normalised flame index (NFI) [84–86], defined as

$$\mathrm{NFI} = \frac{\nabla \mathrm{Y_F} \bullet \nabla \mathrm{Y_O}}{|\nabla \mathrm{Y_F} \bullet \nabla \mathrm{Y_O}|}, \tag{6.2}$$

can be used to distinguish between non-premixed and premixed burning. For premixed

flames, the NFI $\rightarrow +1$ while for non-premixed flames the NFI $\rightarrow -1$. Figure 6.15(e) shows the conditionally averaged NFI. It may be observed that the NFI is positive on the lower left side (in rich, upstream regions), but negative on the upper rich side (across the whole lean side and also in rich, downstream regions). The mode of burning therefore is more premixed on the lower left than it is on the upper right, implying that the burning mode also undergoes cyclic fluctuations.

6.4.3 Displacement speed variations

Variations of displacement speed also affect the averaged edge-flame propagation velocity components. The contribution of the edge-flame speed S_e^*, representing flame propagation along mixture-fraction iso-surfaces towards reactants (see equation 3.19), is now investigated in more detail. Figure 6.16(a) presents the conditional average of S_e^*/S_L. It may be observed that S_e^*/S_L is generally positive, except in a small region on the very rich side, but smaller than unity. It generally increases at locations further downstream. Combining this information with the averaged $\boldsymbol{N}_{Y_p}$ vectors shown in figure 6.15 does not seem to explain the observed $< S_e^*/S_L \boldsymbol{T}_{2,x} | (x,y) >$ shown previously in figure 6.14, which was in the downstream direction on the upper right half of the plot. To explain this, figure 6.16(b) shows the correlation $< S_e^*/S_L \boldsymbol{T}_{2,x} > - < S_e^*/S_L >< \boldsymbol{T}_{2,x} >$. Evidently, S_e^* and $\boldsymbol{T}_{2,x}$ are highly correlated in the upper right region, explaining how the edge-flame propagation can on average be in the downstream direction in that region despite S_e^* being on average positive.

To further investigate the causes of S_e^* variations, figures 6.16(c) and (d) present the conditional average of S_d^*/S_L and S_Z^*/S_L, respectively. The displacement speed of the product mass fraction surface, S_d^*/S_L, is generally positive. It is significantly less than unity in the upstream region and gradually increases to around unity as the edge-flames move downstream as shown in figure 6.16(c). The reasons for this behaviour will be discussed later. The mixture-fraction displacement speed, S_Z^*, (figure6.16(d)) is also positive with the highest values on the very rich side. Figures 6.16(e) and (f) present the conditionally averaged terms $S_d^*/S_L/\sqrt{1-k^2}$ and $-kS_z^*/S_L/\sqrt{1-k^2}$. As shown in equation 3.19, these two terms contribute to the total edge speed, S_e^*. As can be seen comparing $S_d^*/S_L/\sqrt{1-k^2}$ to S_d^* accounting for the orientation of the normal vectors (via the factor $1/\sqrt{1-k^2}$) simply amplifies the S_d^* contribution. In contrast, when the orientations are accounted for, $-kS_z^*/S_L/\sqrt{1-k^2}$ has a strong negative contribution, particularly in downstream regions and towards very rich and very lean regions in the upstream area. Therefore, the negative S_e^* on the rich side observed in figure 6.16(a), is principally the consequence of the nega-

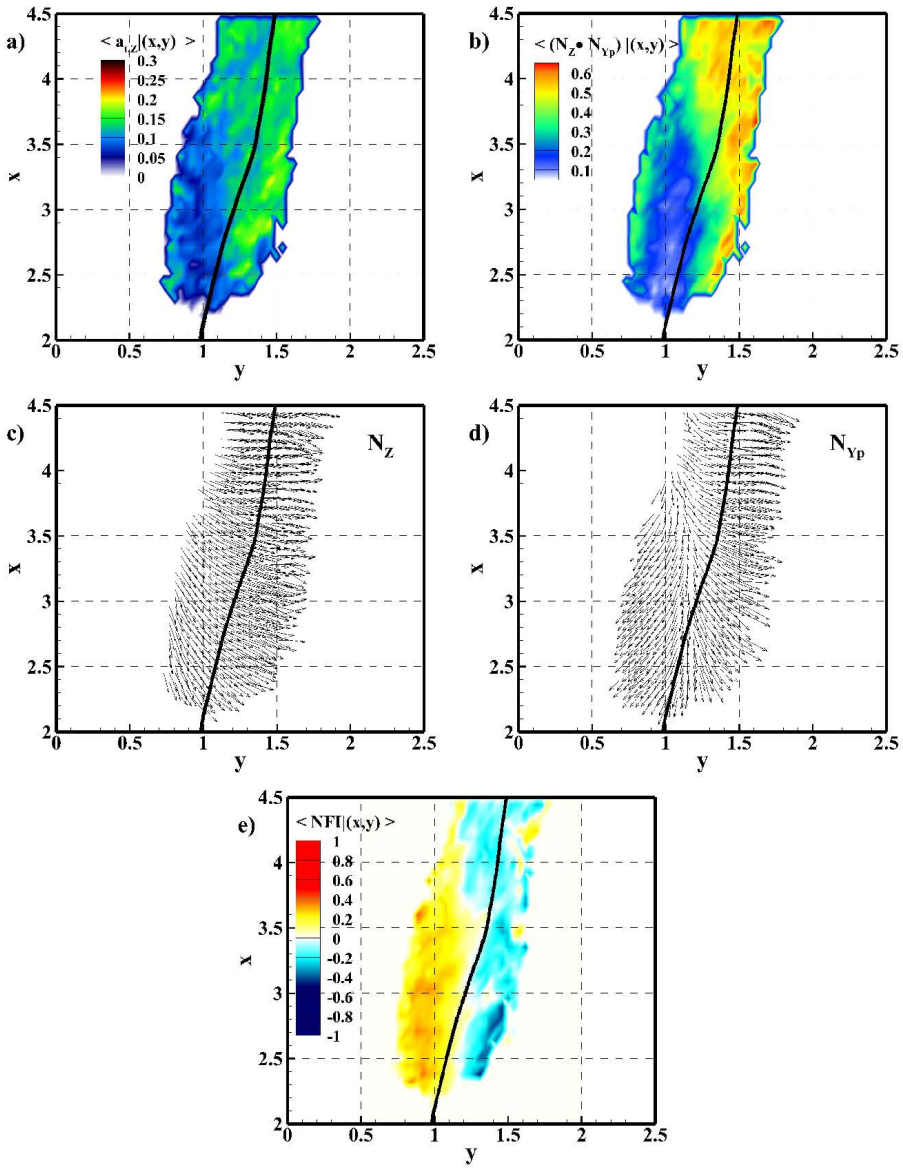

Fig. 6.15 The conditionally averaged: (a) contours of tangential strain rates of the mixture-fraction iso-surfaces $a_{t,Z}$, (b) the inner product $k = \boldsymbol{N}_Z \bullet \boldsymbol{N}_{Y_p}$, (c) vectors normal to mixture-fraction iso-surfaces $\boldsymbol{N}_Z$, (d) vectors tangential to product mass-fraction iso-surfaces $\boldsymbol{N}_{Y_p}$, and (e) the normalised flame index (NFI).

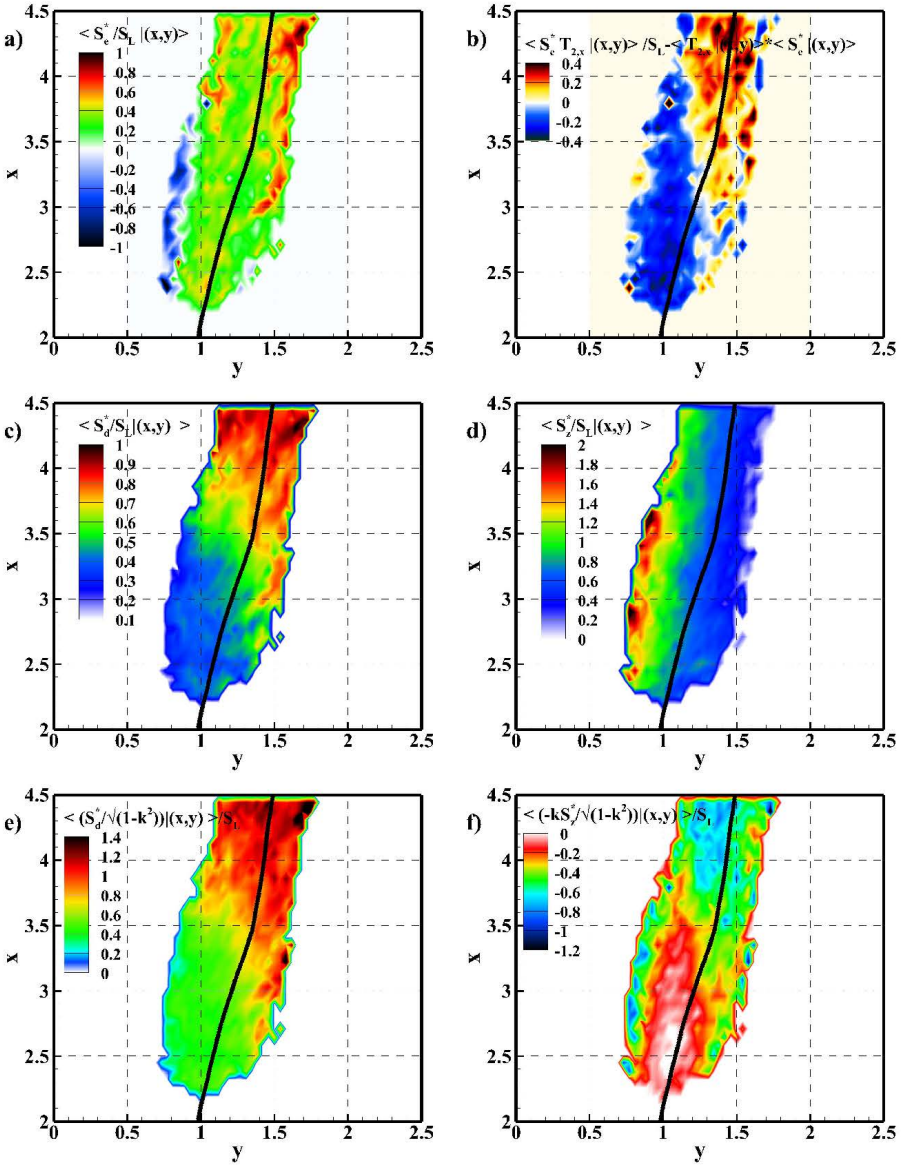

Fig. 6.16 The following conditionally averaged quantities: a) the normalised edge-flame propagation speed in the $\boldsymbol{T}_2$ direction, S_e^*/S_L, b) the correlation of S_e^*/S_L with the streamwise component of $\boldsymbol{T}_2$ c) the displacement speed of the product mass-fraction iso-surfaces, S_d^*/S_L, d) the displacement speed of the mixture-fraction iso-surfaces, S_Z^*/S_L, e) the contribution S_d^*/S_L to S_e^*/S_L f) the contribution of the S_Z^*/S_L to S_e^*/S_L. The solid line is the temporal and spatial Favre averaged mixture-fraction equal to 0.07.

tive contribution of $-kS_z^*/S_L/\sqrt{1-k^2}$. However, the regions of positive S_e^* are due to the strong positive contribution from the term $S_d^*/S_L/\sqrt{1-k^2}$ slightly weakened by the negative contribution form the term $-kS_z^*/S_L/\sqrt{1-k^2}$.

The spatially averaged trends for S_d^* are now discussed. It will be shown below, that these are a result of both strain and curvature effects. Beginning with the strain, figure 6.17 shows the conditionally averaged tangential strain rate a_{t,Y_p}. Overall it shows an opposite trend from the mixture-fraction iso-surfaces, $a_{t,Z}$, being larger on the bottom left (from 6 o'clock through around 10:30) than it is on the top right.[2] Recalling the earlier discussion of strain rate effects in section 6.3.4, S_d^*/S_L is negatively correlated with a_{t,Y_p}, so on the rich side, this correlation explains the less than unity S_d^*/S_L. It does not, however, explain the low values on the lean side.

To explain the lean side behaviour, the different responses to strain in the tangent directions $\boldsymbol{T}_1$ and $\boldsymbol{T}_3$ needs to be invoked. Figures 6.17(b) and (c) show the conditionally averaged strain rates in those directions, $a_{\boldsymbol{T}_1}$ and $a_{\boldsymbol{T}_3}$, respectively. Here, very different spatial patterns are observed. The strain rate in $\boldsymbol{T}_3$ direction is compressive, on-average in the region roughly between 3 and 5 o'clock. As noted in section 6.3.4, compressive strain in this direction causes the product mass-fraction curvatures to increase (c.f. figure 6.11(e)), which are also correlated well with high scalar dissipation rates (c.f. figure 6.6(b)). The high κ_{Y_p} leads to a high tangential diffusion contribution, which ultimately leads to a lower S_d^*. To confirm this, figure 6.17(d) shows the conditionally averaged κ_{Y_p} while figure 6.17(e) shows the dissipation rate χ. As expected, both show high values between around 3 o'clock to around 6 o'clock, explaining the low S_d^*/S_L in this region. It is also noted that the high dissipation rate values is consistent with persistent extensive tangential strain on mixture-fraction iso-surfaces on the lean side.

Finally it is noted that $a_{\boldsymbol{T}_3}$ is strongly extensive on the rich side, from 6 o'clock through to around 10:30. This leads to small product curvatures such that the curvature-effect is insignificant and the strain effect, which reduces S_d^* is dominant. In the downstream regions, $a_{\boldsymbol{T}_3}$ remains weakly extensive, reducing the curvature term in check, while the magnitude of $a_{\boldsymbol{T}_1}$ decays such that S_d^*/S_L can relax to unity.

Finally, the trends for S_Z^* are examined. Figures 6.18(a) and (b) show the conditionally averaged tangential diffusion and normal diffusion contributions to S_Z^*/S_L. The tangential

[2]The fact that a_{t,Y_p} shows the opposite trend from $a_{t,Z}$ on the lower left is expected because in this region the normal vectors are not aligned (c.f. figure 6.15(b)). In the region between 10:30 and 6 o'clock, the values are perhaps slightly smaller than expected given the tendency towards alignment of the normals to product mass-fraction and mixture-fraction iso-surfaces, but the alignment is not perfect, with the inner product around 0.5, which together with the lower peak values of the mixture-fraction strain, is probably sufficient to explain the low a_{t,Y_p}.

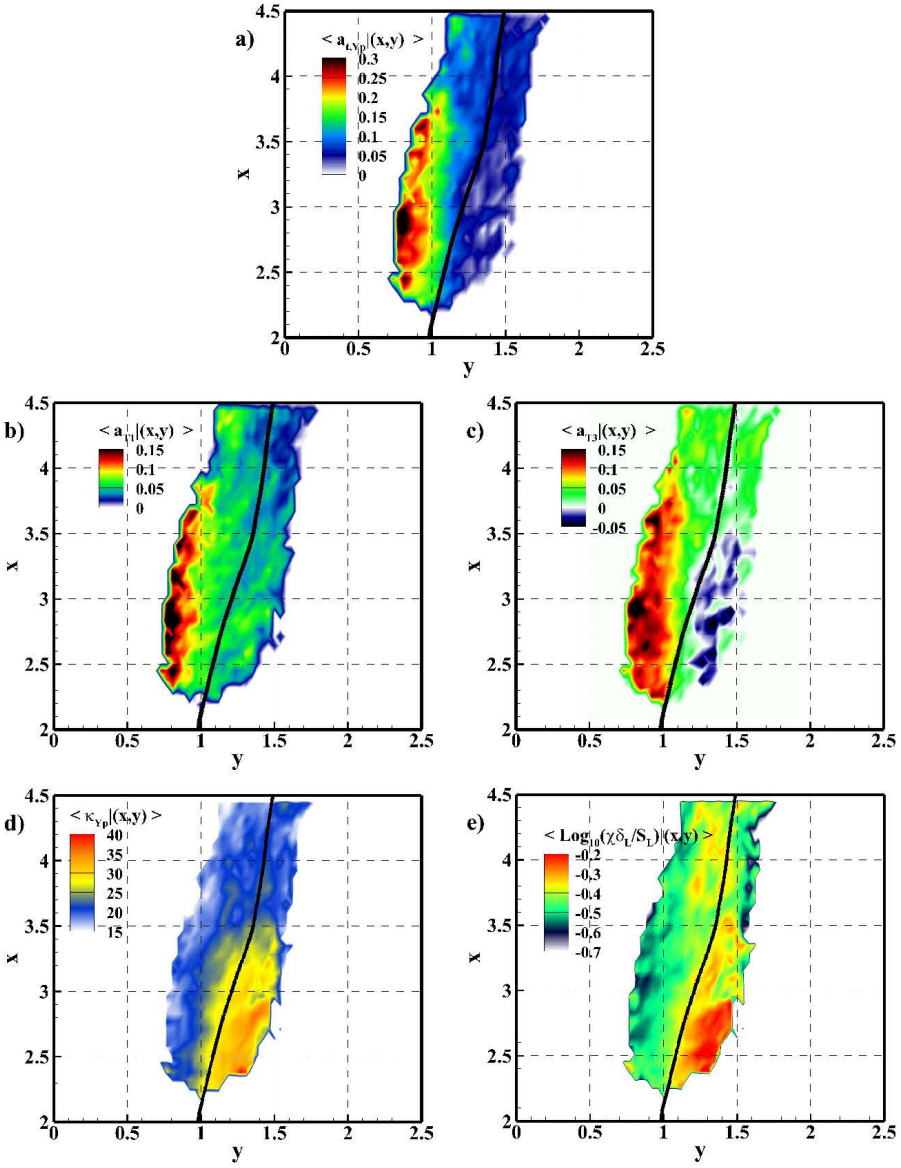

Fig. 6.17 The conditional averages of: (a) product mass fraction tangential strain rate $a_{t,Yp}$, (b) strain in the $\boldsymbol{T}_3$ direction, $a_{\boldsymbol{T}_1}$, (c) strain in the $\boldsymbol{T}_1$ direction, $a_{\boldsymbol{T}_3}$, (d) product-mass fraction curvature κ_{Y_p}, and e) scalar dissipation rate χ. The solid line is the temporally and spatially Favre-averaged mixture-fraction equal to 0.07.

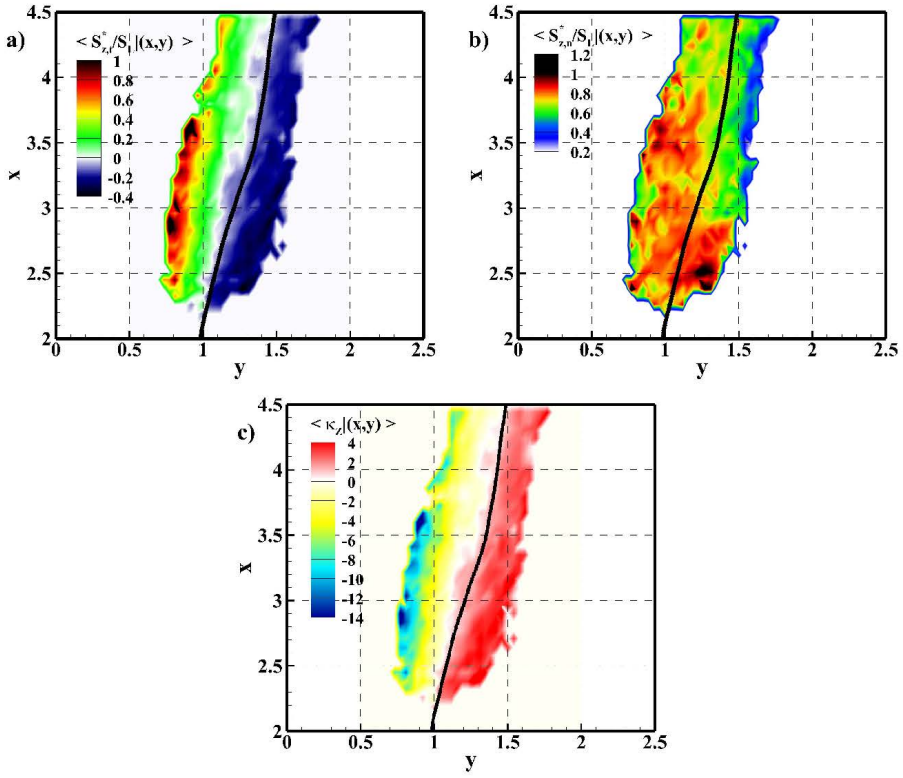

Fig. 6.18 The conditional averages of: a) the tangential diffusion contribution to S_Z^*/S_L, (b) the tangential diffusion contribution to $S_{Y_p}^*/S_L$, and mixture-fraction curvature. The solid line is the temporally and spatially Favre-averaged mixture-fraction equal to 0.07.

diffusion is negative on the lean side and strongly positive on the rich side. The normal diffusion term shows weaker spatial variations and remains on-average positive. There is some evidence of a downstream decay and a correspondence with regions of high scalar dissipation rate. To explain the tangential diffusion term, the conditional average of the mixture-fraction curvatures is shown in figure 6.18(c). As expected, the curvature on average is positive on the lean side and negative on the rich side. Also note that quite large negative values can be obtained on the lean side. These trends are consistent with large eddies pushing the flammable mixtures outwards, thus resulting in the positive curvatures on the lean side. As the eddy passes, the rapid entrainment causes large negative curvatures to develop at the bottom of the eddy. A schematic of this picture will be given later. The curvature effect therefore explains the large values attached by S_Z^* on the rich side while the moderate values on the lean side are a result of a competition between the normal and tangential diffusion components.

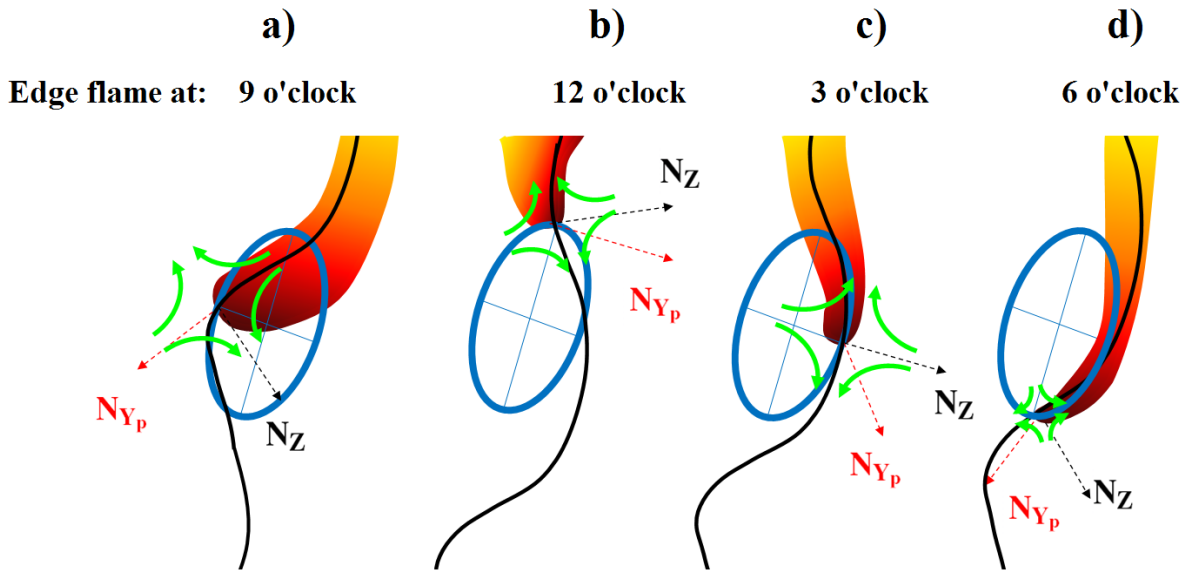

Fig. 6.19 A schematic to explain the edge-flame response to the passage of a large-eddy. The black line represents the mixture-fraction iso-surface. The red line represents the product mass-fraction iso-surface. The green curved arrows schematically represent the strain direction. The indicative directions of the normals to mixture-fraction and product mass-fraction iso-surfaces are shown as dashed arrows. The indicative clock-face is shown as the ellipse, with 9 o'clock, 12 o'clock, 3 o'clock and 6 o'clock marked.

6.5 Discussion

The above picture is now synthesised. It is proposed that the observations are consistent with the edge-flames' interactions with large eddies. Referring to the schematic in figure 6.19, in chapter 4, it was demonstrated that an on-average elliptical clockwise motion of the flame-edges occurs. It was proposed that this motion was due to the passage of large eddies, which was most consistent with the physical picture outlined by Su et al. [1]. The effects of the eddy on the edge-flame's speed, orientation, curvature, and strain rate are now folded in to our earlier picture. Moving around the representative clock-face, the following picture is proposed:

At 9 o'clock:

The flame is between large eddies. The net motion is downstream and outwards. The flow is downstream and inwards. The downstream is counteracted by upstream propagation due mainly to the S_d^* component of S_e^*. While S_e^* is not large in this region, it is well correlated with the flame orientation being in the upstream direction. The inwards flow is counteracted by outwards flame propagation due mainly to high S_Z^* as a result of high negative mixture-fraction curvatures. However, while it has not been discussed in this chapter, chapter 5 shows that out-of-plane motion is also important in this region, allowing flames to

escape regions of high inwards flow. In this region the normals are not well aligned, and the flame tends towards having a more premixed character. There is extensive strain in the $\boldsymbol{T}_3$, which tends to be aligned with $\boldsymbol{N}_Z$ causing low product curvature and low scalar dissipation rate. However, a large strain in the $\boldsymbol{T}_1$ direction (out-of-plane in the schematic) causes S_d^* to be low.

At 12 o'clock:

The flame is at the top of a large eddy. The net motion is downstream and outwards. Although it has not been discussed in this chapter, extensive visualisations suggest that most edges that are moving downstream in this region are edges found on or about to form flame holes. These edges continue to move downstream until they are eventually annihilated. Edges that remain connected to the main leading flame however move outwards through this region. The streamwise flow is neutral and transverse flow is inwards but much smaller than in other regions. Flame propagation is outwards with contributions from both S_Z^*, and S_d^*. Mixture-fraction curvatures are low in this region. The tangential strain on mixture-fraction iso-surfaces is high as the large eddy begins to push the flame outwards. Between about 10:30 and 12 o'clock, the product mass fraction iso-surfaces have rotated significantly such that now the normal vectors are relatively well aligned. In this phase of the cycle, the flame has a more non-premixed character than the other phases. There is moderate $\boldsymbol{T}_3$ and $\boldsymbol{T}_1$ strain, and low product curvature which leads to a relatively large S_d^* compared with the other regions.

At 3 o'clock:

The flame is now at the outer-most point of the large eddy. The net motion is upstream and inwards. The streamwise flow is upstream and the transverse flow is inwards. Flame propagation is outwards with contributions from both S_Z^*, and S_d^*, although the contribution of S_Z^* is relatively weakened compared with other regions due to the high positive mixture-fraction curvature. The strain tangential to mixture-fraction iso-surfaces continues to be high and persistent tangential strain from 12 o'clock is increasing the scalar dissipation rate. The normals are still relatively well aligned, and relative to other regions, flame is less strongly premixed. However, from 3 o'clock through 6 o'clock, the alignment of normal is decreasing and the T_3 strain starts to become large and compressive, resulting in high product curvatures appearing through to 6 o'clock, and this decreases S_d^*.

At 6 o'clock:

Finally, at 6 o'clock, the flame is at the bottom of the large eddy. The net motion is inwards. The streamwise flow is small and downstream, but the transverse flow is strongly entraining, creating a hook-like structure. Flame propagation is upstream and outwards, but

relatively small in this region. The product mass fraction normal has now rotated so that the normal vectors are not well aligned, and the NFI is neutral. Tangential strain on mixture-fraction iso-surfaces is now small. Product curvature and scalar dissipation are still high and the $\boldsymbol{T}_1$-direction strain is beginning to increase, leading to low S_d^* persisting. The strain in the $\boldsymbol{T}_3$ direction has switched to extensive, so that the product curvature decreases from this point through to 9 o'clock.

6.6 Conclusions

Edge-flames have been studied in terms of their propagation speeds, the orientations of the normal vectors to mixture-fraction and product mass-fraction iso-surfaces, the curvatures of those iso-surfaces, strain rates in various directions, and gradients of product mass fraction and mixture fraction.

The key findings are as follows.

- Significant instantaneous fluctuations of these quantities were observed, as well as on-average variations depending on where the edge flame was located.
- The net flame relative propagation speeds are affected instantaneous and on-average by contributions from the displacement speeds of the product mass-fraction and mixture-fraction iso-surfaces as well as the orientations of the normal vectors. None of these influences can be ignored to fully understand the edge-flame behaviour.
- The displacement speed of the product mass-fraction is strongly reduced by the product curvature, which is enhanced when a compressive strain is oriented in the tangent direction $\boldsymbol{T}_3$ (pointing across the edge-flame, usually in the direction of the mixture-fraction normal). As compressive strain in this direction also usually leads to mixture-fraction gradients increasing, a negative correlation with the scalar dissipation rate is also observed. Large extensive strain in the tangent direction $\boldsymbol{T}_1$ (the mutual tangent of product mass-fraction and mixture-fraction iso-surfaces) also causes S_d^* to diminish.
- Variations of the mixture-fraction displacement speed are affected most strongly by mixture-fraction curvature, but normal diffusion plays a role to offset the displacement speed to positive values on average.
- As the flame moves around the on-average stabilisation point (outwards, then downstream, then inwards, and upstream again), it undergoes on-average cyclic variations

of the various flame speeds involved, the orientations of the normal vectors, gradients, and curvatures. It is proposed that these on-average variations are connected with the passage of large eddies. The overall picture is consistent with, but further elaborates, earlier proposals by Su et al. [1] and chapter 5, which in turn drew on several previous works including notably Refs. [35, 108, 115, 117].

In future work, our priorities include determining whether and how this picture depends on: lifted height, Lewis number, dilution, and configuration (e.g. slot versus round jet).

Chapter 7

Conclusions and suggestions for further work

7.1 Concluding remarks

Summary of the work

A direct numerical simulation of a turbulent, lifted, slot-jet flame was performed. In order to achieve a realistic parameter space in terms of the Reynolds and Damköhler numbers, or equivalently the ratios of the jet velocity to laminar flame speed, and the jet width to laminar flame thickness, a one-step chemistry model was employed. However, a mixture-fraction dependent activation energy was employed in order to replicate the strong equivalence-ratio dependence of the laminar burning velocity that is typical of hydrocarbon fuels. The DNS are the first of a lifted flame in an atmospheric temperature environment which are targeted at hydrocarbon combustion.

The thesis then comprehensively analysed the flame in terms of its overall structure and statistics, with a view to determining the stabilisation mechanism and understanding edge-flame dynamics. The flame was analysed both in terms of instantaneous statistics conditioned on the locations of edge-flames as well as Favre-averaged statistics.

The following summarises the key findings.

1- General structure of the flame

The overall structure of the flame was first examined. The flame was found to be composed of leading edge flames followed by a trailing diffusion flame. The edge flames were found to usually have single branch centred close to the stoichiometric mixture-fraction surface. Lean branches were never observed, and rich premixed branches were observed rarely. In contrast, previous hydrogen lifted-flame DNS observed a vigorous inner rich premixed

flame. This leading order structural difference may be connected with the rather different flammability limits of hydrogen as compared with hydrocarbons.

Hook-like structures observed similar to those noted experimentally. It was found that large eddies play key role in creation of these structures. Upstream islands were observed in streamwise-transverse planes, however these were always found to be connected to the main flame. No evidence of unconnected flame elements was observed either as disconnected pockets of products upstream of the main flame or, in contrast to previous hydrogen lifted-flame DNS, as diffusion flame islands in lean regions. Two types of flame holes were found to occur. The first were extinction holes resulting from the interaction of large eddies with the flame which created a region of high scalar dissipation rate leading to local extinction. The second were inclusion holes. These types of holes were generated by propagation of edge flames around a large structure and reconnection upstream to create a hole. Example scenarios of either smooth or rapid upstream and downstream motion of the flame in a streamwise-transverse plane were examined and related to the flow and relative flame propagation velocities both within the plane and via out-of-plane motion.

2- Stabilisation mechanism

The statistics of flow and edge-flame propagation velocity components conditioned on the instantaneous locations of the flame revealed that the flow on average balances the relative propagation in the streamwise direction, thus demonstrating that the flame is stabilised essentially by edge-flame propagation. This is the first such demonstration, in a turbulent lifted flame, employing all components of local flame-propagation speeds.

Significant fluctuations in lifted height were observed. Conditioning of the net flame velocity on streamwise and transverse location revealed an elliptical pattern of flame motion around the average stabilisation point: first outwards towards the oxidiser, then upstream, then inwards towards the fuel, then downstream again. This motion would be clockwise on a vertical flame viewed horizontally. It is proposed that this motion is connected with the passage of large eddies. The observations support the stabilisation mechanism proposed by Su *et al.* [1], but suggest that in addition an out-of-plane motion around large eddies is required to explain how edge-flames can escape regions of high inwards transverse velocity. In addition, it was found that local edge-flame velocities can be significantly lower than the laminar flame speed in some regions, suggesting a moderating role is also played by scalar dissipation at small lifted heights.

The flame was then analysed in an averaged sense. It was observed that the entrainment flow locally bent around the flame location to result in locally upstream flow on the lean side of the averaged flame-stabilisation location. A budget of terms in the transport equation

for the Favre-averaged product mass fraction was then presented to provide support for the proposed stabilisation mechanism based on the instantaneous picture. The averaged structure was found to be fundamentally two-dimensional. On the lean side, upstream mean, turbulent, and laminar transport were balanced by entrainment into richer regions. On the rich side, the upstream turbulent transport and transport due to entrainment from the lean region balanced downstream convection. Downstream of this point the flame had a structure quite similar to a diffusion flame with subtle differences. On the lean side a quasi-laminar balance of reaction, laminar diffusion and entrainment was observed. In the core of the flame the downstream convection and laminar and turbulent transport of products out of the flame balanced reaction, entrainment from leaner regions, and – in contrast to what is expected in a diffusion flame – upstream turbulent transport of products. In very rich conditions downstream convection simply balanced transverse turbulent transport. Turbulent transport was found to be gradient-like on the highly turbulent rich side, and to have a small, but counter-gradient contribution on the weakly turbulent lean side.

The averaged picture was broadly consistent with the instantaneous and support the clockwise motion of individual flames leading to the above-described two-dimensional structure. However, the out-of-plane effect could not be observed due to the averaging in spanwise direction.

The results strongly support the edge-flame theory of lifted flame stabilisation where lifted height fluctuations linked to the passage of large eddies.

3- Edge flame statistics

Edge-flames were then studied in terms of their propagation speeds, the orientations of the normal vectors to mixture-fraction and product mass-fraction iso-surfaces, the curvatures of those iso-surfaces, strain rates in various directions, and gradients of product mass fraction and mixture fraction.

All of these quantities were found to undergo significant fluctuations as well as on-average variations depending on the spatial location. The net displacement velocities of edge-flames was found to be influenced by the both the displacement speeds of the mixture-fraction and product mass-fraction iso-surfaces, as well as the flame orientations. Product mass-fraction displacement speeds were less than S_L as a result of either large product mass-fraction iso-surface curvatures, caused by compressive strains across the narrow region edge-flames, or large extensive strain rates in the direction of the mutual tangent to product mass-fraction and mixture-fraction iso-surfaces. The mixture-fraction displacement speed variations were most strongly influenced by curvature, while the orientation of normal vectors was influenced by the direction and magnitude of strain.

On-average spatial fluctuations of the above quantities were found to occur. When connected with the observed clockwise elliptical motion of flame-edges, it was deduced that edge-flames undergo on-average cyclic fluctuations of the above quantities, notably they undergo cyclic fluctuations of the various displacement speeds involved in their net motion, and flame orientations, which were connected with cyclic fluctuations of strains and curvatures. A schematic was proposed detailing how these cyclic fluctuations were a result of the passage of large eddies.

7.2 Suggestions for further research

1- Parameter studies

While this thesis only reports results from one DNS case, as part of this research, an extensive database of DNS has been created to investigate whether and how the above-described picture depends on key parameters. The key parameters include: i) the lifted height, which can be readily increased by increasing the co-flow velocity, ii) dilution levels, iii) fuel Lewis number, and iv) configuration (round versus slot-jet). Application of the present analysis tools to these data-sets should be regarded as a high priority for future research.

2- The creation and destruction of inclusion and extinction holes

As mentioned earlier, discontinuities, i.e. holes, on the flame surfaces were observed. These were generated by two different mechanisms and were termed as extinction holes or inclusion holes depending on the mechanism. Both kinds of holes can grow, shrink and disappear as they go downstream. They can also merge with other holes and/or split into multiple holes. Future work is planned to quantify the relative importance of these two types of holes, as well as to understand their time evolutions and geometries. In particular it is planned to understand the conditions that lead to hole formation, and the conditions that lead to hole disappearance, i.e. flame healing.

3 - Out-of-plane motion in lifted flames

It was observed that out-of-plane flow and flame propagation are on average negligible while high levels of fluctuations were observed. Also it was realised that even though they are negligible on-average, they play roles in the elliptical motion of the flame base due to correlations with the flame orientation. Planned future work will quantify in an averaged sense the role of out-of-plane flow and flame propagation on the appearance of upstream islands, as well as to quantify other out-of-plane effects in an effort to better understand the existing, very substantial, body of experimental work based on in-plane measurements.

4 - Assessment of conditional moment closure in modelling turbulent lifted flames

The conditional moment closure (CMC) method aims to describe the reaction source terms in term of their conditional moments. In non-premixed flames, the mixture fraction is the conditioning parameter and it has been amply demonstrated that this conditional averaging can greatly reduce fluctuations, allowing chemical reaction source terms to be closed at relatively low order. There are few studies in the literature [142–145] discussing this concept in the lifted flame configuration and these discussions are limited to higher temperature co-flow conditions where the auto-ignition mechanism is dominant. Therefore, assessing the weaknesses and strengths of this approach needs to be examined in a low temperature co-flow condition, which can be achieved using the present database.

Planned future work will therefore quantify in an averaged sense the level of conditional fluctuations and will assess the first-order and second-order conditional moment closure approaches in the configuration of this lifted flame.

5 - Developing the flame surface density for lifted flames

The coherent flame model (CFM) proposed by Marble and Broadwell [146], and further developed by [100, 104], amongst others, is a geometrical modelling approach which has been typically used to model premixed combustion. It has also been used to model non-premixed combustion [147]. The mean reaction rate is estimated as the product of mean flame surface density, $\bar{\Sigma}$, and the consumption rate per unit surface, Ω_i in this approach. The consumption rate is usually provided from a counter-flow strained laminar flame simulation. In the case of a lifted flame, it is not as straightforward as one requires knowing whether or not the stoichiometric surface is burning. Conditioning the surface density on a reacting scalar can potentially achieve this. The conditional flame surface density evolution equation has been derived by Hawkes et al. [148], and is similar to the unconditional equation except it contains a source term which corresponds to the propagation of flame edges. An evolution equation for the line density of flame edges has also been developed. Future work is therefore planned to analyse these equations with a view to understanding the creation of burning surface area by flame propagation and the evolution of the line density of flame edges (i.e. edge creation and destruction). Potentially, this information could feed to a future conditional flame surface density model for lifted flames.

Finally, it is mentioned that future generations of supercomputers should be able to tackle lifted hydrocarbon flames using detailed chemistry. While we believe that the present model contains most of the essential features of a hydrocarbon lifted flame, it is clear that detailed chemistry effects could play a role in determining finer details of lifted flame stabilisation. Now that experimental and DNS parameter spaces are beginning to overlap, serious

thought should be given to future experimental targets that are friendly for DNS. The lifted flame is a very good option in this regard, since the inlet boundary conditions can be extremely well characterised, as difficulties with estimating the inlet scalar profiles are greatly reduced.

References

[1] L. K. Su, O. S. Sun, and M. G. Mungal, "Experimental investigation of stabilization mechanisms in turbulent, lifted jet diffusion flames," *Combust. Flame*, vol. 144, no. 3, pp. 494–512, 2006.

[2] *World Energy Outlook*. International Energy Agency, 2013.

[3] S. H. Chung, "Stabilization, propagation and instability of tribrachial triple flames," *Proc. Combust. Inst.*, vol. 31, no. 1, pp. 877 – 892, 2007.

[4] X. Qin, C. W. Choi, A. Mukhopadhyay, I. K. Puri, S. K. Aggarwal, and V. R. Katta, "Triple flame propagation and stabilization in a laminar axisymmetric jet," *Combust. Theor. Model.*, vol. 8, no. 2, pp. 293–314, 2004.

[5] R. K. A. Kailasanathan, T. L. B. Yelverton, T. Fang, and W. L. Roberts, "Effect of diluents on soot precursor formation and temperature in ethylene laminar diffusion flames," *Combust. Flame*, vol. 160, no. 3, pp. 656–670, 2013.

[6] C. R. Kaplan, E. S. Oran, and S. W. Baek, "Stabilization mechanism of lifted jet diffusion flames," *Symp. (Int.) Combust.*, vol. 25, no. 1, pp. 1183 – 1189, 1994.

[7] W. M. Pitts, "Importance of isothermal mixing processes to the understanding of lift-off and blowout of turbulent jet diffusion flames," *Combust. Flame*, vol. 76, no. 2, pp. 197–212, 1989.

[8] K. M. Lyons, K. A. Watson, C. D. Carter, and J. M. Donbar, "Upstream islands of flame in lifted-jet partially premixed combustion," *Combust. Sci. Technol.*, vol. 179, no. 5, pp. 1029–1037, 2007.

[9] A. Upatnieks, J. F. Driscoll, C. C. Rasmussen, and S. L. Ceccio, "Liftoff of turbulent jet flames—assessment of edge flame and other concepts using cinema-PIV," *Combust. Flame*, vol. 138, no. 3, pp. 259 – 272, 2004.

[10] M. Namazian, R. W. Schefer, and J. Kelly, "Scalar dissipation measurements in the developing region of a jet," *Combust. Flame*, vol. 74, no. 2, pp. 147–160, 1988.

[11] E. F. Hasselbrink Jr and M. G. Mungal, "Characteristics of the velocity field near the instantaneous base of lifted non-premixed turbulent jet flames," *Symp. (Int.) Combust.*, vol. 27, no. 1, pp. 867–873, 1998.

[12] R. W. Schefer, M. Namazian, and J. Kelly, "Stabilization of lifted turbulent-jet flames," *Combust. Flame*, vol. 99, no. 1, pp. 75–86, 1994.

[13] C. M. Müller, H. Breitbach, and N. Peters, "Partially premixed turbulent flame propagation in jet flames," *Symp. (Int.) Combust.*, vol. 25, no. 1, pp. 1099 – 1106, 1994.

[14] G. T. Kalghatgi, "Lift-off heights and visible lengths of vertical turbulent jet diffusion flames in still air," *Combust. Sci. Technol.*, vol. 41, no. 1-2, pp. 17–29, 1984.

[15] S. H. Stårner, R. W. Bilger, J. H. Frank, D. F. Marran, and M. B. Long, "Mixture fraction imaging in a lifted methane jet flame," *Combust. Flame*, vol. 107, no. 3, pp. 307 – 313, 1996.

[16] L. Muniz and M. G. Mungal, "Instantaneous flame-stabilization velocities in lifted-jet diffusion flames," *Combust. Flame*, vol. 111, no. 1, pp. 16–31, 1997.

[17] R. L. Gordon, I. Boxx, C. Carter, A. Dreizler, and W. Meier, "Lifted diffusion flame stabilisation: Conditional analysis of multi-parameter high-repetition rate diagnostics at the flame base," *Flow Turbul. Combust.*, vol. 88, no. 4, pp. 503–527, 2012.

[18] I. Boxx, C. Heeger, R. Gordon, B. Böhm, A. Dreizler, and W. Meier, "On the importance of temporal context in interpretation of flame discontinuities," *Combust. Flame*, vol. 156, no. 1, pp. 269–271, 2009.

[19] I. Boxx, C. Heeger, R. Gordon, B. Böhm, M. Aigner, A. Dreizler, and W. Meier, "Simultaneous three-component PIV/OH-PLIF measurements of a turbulent lifted, C_3H_8-Argon jet diffusion flame at 1.5 kHz repetition rate," *Proc. Combust. Inst.*, vol. 32, no. 1, pp. 905–912, 2009.

[20] Y. Mizobuchi, S. Tachibana, J. Shinio, S. Ogawa, and T. Takeno, "A numerical analysis of the structure of a turbulent hydrogen jet lifted flame," *Proc. Combust. Inst.*, vol. 29, no. 2, pp. 2009–2015, 2002.

[21] Y. Mizobuchi, J. Shinio, S. Ogawa, and T. Takeno, "A numerical study on the formation of diffusion flame islands in a turbulent hydrogen jet lifted flame," *Proc. Combust. Inst.*, vol. 30, no. 1, pp. 611–619, 2005.

[22] C. J. Lawn, "Lifted flames on fuel jets in co-flowing air," *Prog. Energy Combust. Sci.*, vol. 35, no. 1, pp. 1–30, 2009.

[23] L. Vanquickenborne and A. van Tiggelen, "The stabilization mechanism of lifted diffusion flames," *Combust. Flame*, vol. 10, no. 1, pp. 59 – 69, 1966.

[24] N. Peters and F. A. Williams, "Liftoff characteristics of turbulent jet diffusion flames," *AIAA Journal*, vol. 21, pp. 423–429, 1983.

[25] K. A. Watson, K. M. Lyons, J. M. Donbar, and C. D. Carter, "On scalar dissipation and partially premixed flame propagation," *Combust. Sci. Technol.*, vol. 175, no. 4, pp. 649–664, 2003.

[26] J. Buckmaster and R. Weber, "Edge-flame-holding," *Symp. (Int.) Combust.*, vol. 26, no. 1, pp. 1143 – 1149, 1996.

[27] H. Phillips, "Flame in a buoyant methane layer," *Symp. (Int.) Combust.*, vol. 10, no. 1, pp. 1277–1283, 1965.

[28] P. N. Kioni, B. Rogg, K. N. C. Bray, and A. Linán, "Flame spread in laminar mixing layers: the triple flame," *Combust. Flame*, vol. 95, no. 3, pp. 276–290, 1993.

[29] P. N. Kioni, K. N. C. Bray, D. A. Greenhalgh, and B. Rogg, "Experimental and numerical studies of a triple flame," *Combust. Flame*, vol. 116, no. 1–2, pp. 192–206, 1999.

[30] N. Kim, J. Seo, K. C. Oh, and H. D. Shin, "Lift-off characteristics of triple flame with concentration gradient," *Proc. Combust. Inst.*, vol. 30, no. 1, pp. 367–374, 2005.

[31] K. A. Watson, K. M. Lyons, J. M. Donbar, and C. D. Carter, "Simultaneous rayleigh imaging and CH-PLIF measurements in a lifted jet diffusion flame," *Combust. Flame*, vol. 123, no. 1–2, pp. 252 – 265, 2000.

[32] C. M. Arndt, R. Schießl, J. D. Gounder, W. Meier, and M. Aigner, "Flame stabilization and auto-ignition of pulsed methane jets in a hot coflow: Influence of temperature," *Proc. Combust. Inst.*, vol. 34, no. 1, pp. 1483 – 1490, 2013.

[33] J. Boulanger, L. Vervisch, J. Reveillon, and S. Ghosal, "Effects of heat release in laminar diffusion flames lifted on round jets," *Combust. Flame*, vol. 134, no. 4, pp. 355–368, 2003.

[34] J. E. Broadwell, W. J. Dahm, and M. G. Mungal, "Blowout of turbulent diffusion flames," *Symp. (Int.) Combust.*, vol. 20, no. 1, pp. 303–310, 1985.

[35] R. C. Miake-Lye and J. A. Hammer, "Lifted turbulent jet flames: A stability criterion based on the jet large-scale structure," *Proc. Combust. Inst.*, vol. 22, no. 1, pp. 817–824, 1989.

[36] C. P. Burgess and C. J. Lawn, "The premixture model of turbulent burning to describe lifted jet flames," *Combust. Flame*, vol. 119, no. 1, pp. 95–108, 1999.

[37] R. G. Abdel-Gayed, D. Bradley, and M. Lawes, "Turbulent burning velocities: a general correlation in terms of straining rates," *Proc. R. Soc. Lond.*, vol. 414, no. 1847, pp. 389–413, 1987.

[38] I. G. Boxx, W. Meier, and C. D. Carter, "Investigation of turbulent lifted planar jet flames using highspeed laser imaging diagnostics," *AIAA SciTech, 52nd Aerospace Sciences Meeting*, 2014.

[39] S. Meares, V. N. Prasad, M. Juddoo, K. H. Luo, and A. R. Masri, "Simultaneous planar and volume cross-lif imaging to identify out-of-plane motion," *Proc. Combust. Inst.*, vol. 35, no. 3, pp. 3813–3820, 2015.

[40] R. L. Gordon, A. R. Masri, and E. Mastorakos, "Simultaneous rayleigh temperature, OH− and CH_2O – LIF imaging of methane jets in a vitiated coflow," *Combust. Flame*, vol. 155, no. 1-2, pp. 181 – 195, 2008.

[41] R. L. Gordon, A. R. Masri, S. B. Pope, and G. M. Goldin, "A numerical study of auto-ignition in turbulent lifted flames issuing into a vitiated co-flow," *Combust. Theor. Model.*, vol. 11, no. 3, pp. 351–376, 2007.

[42] C. S. Yoo, R. Sankaran, and J. H. Chen, "Three-dimensional direct numerical simulation of a turbulent lifted hydrogen jet flame in heated coflow: flame stabilization and structure," *J. Fluid Mech.*, vol. 640, pp. 453–481, 12 2009.

[43] C. N. Markides and E. Mastorakos, "An experimental study of hydrogen autoignition in a turbulent co-flow of heated air," *Proc. Combust. Inst.*, vol. 30, no. 1, pp. 883–891, 2005.

[44] R. Cabra, T. Myhrvold, J. Y. Chen, R. W. Dibble, A. N. Karpetis, and R. S. Barlow, "Simultaneous laser raman-rayleigh-lif measurements and numerical modeling results of a lifted turbulent H_2/N_2 jet flame in a vitiated coflow," *Proc. Combust. Inst.*, vol. 29, no. 2, pp. 1881–1888, 2002.

[45] R. L. Gordon, A. R. Masri, and E. Mastorakos, "Simultaneous rayleigh temperature, OH-and CH_2O – LIF imaging of methane jets in a vitiated coflow," *Combust. Flame*, vol. 155, no. 1, pp. 181–195, 2008.

[46] K. H. Luo, "Combustion effects on turbulence in a partially premixed supersonic diffusion flame," *Combust. Flame*, vol. 119, no. 4, pp. 417 – 435, 1999.

[47] B. Coriton, A. M. Steinberg, and J. H. Frank, "High-speed tomographic piv and oh plif measurements in turbulent reactive flows," *Experiments in fluids*, vol. 55, no. 6, pp. 1–20, 2014.

[48] R. L. Gordon, A. R. Masri, S. B. Pope, and G. M. Goldin, "Transport budgets in turbulent lifted flames of methane autoigniting in a vitiated co-flow," *Combust. Flame*, vol. 151, no. 3, pp. 495 – 511, 2007.

[49] W. Wang and T. Echekki, "Investigation of lifted jet flames stabilization mechanism using RANS simulations," *Fire Saf. J.*, vol. 46, no. 5, pp. 254 – 261, 2011.

[50] B. F. Magnussen and B. H. Hjertager, "On mathematical modeling of turbulent combustion with special emphasis on soot formation and combustion," *Symp. (Int.) Combust.*, vol. 16, no. 1, pp. 719 – 729, 1977.

[51] J. W. Deardorff, "A numerical study of three-dimensional turbulent channel flow at large reynolds numbers," *J. Fluid Mech.*, vol. 41, no. 02, pp. 453–480, 1970.

[52] W. P. Jones and S. Navarro-Martinez, "Large eddy simulation of autoignition with a subgrid probability density function method," *Combust. Flame*, vol. 150, no. 3, pp. 170 – 187, 2007.

[53] S. Navarro-Martinez and A. Kronenburg, "Flame stabilization mechanisms in lifted flames," *Flow Turbul. Combust.*, vol. 87, pp. 377–406, 2011.

[54] T. Leung and I. Wierzba, "The effect of co-flow stream velocity on turbulent non-premixed jet flame stability," *Proc. Combust. Inst.*, vol. 32, no. 2, pp. 1671–1678, 2009.

[55] P. Domingo, L. Vervisch, and D. Veynante, "Large-eddy simulation of a lifted methane jet flame in a vitiated coflow," *Combust. Flame*, vol. 152, no. 3, pp. 415 – 432, 2008.

[56] C. S. Yoo, E. S. Richardson, R. Sankaran, and J. H. Chen, "A DNS study on the stabilization mechanism of a turbulent lifted ethylene jet flame in highly-heated coflow," *Proc. Combust. Inst.*, vol. 33, no. 1, pp. 1619–1627, 2011.

[57] C. Pantano, "Direct simulation of non-premixed flame extinction in a methane–air jet with reduced chemistry," *J. Fluid Mech.*, vol. 514, pp. 231–270, 2004.

[58] R. W. Grout, A. Gruber, C. S. Yoo, and J. H. Chen, "Direct numerical simulation of flame stabilization downstream of a transverse fuel jet in cross-flow," *Proc. Combust. Inst.*, vol. 33, no. 1, pp. 1629–1637, 2011.

[59] N. Chakraborty and E. Mastorakos, "Direct numerical simulations of localised forced ignition in turbulent mixing layers: The effects of mixture fraction and its gradient," *Flow Turbul. Combust.*, vol. 80, pp. 155–186, 2008.

[60] S. Cao and T. Echekki, "Autoignition in nonhomogeneous mixtures: Conditional statistics and implications for modeling," *Combust. Flame*, vol. 151, no. 1-2, pp. 120 – 141, 2007.

[61] K. Wohl, N. M. Kapp, and C. Gazley, "The stability of open flames," in *Symposium on Combust. Flame, and Explosion Phenomena*, vol. 3, pp. 3–21, Elsevier, 1948.

[62] D. Garrido-López and S. Sarkar, "Effects of imperfect premixing coupled with hydrodynamic instability on flame propagation," *Proc. Combust. Inst.*, vol. 30, no. 1, pp. 621 – 628, 2005.

[63] J. H. Chen, A. Choudhary, B. De Supinski, M. Devries, E. R. Hawkes, S. Klasky, W. K. Liao, K. L. Ma, J. Mellor-Crummey, N. Podhorszki, R. Sankaran, S. Shende, and C. S. Yoo, "Terascale direct numerical simulations of turbulent combustion using S3D," *Comput. Sci. Discov.*, vol. 2, no. 1, 2009.

[64] A. Krisman, E. R. Hawkes, M. Talei, A. Bhagatwala, and J. H. Chen, "Polybrachial structures in dimethyl ether edge-flames at negative temperature coefficient conditions," *Proc. Combust. Inst.*, 2014.

[65] O. Chatakonda, E. R. Hawkes, A. J. Aspden, A. R. Kerstein, H. Kolla, and J. H. Chen, "On the fractal characteristics of low damköhler number flames," *Combust. Flame*, vol. 160, no. 11, pp. 2422 – 2433, 2013.

[66] R. W. Grout, A. Gruber, H. Kolla, P. T. Bremer, J. C. Bennett, A. Gyulassy, and J. H. Chen, "A direct numerical simulation study of turbulence and flame structure in transverse jets analysed in jet-trajectory based coordinates," *J. Fluid Mech.*, vol. 706, pp. 351–383, 2012.

[67] H. Kolla, R. W. Grout, A. Gruber, and J. H. Chen, "Mechanisms of flame stabilization and blowout in a reacting turbulent hydrogen jet in cross-flow," *Combust. Flame*, vol. 159, no. 8, pp. 2755–2766, 2012.

[68] Z. Luo, C. S. Yoo, E. S. Richardson, J. H. Chen, C. K. Law, and T. Lu, "Chemical explosive mode analysis for a turbulent lifted ethylene jet flame in highly-heated coflow," *Combust. Flame*, vol. 159, no. 1, pp. 265–274, 2012.

[69] E. R. Hawkes, O. Chatakonda, H. Kolla, A. R. Kerstein, and J. H. Chen, "A petascale direct numerical simulation study of the modelling of flame wrinkling for large-eddy simulations in intense turbulence," *Combust. Flame*, vol. 159, no. 8, pp. 2690 – 2703, 2012.

[70] E. R. Hawkes, R. Sankaran, J. H. Chen, S. A. Kaiser, and J. H. Frank, "An analysis of lower-dimensional approximations to the scalar dissipation rate using direct numerical simulations of plane jet flames," *Proc. Combust. Inst.*, vol. 32, no. 1, pp. 1455–1463, 2009.

[71] T. Echekki and J. H. Chen, "Structure and propagation of Methanol–Air triple flames," *Combust. Flame*, vol. 114, no. 1–2, pp. 231 – 245, 1998.

[72] H. G. Im and J. H. Chen, "Structure and propagation of triple flames in partially premixed hydrogen–air mixtures," *Combust. Flame*, vol. 119, no. 4, pp. 436–454, 1999.

[73] C. A. Kennedy and M. H. Carpenter, "Several new numerical methods for compressible shear-layer simulations," *Appl. Numer. Math.*, vol. 14, no. 4, pp. 397 – 433, 1994.

[74] T. Passot and A. Pouquet, "Numerical simulation of compressible homogeneous flows in the turbulent regime," *J. Fluid Mech.*, vol. 181, pp. 441–466, 1987.

[75] A. Cessou, C. Maurey, and D. Stepowski, "Parametric and statistical investigation of the behavior of a lifted flame over a turbulent free-jet structure," *Combust. Flame*, vol. 137, no. 4, pp. 458–477, 2004.

[76] S. A. Stanley, S. Sarkar, and J. P. Mellado, "A study of the flow-field evolution and mixing in a planar turbulent jet using direct numerical simulation," *J. Fluid Mech.*, vol. 450, pp. 377–407, 2002.

[77] C. S. Yoo, Y. Wang, A. Trouvé, and H. G. Im, "Characteristic boundary conditions for direct simulations of turbulent counterflow flames," *Combust. Theor. Model.*, vol. 9, no. 4, pp. 617–646, 2005.

[78] C. S. Yoo and H. G. Im, "Characteristic boundary conditions for simulations of compressible reacting flows with multi-dimensional, viscous and reaction effects," *Combust. Theor. Model.*, vol. 11, no. 2, pp. 259–286, 2007.

[79] G. Lodato, P. Domingo, and L. Vervisch, "Three-dimensional boundary conditions for direct and large-eddy simulation of compressible viscous flows," *J. Comput. Phys.*, vol. 227, no. 10, pp. 5105 – 5143, 2008.

[80] S. B. Pope, *Turbulent Flows*. Cambridge University Press, 2000.

[81] N. Chakraborty and E. Mastorakos, "Numerical investigation of edge flame propagation characteristics in turbulent mixing layers," *Phys. Fluids*, vol. 18, no. 10, p. 105103, 2006.

[82] H. Hesse, N. Chakraborty, and E. Mastorakos, "The effects of the lewis number of the fuel on the displacement speed of edge flames in igniting turbulent mixing layers," *Proc. Combust. Inst.*, vol. 32, no. 1, pp. 1399–1407, 2009.

[83] H. Pitsch and S. Fedotov, "Stochastic modeling of scalar dissipation rate fluctuations in non-premixed turbulent combustion," *Center for Turbulence Research, Annual Research Briefs*, vol. 91, 2000.

[84] H. Yamashita, M. Shimada, and T. Takeno, "A numerical study on flame stability at the transition point of jet diffusion flames," *Symp. (Int.) Combust.*, vol. 26, no. 1, pp. 27 – 34, 1996.

[85] K. Bray, P. Domingo, and L. Vervisch, "Role of the progress variable in models for partially premixed turbulent combustion," *Combust. Flame*, vol. 141, no. 4, pp. 431 – 437, 2005.

[86] P. Domingo, L. Vervisch, and J. Réveillon, "DNS analysis of partially premixed combustion in spray and gaseous turbulent flame-bases stabilized in hot air," *Combust. Flame*, vol. 140, no. 3, pp. 172 – 195, 2005.

[87] E. Knudsen and H. Pitsch, "Capabilities and limitations of multi-regime flamelet combustion models," *Combust. Flame*, vol. 159, no. 1, pp. 242 – 264, 2012.

[88] S. Noda, H. Mori, Y. Hongo, and M. Nishioka, "Nonpremixed flamelet statistics at flame base of lifted turbulent jet nonpremixed flames," *JSME Int. J. B-Fluid T*, vol. 48, no. 1, pp. 75–82, 2005.

[89] J. Hult, U. Meier, W. Meier, A. Harvey, and C. F. Kaminski, "Experimental analysis of local flame extinction in a turbulent jet diffusion flame by high repetition 2-D laser techniques and multi-scalar measurements," *Proc. Combust. Inst.*, vol. 30, no. 1, pp. 701–709, 2005.

[90] M. Tanahashi, M. Fujimura, and T. Miyauchi, "Coherent fine-scale eddies in turbulent premixed flames," *Proc. Combust. Inst.*, vol. 28, no. 1, pp. 529 – 535, 2000.

[91] H. G. Im and J. H. Chen, "Effects of flow strain on triple flame propagation," *Combust. Flame*, vol. 126, no. 1, pp. 1384–1392, 2001.

[92] E. R. Hawkes and J. H. Chen, "Direct numerical simulation of hydrogen-enriched lean premixed methane–air flames," *Combust. Flame*, vol. 138, no. 3, pp. 242–258, 2004.

[93] E. R. Hawkes and J. H. Chen, "Comparison of direct numerical simulation of lean premixed methane–air flames with strained laminar flame calculations," *Combust. Flame*, vol. 144, no. 1, pp. 112–125, 2006.

[94] E. R. Hawkes, R. Sankaran, J. C. Sutherland, and J. H. Chen, "Scalar mixing in direct numerical simulations of temporally evolving plane jet flames with skeletal CO/H_2 kinetics," *Proc. Combust. Inst.*, vol. 31, no. 1, pp. 1633–1640, 2007.

[95] R. Sankaran, E. R. Hawkes, J. H. Chen, T. Lu, and C. K. Law, "Direct numerical simulations of turbulent lean premixed combustion," in *Journal of Physics: conference series*, vol. 46, p. 38, IOP Publishing, 2006.

[96] J. H. Chen, E. R. Hawkes, R. Sankaran, S. D. Mason, and H. G. Im, "Direct numerical simulation of ignition front propagation in a constant volume with temperature inhomogeneities: I. fundamental analysis and diagnostics," *Combust. Flame*, vol. 145, no. 1, pp. 128–144, 2006.

[97] N. Chakraborty and S. Cant, "Unsteady effects of strain rate and curvature on turbulent premixed flames in an inflow–outflow configuration," *Combust. Flame*, vol. 137, no. 1, pp. 129–147, 2004.

[98] E. R. Hawkes, R. Sankaran, and J. H. Chen, "A study of extinction and reignition dynamics in syngas jet flames using terascale direct numerical simulations: sensitivity to the choice of reacting scalar," in *Proceedings of the Australian Combustion Symposium*, pp. 46–49, 2007.

[99] E. R. Hawkes, R. Sankaran, and J. H. Chen, "Reignition dynamics in massively parallel direct numerical simulations of CO/H_2 jet flames," in *16th Australasian Fluid Mechanics Conference*, pp. 1271–1274, School of Engineering, The University of Queensland, 2007.

[100] S. B. Pope, "The evolution of surfaces in turbulence," *Int. J. Eng. Sci.*, vol. 26, no. 5, pp. 445–469, 1988.

[101] C. H. Gibson, W. T. Ashurst, and A. R. Kerstein, "Mixing of strongly diffusive passive scalars like temperature by turbulence," *J. Fluid Mech.*, vol. 194, pp. 261–293, 1988.

[102] N. Chakraborty, E. R. Hawkes, J. H. Chen, and R. S. Cant, "The effects of strain rate and curvature on surface density function transport in turbulent premixed methane–air and hydrogen–air flames: A comparative study," *Combust. Flame*, vol. 154, no. 1, pp. 259–280, 2008.

[103] J. H. Chen and H. G. Im, "Correlation of flame speed with stretch in turbulent premixed methane/air flames," in *Symp. (Int.) Combust.*, vol. 27, pp. 819–826, Elsevier, 1998.

[104] S. M. Candel and T. J. Poinsot, "Flame stretch and the balance equation for the flame area," *Combust. Sci. Technol.*, vol. 70, no. 1-3, pp. 1–15, 1990.

[105] D. Han and M. G. Mungal, "Observations on the transition from flame liftoff to flame blowout," *Proc. Combust. Inst.*, vol. 28, no. 1, pp. 537–543, 2000.

[106] F. Takahashi and W. J. Schmoll, "Lifting criteria of jet diffusion flames," *Symp. (Int.) Combust.*, vol. 23, no. 1, pp. 677–683, 1991.

[107] F. Takahashi, W. John Schmoll, and V. R. Katta, "Attachment mechanisms of diffusion flames," *Symp. (Int.) Combust.*, vol. 27, no. 1, pp. 675–684, 1998.

[108] J. B. Kelman, A. J. Eltobaji, and A. R. Masri, "Laser imaging in the stabilisation region of turbulent lifted flames," *Combust. Sci. Technol.*, vol. 135, no. 1-6, pp. 117–134, 1998.

[109] R. W. Schefer, M. Namazian, and J. Kelly, "Stabilization of lifted turbulent-jet flames," *Combust. Flame*, vol. 99, no. 1, pp. 75 – 86, 1994.

[110] R. W. Schefer, M. Namazian, E. E. J. Filtopoulos, and J. Kelly, "Temporal evolution of turbulence/chemistry interactions in lifted, turbulent-jet flames," *Symp. (Int.) Combust.*, vol. 25, no. 1, pp. 1223 – 1231, 1994.

[111] R. W. Schefer, "Flame sheet imaging using CH chemiluminescence," *Combust. Sci. Technol.*, vol. 126, no. 1-6, pp. 255–279, 1997.

[112] R. W. Schefer, "Three-dimensional structure of lifted, turbulent-jet flames," *Combust. Sci. Technol.*, vol. 125, no. 1-6, pp. 371–394, 1997.

[113] R. W. Schefer and P. J. Goix, "Mechanism of flame stabilization in turbulent, lifted-jet flames," *Combust. Flame*, vol. 112, no. 4, pp. 559 – 574, 1998.

[114] C. D. Brown, K. A. Watson, and K. M. Lyons, "Studies on lifted jet flames in coflow: the stabilization mechanism in the near-and far-fields," *Flow Turbul. Combust.*, vol. 62, no. 3, pp. 249–273, 1999.

[115] M. M. Tacke, D. Geyer, E. P. Hassel, and J. Janicka, "A detailed investigation of the stabilization point of lifted turbulent diffusion flames," *Symp. (Int.) Combust.*, vol. 27, pp. 1157–1165, 1998.

[116] C. Maurey, A. Cessou, B. Lecordier, and D. Stepowski, "Statistical flow dynamic properties conditioned on the oscillating stabilization location of turbulent lifted flame," *Proc. Combust. Inst.*, vol. 28, no. 1, pp. 545–551, 2000.

[117] F. Baillot and D. Demare, "Physical mechanisms of a lifted nonpremixed flame stabilized in an acoustic field," *Combust. Sci. Technol.*, vol. 174, no. 8, pp. 73–98, 2002.

[118] K. A. Watson, K. M. Lyons, J. M. Donbar, and C. D. Carter, "Simultaneous two-shot ch planar laser-induced fluorescence and particle image velocimetry measurements in lifted CH4/air diffusion flames," *Proc. Combust. Inst.*, vol. 29, no. 2, pp. 1905–1912, 2002.

[119] K. A. Watson, K. M. Lyons, J. M. Donbar, and C. D. Carter, "Scalar and velocity field measurements in a lifted CH_4 - air diffusion flame," *Combust. Flame*, vol. 117, no. 1-2, pp. 257 – 271, 1999.

[120] M. S. Mansour, "The flow field structure at the base of lifted turbulent partially premixed jet flames," *Experimental thermal and fluid science*, vol. 28, no. 7, pp. 771–779, 2004.

[121] A. Joedicke, N. Peters, and M. Mansour, "The stabilization mechanism and structure of turbulent hydrocarbon lifted flames," *Proc. Combust. Inst.*, vol. 30, no. 1, pp. 901–909, 2005.

[122] A. E. Dahoe and L. P. H. De Goey, "On the determination of the laminar burning velocity from closed vessel gas explosions," *J. Loss Prevent. Proc.*, vol. 16, no. 6, pp. 457–478, 2003.

[123] A. Upatnieks, J. F. Driscoll, and S. L. Ceccio, "Cinema particle imaging velocimetry time history of the propagation velocity of the base of a lifted turbulent jet flame," *Proc. Combust. Inst.*, vol. 29, no. 2, pp. 1897–1903, 2002.

[124] C. Heeger, B. Böhm, S. F. Ahmed, R. Gordon, I. Boxx, W. Meier, A. Dreizler, and E. Mastorakos, "Statistics of relative and absolute velocities of turbulent non-premixed edge flames following spark ignition," *Proc. Combust. Inst.*, vol. 32, no. 2, pp. 2957–2964, 2009.

[125] F. T. C. Yuen and O. L. Gülder, "Turbulent premixed flame front dynamics and implications for limits of flamelet hypothesis," *Proc. Combust. Inst.*, vol. 34, no. 1, pp. 1393 – 1400, 2013.

[126] G. R. Ruetsch, L. Vervisch, and A. Linán, "Effects of heat release on triple flames," *Phys. Fluids*, vol. 7, no. 6, pp. 1447–1454, 1995.

[127] L. D. Landau, "On the theory of slow combustion," *Acta Physicochim. URSS*, vol. 19, no. 1, pp. 77–85, 1944.

[128] D. Veynante, A. Trouvé, K. N. C. Bray, and T. Mantel, "Gradient and counter-gradient scalar transport in turbulent premixed flames," *J. Fluid Mech.*, vol. 332, pp. 263–293, 1997.

[129] C. Jiménez and B. Cuenot, "DNS study of stabilization of turbulent triple flames by hot gases," *Proc. Combust. Inst.*, vol. 31, no. 1, pp. 1649 – 1656, 2007.

[130] N. Peters, P. Terhoeven, J. H. Chen, and T. Echekki, "Statistics of flame displacement speeds from computations of 2-D unsteady methane-air flames," *Symp. (Int.) Combust.*, vol. 27, no. 1, pp. 833 – 839, 1998.

[131] J. Buckmaster, "Edge-flames," *Prog. Energy Combust. Sci.*, vol. 28, no. 5, pp. 435–475, 2002.

[132] J. Buckmaster, "Edge-flames and their stability," *Combust. Sci. Technol.*, vol. 115, no. 1-3, pp. 41–68, 1996.

[133] S. Ghosal and L. Vervisch, "Theoretical and numerical study of a symmetrical triple flame using the parabolic flame path approximation," *J. Fluid Mech.*, vol. 415, pp. 227–260, 2000.

[134] A. Juneja and S. B. Pope, "A dns study of turbulent mixing of two passive scalars," *Phys. Fluids*, vol. 8, no. 8, pp. 2161–2184, 1996.

[135] A. Trouvé and T. Poinsot, "The evolution equation for the flame surface density in turbulent premixed combustion," *J. Fluid Mech.*, vol. 278, pp. 1–31, 1994.

[136] I. R. Gran, T. Echekki, and J. H. Chen, "Negative flame speed in an unsteady 2-D premixed flame: A computational study," *Symp. (Int.) Combust.*, vol. 26, no. 1, pp. 323 – 329, 1996.

[137] T. Echekki and J. H. Chen, "Unsteady strain rate and curvature effects in turbulent premixed methane-air flames," *Combust. Flame*, vol. 106, no. 1, pp. 184–202, 1996.

[138] E. R. Hawkes and J. H. Chen, "Evaluation of models for flame stretch due to curvature in the thin reaction zones regime," *Proc. Combust. Inst.*, vol. 30, no. 1, pp. 647–655, 2005.

[139] N. Chakraborty and S. Cant, "A priori analysis of the curvature and propagation terms of the flame surface density transport equation for large eddy simulation," *Phys. Fluids*, vol. 19, no. 10, p. 105101, 2007.

[140] Y. S. Ko and S. H. Chung, "Propagation of unsteady tribrachial flames in laminar non-premixed jets," *Combust. Flame*, vol. 118, no. 1, pp. 151–163, 1999.

[141] W. T. Ashurst, A. R. Kerstein, R. M. Kerr, and C. H. Gibson, "Alignment of vorticity and scalar gradient with strain rate in simulated navier–stokes turbulence," *Phys. Fluids*, vol. 30, no. 8, pp. 2343–2353, 1987.

[142] E. S. Richardson, C. S. Yoo, and J. H. Chen, "Analysis of second-order conditional moment closure applied to an autoignitive lifted hydrogen jet flame," *Proc. Combust. Inst.*, vol. 32, no. 2, pp. 1695–1703, 2009.

[143] C. B. Devaud and K. N. C. Bray, "Assessment of the applicability of conditional moment closure to a lifted turbulent flame: first order model," *Combust. Flame*, vol. 132, no. 1, pp. 102–114, 2003.

[144] I. S. Kim and E. Mastorakos, "Simulations of turbulent lifted jet flames with two-dimensional conditional moment closure," *Proc. Combust. Inst.*, vol. 30, no. 1, pp. 911–918, 2005.

[145] M. Fairweather and R. M. Woolley, "First-order conditional moment closure modeling of turbulent, nonpremixed hydrogen flames," *Combust. Flame*, vol. 133, no. 4, pp. 393–405, 2003.

[146] F. E. Marble and J. E. Broadwell, "The coherent flame model for turbulent chemical reactions," tech. rep., DTIC Document, 1977.

[147] E. Van Kalmthout, D. Veynante, and S. Candel, "Direct numerical simulation analysis of flame surface density equation in non-premixed turbulent combustion," in *Symp. (Int.) Combust.*, vol. 26, pp. 35–42, Elsevier, 1996.

[148] E. R. Hawkes and R. S. Cant, "A flame surface density approach to large-eddy simulation of premixed turbulent combustion," *Proc. Combust. Inst.*, vol. 28, no. 1, pp. 51–58, 2000.

[149] W. M. Pitts, "Large-scale turbulent structures and the stabilization of lifted turbulent jet diffusion flames," *Symp. (Int.) Combust.*, vol. 23, no. 1, pp. 661–668, 1991.

[150] D. Demare and F. Baillot, "The role of secondary instabilities in the stabilization of a nonpremixed lifted jet flame," *Phys. Fluids*, vol. 13, no. 9, pp. 2662–2670, 2001.

[151] K. A. Watson, K. M. Lyons, J. M. Donbar, and C. D. Carter, "Observations on the leading edge in lifted flame stabilization," *Combust. Flame*, vol. 119, no. 1, pp. 199–202, 1999.

[152] M. S. Mansour, "Stability characteristics of lifted turbulent partially premixed jet flames," *Combust. Flame*, vol. 133, no. 3, pp. 263–274, 2003.

[153] K. N. Kim, S. H. Won, and S. H. Chung, "Characteristics of turbulent lifted flames in coflow jets with initial temperature variation," *Proc. Combust. Inst.*, vol. 31, no. 1, pp. 1591–1598, 2007.

[154] J. Oh and Y. Yoon, "Flame stabilization in a lifted non-premixed turbulent hydrogen jet with coaxial air," *Int. .J Hydrogen Energ.*, vol. 35, no. 19, pp. 10569–10579, 2010.

Appendix A

Experimental studies of lifted flames

The experimental studies of lifted flames in laboratory condition is listed in table A.1.

Table A.1 Experimental study of lifted flame in laboratory co-flow temperature

Reference	Fuel	d mm	Re	U_{jet} m/s	U_{co} m/s	T_{jet} K	T_{co} K	Remarks
Wohl *et al.* 1949 [61]	C_2H_4	*N.G.*	5000- 13000	*N.G.*	*N.G.*	300	300	- Different possibility of open-flame (flash back, attached, lifted and blow out).
Vanquickenborne & van Tiggelen 1966 [23]	CH_4	4	*N.G.*	*N.G.*	*N.G.*	300	300	- Turbulent premixed flame
Kalghatgi 1984 [14]	H_2, CH_4 C_2H_4, C_3H_8	$1-10$	N.G.	$10-400$	*N.G.*	300	300	- Turbulent flame speed correlated with turbulence Re number
Miake-Lye & Hammer 1989[35]	CH_4	3.8	4000 - 100,000	$10-60$	*N.G.*	300	300	- Stabilised by large eddy coherent structures
	C_2H_4	3.8	4000 - 100,000	$0-200$				
	NaturalGas		4000 - 100,000	$0-200$				
		3.8, 6.3, 7.9						
Pitts 1991 [149]	C_3H_8	6.35	3960	2.7	0.15	300	300	- Stabilised by large eddies
Muniz & Mungal 1997 [16]	CH_4	4.8	3900	14	0.58	300	300	- Leading edge exhibits triple flame
	CH_4		3800	14	0.43			like behaviour.
	CH_4		4000	14	0.27			- Propagation speed is less than $3S_L$.
	CH_4		10500	38	0.28			- Streamlines diverged at leading edge.
	C_2H_4		11400	22	1.2			
	C_2H_4		11100	21	1.72			
	C_2H_4		22000	42	1.85			
Hasselbrink & Mungal 1998 [11]	CH_4	4.8	8691	31	0.4	300	300	- Quasi-laminar partially
	C_2H_4		29700	61	2.0			premixed flame propagation

Continued on next page

Table A.1 – *Continued from previous page*

Reference	Fuel	d mm	Re	U_{jet} m/s	U_{co} m/s	T_{jet} K	T_{co} K	Remarks
Takahashi *et al.* 1998 [107] 1991[106]	CH_4	9.45	0 - 12500	$0-23$	$0-4.5$	300	300	Flame lifting and reattaching analysis
Kelman *et al.*1998 [108]	CNG	4.3	10000	$N.G.$	0.5	300	300	- Partially premixed flame propagation and cold quenching by large eddies
Schefer & Goix 1998 [113]	CH_4	5.4	7000	21	$N.G.$	300	300	- Stabilised by turbulent premixed propagation
Schefer & Namazian 1988 [10],1994 [110],1994 [109]			12000	37				
schefer 1997 [111, 112]			19500	60				
Brown *et al.* 1999 [114]	CH_4	2.54	N.G.	23.7	$0-2.7$	300	300	- Low lifted heights turbulence propagation
	C_2H_4		N.G.	15.7	$0-2.7$	300	300	ordinary lifted flames and blow out
	C_3H_8		N.G.	31.7	$0-2.7$	300	300	premixed flame theory
Han and Mungal 2000 [105]	CH_4	4.6	7000	25	0.36	300	300	- Co-flow velocity and blow out prediction
					0.72			
Maurey *et al.* 2000 [116]	CH_4	4	4100	16.3	$N.G.$	300	300	- Stabilised by edge propagation, instantaneous entrainment
Tacke *et al.* 1998 [115]	100% H_2	3	40000	1400	$N.G.$	300	300	- Stabilised by large eddy structures
	85% H_2 +15% N_2	4	23000	320				
	85% H_2 +15% N_2	4	34500	470				
	75% H_2 +25% N_2	4	17000	180				
Baillot and Demare 2002 [117] ,2001 [150]	CH_4	6	5000	13.5	$N.G.$	300	300	- Stabilised by Kelvin-Helmholtz structures with no acoustical excitation

Continued on next page

Table A.1 – *Continued from previous page*

Reference	Fuel	d mm	Re	U_{jet} m/s	U_{co} m/s	T_{jet} K	T_{co} K	Remarks
Watson *et al.* 2003 [25],2002 [118], 2000 [31], 1999 [119, 151]	CH_4	5	4800	15.8	0.13	300	300	- Stabilised by edge flame
			6400	21.2	0.13			- Scalar dissipation rate were measured.
			8300	27.5	0.19			
Mansour 2004[120],2003 [152]	CH_4, $\phi_j = 4.52$	4	2445.97	4.74	0.2	300	300	Premixed triple flame
	CH_4, $\phi_j = 5.69$		3633.62	7.45				
	CH_4, $\phi_j = 7.37$		5036.22	11.03				
Cessou *et al.* 2004 [75]	CH_4	2	2700 - 3800	$22-30$	0.05	300	300	- Blow-out prediction [34]
	C_3H_8	2	3800- 23000	$8-48$				
	C_2H_4	2	5000- 27,000	$21-115$				
	$90\%C_2H_4$	2	4700- 20,000	$21-88$				
	$80\%C_2H_4$	2	4500- 14,000	$21-68$				
	CH_4	3	3600- 6900	$19-37$				
	C_3H_8	3	5700- 42,000	$8-58$				
	C_2H_4	3	6400- 52,000	$18-146$				
	CH_4	4	3700- 11,000	$15-46$				
	C_3H_8	4	6700- 68,000	$7-71$				
	C_2H_4	4	8000- 54,000	$17-115$				
	CH_4	5	3700- 19,000	$12-62$				
	C_3H_8	5	8400- 61,000	$7-51$				
	C_2H_4	5	8300- 53,000	$14-91$				

Continued on next page

Table A.1 – *Continued from previous page*

Reference	Fuel	d mm	Re	U_{jet} m/s	U_{co} m/s	T_{jet} K	T_{co} K	Remarks
Upatnieks *et al.* 2004 [9], 2002 [123]	77% $CH_4 + 23\%$ N_2	5	4200	14	0.26	300	300	- No correlation of propagation with large eddies
			8500	33.2	0.47			- Laminar triple flame structure, streamline divergence
Joedicke 2005 *et al.* [121]	CH_4	4	3080, 4730	13, 20	0.1	300	300	- Stabilised by triple flame structure
			7100, 8280	30, 35				
	$85\%CH_4 + 15\%N_2$		3110, 4790	13, 20				
			7190, 8380	13, 20				
	C_3H_8		11400, 26300	13, 30				
	$85\%C_3H_8 + 15\%N_2$		8360, 12900	13, 20				
			19300, 22500	30, 35				
	$50\%C_2H_4 + 50\%N_2$		6500	20				
			13000	40				
Hult 2005 *et al.* [89]	33.2% H_2 22.1% CH_4 44.7% N_2	8	22,800	63.2	0.3	300	300	- Local extinction downstream by high strain rate vortices
Noda *et al.* 2005 [88]	38% CH_4+ 62% H_2	3.2	4200	50	1.0	300	300	- Scalar dissipation concept
			6700	80				$\chi_q = 17.21/s$ and χ is log-normal
Su *et al.* 2006 [1]	Methane (CH_4)	4.6	4400	10.8	0.36	300	300	- Large eddy theory
			6200	15.3				flow velocity was 1 to 3 S_L
Kim *et al.* 2007 [153]	(0.6 to 1.0%) C_3H_8 + (0.4- 0.0 %) N_2	1.65	N.G.	lifted to blow out	0.5	294 to 900	294 to 900	- The jet and co-flow temperatures increases Lifted height

Continued on next page

Table A.1 – *Continued from previous page*

Reference	Fuel	d mm	Re	U_{jet} m/s	U_{co} m/s	T_{jet} K	T_{co} K	Remarks
Lyons *et al.* 2007 [8]	CH_4	*N.G.*	4800- 6400	$15.8-27.5$	0.13 – 0.19	300	300	- Out-of-plane motion
Oh and Yoon 2010 [154]	Hydrogen	3.65	3,318 6,636 9954	100 200 300	16 $12, 16, 20$ 16	300	300	- Stabilised by local principle strain and turbulent intensity - Turbulent propagation theory
Boxx *et al.* 2009 [18, 19]	75% C_3H_8 + 25% Argon	4	10,000	17	*N.G.*	300	300	- Upstream islands and out-of-plane motion - Downstream holes and local extinction
Gordon 2012 *et al.* [17]	75% propane (C_3H_8) + 25% Argon	4	10,000 - 15,000	*N.G.*	0.2	300	300	- Stabilised by upstream islands and out-of-plane fluid motion
Boxx 2014 *et al.* [38]	75% propane (C_3H_8) + 25% Argon	4×40	5,000	*N.G.*	0.15 0.3 0.43	300	300	- Laminar edge flame - Streamline divergence velocity fluctuations